Title
Mechanisms to establish higher-order chromosome structure and regulate gene expression

Author
Anderson, Erika

Publication Date
2018

Peer reviewed|Thesis/dissertation

Mechanisms to establish higher-order chromosome structure and regulate gene expression

By

Erika Cannon Anderson

A dissertation submitted in partial satisfaction of the

requirements for the degree of

Doctor of Philosophy

in

Molecular and Cell Biology

in the

Graduate Division

of the

University of California, Berkeley

Committee in charge:

Professor Barbara J. Meyer, Chair
Professor Jasper Rine
Professor Gary H. Karpen
Professor Robert L. Fischer

Fall 2018

Mechanisms to establish higher-order chromosome structure and regulate gene expression

By

Erika Cannon Anderson

Abstract

Mechanisms to establish higher-order chromosome structure and regulate gene expression

by

Erika Cannon Anderson

Doctor of Philosophy in Molecular and Cell Biology

University of California, Berkeley

Professor Barbara J. Meyer, Chair

In species that use chromosome-based sex determination, the copy number of sex chromosomes differs between the two sexes. Multiple different molecular mechanisms have evolved independently in diverse animal taxa to compensate for this imbalance in sex chromosome dose. In *Drosophila* species, gene expression from the single X in males is upregulated twofold. In *Caenorhabditis* species, genes from the two hermaphrodite Xs are downregulated by half. In mammals, one of the two X chromosomes is inactivated in females. In Chapter 1, I use these three dosage compensation strategies to illustrate the variety of ways in which gene expression can be coordinately regulated across an entire chromosome. The proteins and non-coding RNAs that enact dosage compensation also change histone marks over broad domains, compact chromosomes, restructure higher-order domain organization, and reposition X chromosomes within the nucleus, providing valuable models to dissect how chromosomes are organized at multiple scales.

In Chapter 2, I use the process of *Caenorhabditis elegans* X-chromosome dosage compensation to investigate how chromosome architecture is established and its relationship to gene expression. In *C. elegans*, a dosage compensation complex (DCC) equalizes X expression between sexes by repressing transcription from the two hermaphrodite Xs by half while also establishing a unique structure composed of megabase-scale topologically associating domains (TADs). DCC-dependent TAD boundaries all contain a strong DCC binding site (*rex* site). By making a series of *rex* site deletions and insertions and measuring the resulting chromosome structure, I determined that DCC binding at a strong *rex* site is necessary and sufficient for boundary formation. Deleting all eight of the *rex* sites at DCC-dependent boundaries recapitulated the TAD structure of a DCC mutant. When TAD structure was disrupted but most DCC binding was retained, X chromosome expression was not changed, indicating that TADs are neither a cause nor consequence of X repression. However, the worms showed increased thermosensitivity, accelerated aging, and shortened lifespan, suggesting a role for chromosome structure in regulating stress and aging programs.

Acknowledgements

First, I would like to thank my amazing advisor Barbara for her mentorship, wealth of ideas for experiments, and insightful comments on many drafts. Several years before I was born, Barbara discovered that "*C. elegans* possesses a dosage compensation mechanism that equalizes the X-specific transcript levels in X0 males and XX hermaphrodites," and she's steadily been figuring out that mechanism ever since. It's an honor for me to learn from such a dedicated and thorough scientist and to be part of the newest chapter of the dosage compensation story.

I'm hugely indebted to all the current and former Meyer Lab members who have taught me techniques and shared their excellent feedback and wide-ranging expertise. In particular, Qian, my baymate of five years, patiently and wisely answered several thousand questions on topics ranging from "Where are the tubes?" to "How do you think TADs work?". Satoru kept the microscopes and computers running and battled with software installation on my behalf. Denise heroically kept everything else in the lab running. Qiming thoughtfully performed important experiments, leaving protocols better than he found them. Anel and Aurora kept the lab stocked with media, plates, and clean dishes. Deborah transformed my plots into truly beautiful figures.

Beyond the lab, I'm incredibly grateful to my wonderful collaborators Phil, Ryo, and Katie for enthusiastically counting many dead worms and teaching me all about stress and aging in *C. elegans*. My committee members Jasper, Gary, and Bob provided useful guidance and creative ideas over the years, and helpful comments on this thesis. Thanks to the staff in the Functional Genomics Laboratory and Genomics Sequencing Laboratory who made all my sequencing run smoothly. And thanks to the custodian for his friendly smile on the days when I was in lab at midnight.

My data analysis was made possible by the knowledgeable and generous people who anonymously answer questions on forums like Stack Overflow. I'm grateful to members of the Dekker and Mirny labs for making their Hi-C analysis software available and fielding questions. These experiments were also made possible by fascinating podcasts that kept me focused while harvesting tens of millions of worm embryos.

I'm appreciative of the years of public education that prepared me for graduate school. I first learned how exciting science is and how to work hard at it from my teammates and coaches on the Bloomington High School North Science Olympiad team, which was made possible by Mr. Portle welcoming us into his classroom every afternoon. I'm grateful for my incomparable mentors at Indiana University, Mimi, Claire, and Soni, who gave me a foundation in how to do experiments and read and write about biology.

My friends, classmates, roommates, running buddies, and fellow carillon students who make it a joy to live in Berkeley are too numerous to name. Thanks to them for providing encouragement, commiseration, stress relief, and writing playlists. Finally, I'm grateful to my family for always believing in me, being my biggest cheerleaders, and staying interested in all my explanations of chromosome biology.

Table of Contents

Chapter 1
Introduction to mechanisms for chromosome-wide dosage compensation

Introduction

In species that use chromosome-based sex determination, the copy number of sex chromosomes differs between males and females. For example, in humans, female cells contain two X chromosome and two sets of autosomes, while male cells have only one X along with two sets of autosomes. Typically, altering the copy number of a single chromosome is lethal (Torres et al., 2008). Therefore, species must compensate for the difference in sex chromosome dose between sexes.

Multiple different molecular mechanisms to compensate for this imbalance in sex chromosome dose have evolved independently in diverse animal taxa. In *Drosophila* species, gene expression from the single X in males is upregulated twofold. In *Caenorhabditis* species genes from the two hermaphrodite Xs are each downregulated twofold. In mammals, one of the two female X chromosomes is inactivated. The diverse mechanisms employed illustrate the variety of ways in which gene expression can be coordinately regulated across an entire chromosome. The proteins and non-coding RNAs that enact dosage compensation also modify histones over broad domains, compact chromosomes, restructure higher-order domain organization, and reposition X chromosomes within the nucleus. Dosage compensation systems therefore provide valuable models to dissect how chromosomes are organized at multiple scales. I use the three best-understood dosage compensation systems (nematodes, flies, and placental mammals) to explore the relationships between X chromosome histone modifications, architecture, nuclear positioning, and transcription.

Diversity of dosage compensation machinery

Dosage compensation machinery is capable of distinguishing the X chromosome from autosomes and altering X transcription. In each species, dosage compensation factors include some proteins or RNAs unique to dosage compensation and other proteins that also function in other, non-X-specific complexes.

In *C. elegans* hermaphrodites (XX), expression from each X is downregulated twofold to equal the expression level in males (X0). This transcriptional repression is enacted by a dosage compensation complex (DCC), which binds to the hermaphrodite Xs and reduces recruitment of RNA Polymerase II (Pol II) (Kruesi et al., 2013). The DCC includes five condensin subunits and five additional subunits. Among the condensin subunits, the SMC protein MIX-1 (Lieb et al., 1998), the kleisin DPY-26 (Lieb et al., 1996), and two HEAT domain-containing proteins (DPY-28 and CAPG-1) (Csankovszki et al., 2009; Tsai et al., 2008) are also components of Condensin I, while the SMC protein DPY-27 is unique to the DCC (Chuang et al., 1994; Csankovszki et al., 2009; Mets and Meyer, 2009). Condensins belong to the structural maintenance of chromosomes (SMC) family of protein complexes and condense chromosomes in multiple contexts, including cell division (Hirano, 2016). Loss of MIX-1, DPY-26, DPY-28, or CAPG-1 causes defects in mitotic chromosome segregation and meiotic recombination and chromosome segregation (Csankovszki et al., 2009; Mets and Meyer, 2009). Among the non-condesin DCC subunits, SDC-2 is a protein with hermaphrodite-specific expression required for loading of all

other DCC components onto the X chromosome (Dawes et al., 1999). Loading of all subunits other than SDC-2 requires SDC-3 (Davis and Meyer, 1997) and DPY-30 (a component of the MLL/COMPASS complex) (Hsu et al., 1995; Pferdehirt et al., 2011). The final DCC subunits, SDC-1 and DPY-21, are required for full DCC activity but are not needed for loading of other subunits (Nonet and Meyer, 1991; Yonker and Meyer, 2003). DPY-21 is an H4K20me2 demethylase, and its activity results in enrichment of H4K20me1 on X compared to autosomes (Brejc et al., 2017).

The DCC recognizes the X chromosome by binding to recruitment elements on X (*rex* sites), which recruit the complex autonomously, even when inserted onto autosomes (Wheeler et al., 2016). Most strong *rex* sites contain clusters of DNA motifs that are enriched on the X chromosome (Albritton et al., 2017; Ercan et al., 2007; Jans et al., 2009; McDonel et al., 2006). The DCC also binds with lower occupancy to secondary sites, called dependent on X (*dox* sites). These sites only bind the DCC when on the X chromosome, not when present in extrachromosomal arrays. In an X-to-autosome fusion chromosome, the DCC binds the first several megabases of the autosome adjoining the X (Pferdehirt et al., 2011), suggesting a model in which the complex first binds to *rex* sites and then spreads along the chromosome to other sites.

In placental mammals, dosage compensation occurs in female (XX) cells, but instead of reducing expression from both Xs, one X chromosome is silenced while genes from the other X are expressed. X chromosome inactivation is initiated by expression of the long non-coding RNA (lncRNA) Xist, which is transcribed from X and spreads across the chromosome in cis. Transcription is silenced due to exclusion of Pol II from the Xist territory (Chaumeil et al., 2006). Human Xist is 17 kb and contains several conserved repeats (Brown et al., 1992). Separate domains mediate Xist spreading across the X chromosome and transcriptional silencing. Conserved repeats on the 5' end of Xist, known as the A repeats, are necessary for transcriptional silencing, while spreading is controlled by the cooperative effect of multiple sequences dispersed throughout the lncRNA (Wutz et al., 2002). Crosslinking studies have identified ten proteins that interact directly with *Xist*, including three that are essential for X silencing (McHugh et al., 2015). SHARP is a transcriptional repressor that indirectly interacts with the histone deacetylase HDAC3; lamin B receptor (LBR) is a protein embedded in the inner nuclear membrane that binds both lamins and chromatin (Gruenbaum et al., 2005); and SAF-A binds chromatin-associated RNAs and regulates chromosome compaction (Nozawa et al., 2017). The polycomb complexes PRC1 and PRC2 catalyze the enrichment of histone modifications H2AK119ub and H3K27me3 on the inactive X, which may be important for maintenance of silencing (Brockdorff, 2017).

The X chromosome is distinguished from autosomes by expression of Xist. Driving Xist transcription from an autosome is sufficient to repress the autosomal genes, though the silencing is less efficient than Xist-mediated silencing on X (Jiang et al., 2013; Loda et al., 2017). Unlike the *C. elegans* DCC, which binds to discrete recruitment sites, Xist broadly localizes across the entire X chromosome (though binding is lowest at genes that escape inactivation). After its initial transcription, Xist first spreads to loci that interact with the *Xist* locus in 3D and then spreads to active genes (Chen et al., 2016; Engreitz et al., 2013).

In *Drosophila melanogaster*, dosage compensation is achieved by upregulating X-linked genes in males (XY) twofold to match the expression level in females (XX). This activation is carried out by a ribonucleoprotein complex that mediates acetylation of H4K16 to increase the

efficiency of transcriptional elongation. The complex, known as the male-specific lethal (MSL) complex, binds to two categories of sites, similarly to the *C. elegans* DCC. The MSL complex is recruited to ~150 High Affinity Sites (HAS), which contain sequence motifs called MSL recognition elements (Alekseyenko et al., 2008). A HAS is sufficient to recruit the complex to an autosome (Alekseyenko et al., 2008). The complex disperses from HAS to additional binding sites across the X chromosome.

The MSL complex is composed of two lncRNAs and five protein subunits. The lncRNAs, roX1 and roX2, are encoded on the X chromosome, and their loci function as HAS. When roX1 and roX2 are eliminated, the MSL complex binds only at HAS without dispersing across the entire X, revealing the importance of the lncRNAs for spreading of the complex (Figueiredo et al., 2014). The only MSL subunit expressed exclusively in males is the E3 ubiquitin ligase MSL2. MSL2 contributes to X chromosome binding of the complex by binding MSL recognition elements (Zheng et al., 2014). Spreading of the complex requires the chromodomain-containing protein MSL-3 (Sural et al., 2008). The histone acetyl transferase MOF is responsible for H4K16 acetylation (Akhtar and Becker, 2000; Gelbart et al., 2009; Hilfiker et al., 1997). Outside of the MSL complex, MOF is also a component of the non-specific lethal complex, which is important for recruitment of Pol II to housekeeping genes throughout the genome (Lam et al., 2012; Raja et al., 2010). In addition to H4K16, MOF can acetylate other H4 lysine residues (Cai et al., 2010) and non-histone proteins, including MSL3 (Buscaino et al., 2003). MSL1 serves as a scaffold for the complex, interacting with MSL2, MSL3, and MOF (Scott et al., 2000), and MLE is a DNA/RNA helicase needed for incorporating roX1 and roX2 into the complex (Meller et al., 2000).

The independent strategies used for dosage compensation in worms, placental mammals, and flies use entirely separate sets of proteins and lncRNAs to recognize and transcriptionally regulate X chromosomes. In each case, factors required for distinguishing X from autosomes are unique to dosage compensation (SDC-2, Xist, MSL2). Additional proteins necessary for dosage compensation have been appropriated from complexes involved in histone modification (DPY-30, SHARP, and MOF) or chromosome organization (condensin I components, SAF-A).

Remodeling chromosome structure in dosage compensation

The *C. elegans* DCC condenses hermaphrodite X chromosomes (Brejc et al., 2017; Lau et al., 2014), just as condensin complexes compact chromosomes in other contexts. Measuring the X chromosome territory using fluorescence in situ hybridization (FISH) probes that tiled across the chromosome revealed that X chromosomes occupied 10 percent of nuclear volume in wild-type worms. Upon depletion of DCC components DPY-27, DPY-30, or DPY-21, X chromosome volume expanded to 16 percent of the nuclear volume, while the volume of an autosomal territory was unaffected (Lau et al., 2014).

In addition to overall compaction of the X chromosome, the DCC establishes a unique X chromosome topology, distinct from the structure of autosomes (Crane et al., 2015). Animal chromosomes are organized into megabase-scale topologically associating domains (TADs) within which loci tend to interact with each other while being insulated from interactions with loci in neighboring TADs. By comparing genome-wide chromatin interaction frequencies (measured by Hi-C) in wild-type and *sdc-2* mutant embryos, Crane et al found that the DCC mediates formation of TAD boundaries at eight strong *rex* sites (Crane et al., 2015). Although

autosomes are also organized into TADs, X chromosome TAD boundaries are stronger and more regularly spaced. The DCC also promotes strong, specific interactions between pairs of *rex* sites. Interactions between *rex* sites at adjacent DCC-dependent TAD boundaries are among the strongest interactions on the chromosome, and *rex* sites within TADs also interact (Crane et al., 2015).

In Chapter 2, I use a series of *rex* site deletions and insertions to identify the requirements for creating a DCC-dependent boundary. Single *rex* deletions eliminated the associated TAD boundaries, revealing that DCC binding at strong rex sites is necessary for boundary formation. Insertion of a *rex* site at a new location on X defined a new boundary, indicating that DCC binding at a boundary, and not intra-TAD interactions, is sufficient to define the boundary. In wild type, the DCC promotes strong interactions between *rex* sites at DCC-dependent boundaries. However, an inserted *rex* site can create a boundary without interacting with other DCC-dependent TAD boundaries. Therefore, boundary-to-boundary interactions are not required for boundary formation. Establishment of full-strength DCC-dependent boundaries also requires proper H4K20me1 (Brejc et al., 2017). Disrupting TAD structure while leaving most DCC binding intact did not cause visible dosage compensation phenotypes or significant changes in gene expression in embryos. Therefore DCC-mediated TAD structure is neither a cause nor consequence of transcriptional repression (Chapter 2).

Independent of creating TAD boundaries, the DCC also promotes interactions chromosome-wide at the scale of hundreds of kilobases (Chapter 2). The DCC's dual functions in establishing boundaries and compacting chromatin at the 100-kb scale are consistent with the popular loop extrusion model for TAD boundary formation and chromosome compaction by SMC complexes. In keeping with this model (Fudenberg et al., 2016), I propose that the condensin portion of the DCC is loaded onto X and extrudes a chromatin loop of increasing size until it reaches a *rex* site where strong binding of SDC proteins halts extrusion. When the DCC loads across X, it creates loops at many loci, which are reflected in increased DNA interactions between loci at the scale of hundreds of kb. Because the loops do not cross strong *rex* sites, the *rex* sites delineate boundaries between TADs. Disrupting DCC-dependent TADs does not change the volume of the X chromosome territory, indicating that chromosome compaction is independent of TAD boundary formation and may instead result from the DCC's promotion of interactions at the 100-kb scale.

Mammalian X inactivation is also accompanied by chromosome compaction. For decades, the inactive X has been observed as a densely staining region of heterochromatin known as the Barr body (Barr and Bertram, 1977). Later measurements showed that this Barr body does not include the full chromosome, but is a compact core made up of repetitive sequences. Coding sequences of the X are located in the outer rim of the chromosomal territory (Clemson et al., 2006). Visualizing the full inactive X chromosome using FISH paint revealed that the inactive X chromosome territory is compacted only 1.2-fold compared to the active X in human cells, but the shape of the inactive X territory is smoother and rounder compared to the active X and autosomes (Eils, 1996).

Hi-C measurements show that the inactive X has a unique structure compared to autosomes and the active X (Giorgetti et al., 2016; Rao et al., 2014). Mammalian genomes are partitioned into transcriptionally active and transcriptionally repressed compartments that interact in cis and trans (A and B compartments, respectively) (Lieberman-Aiden et al., 2009),

but the inactive X lacks these compartments. The inactive X also generally lacks the TADs observed on the active X (Giorgetti et al., 2016). Instead, the inactive X chromosome is organized into two megadomains of 73 and 93 Mb separated by a boundary located at the *DXZ4* macrosatellite. *Dxz4* deletions eliminate the boundary between superdomains but have no major effect on X chromosome H3K27 methylation, transcription, or nuclear localization (Darrow et al., 2016; Froberg et al., 2018).

The presence of TADs on X is generally correlated with active gene expression, but the causal relationship between the TAD structure and transcription remains unclear. TADs are observed on the active X and on the inactive X only around genes that escape X inactivation. TAD and compartment structure is antagonized by the noncanonical SMC protein SMCHD1, which is enriched on the inactive X (Gdula et al., 2018; Wang et al., 2018). When SMCHD1 was depleted, binding of proteins necessary for TAD formation (cohesin and CTCF) increased, TADs were strengthened, and new compartments emerged at different locations from A and B compartments (Gdula et al., 2018; Wang et al., 2018). In mouse embryos, loss of SmcHD1 results in activation of at least half of the genes on the inactive X. In contrast, SmcHD1 deletion in differentiated mouse embryonic fibroblasts, does not cause reactivation of genes on the inactive X (Gdula et al., 2018). Therefore, TAD structure can be established in the absence of X expression, revealing that the TADs are not a consequence of transcription. These results also suggest that SmcHD1 may be needed at an early stage of silencing but not for silencing maintenance.

The condensin of the *C. elegans* DCC and mammalian SMCHD1 homodimers are both SMC complexes that promote interactions across X chromosomes, but their effects on domain organization are vastly different. DCC binding establishes TAD boundaries while SMCHD1 erases TADs. These opposite changes in TAD architecture both occur concurrently with compaction, highlighting that establishment of TAD structure and chromosome compaction by SMC complexes are separable processes.

Dosage compensation does not change the volume or TAD organization of *D. melanogaster* X chromosomes. HAS are enriched at TAD boundaries and there are strong interactions between HAS. However, unlike DCC-dependent TAD boundaries in *C. elegans*, TAD boundaries on the *D. melanogaster* X are maintained in males and females and in the absence of MSL2 or MSL3 (Ramírez et al., 2015). Though dosage compensation does not modulate TAD structure, other chromosome topology may be important for the transcriptional activation. The DNA supercoiling factor SCF generates negative supercoils in conjunction with topoisomerase II and colocalizes with the MSL complex on chromatin. Knockdown of SCF results in male-specific lethality and reduced X transcription in males (Furuhashi et al., 2006), suggesting that regulation of supercoiling may play a role in transcriptional activation.

X chromosome nuclear positioning

In *C. elegans*, changing the position of the X chromosome within the nucleus has a minor effect on dosage compensation (Snyder et al., 2016). Each *C. elegans* chromosome is comprised of a central region, which is enriched for active chromatin marks, and two distal arm regions, which are anchored at the nuclear lamina and enriched for repressive chromatin marks including H3K9 mono-, di-, and tri-methylation (Towbin et al., 2012). Eliminating H3K9me or disrupting the anchoring of chromosome arms to the nuclear lamina results in X chromosome

decompaction and relocalization to a more interior nuclear position, while autosome volume and positioning are unaffected. These mutations also cause subtle but statistically significant increases in X expression. Average expression of genes on X increased 1.07-fold in the absence of H3K9me and 1.04-fold in the absence of chromosome anchoring, while autosome expression was slightly reduced. The dosage compensation defects were detectable by a sensitive genetic assay (Snyder et al., 2016).

Mammalian inactive X chromosomes tend be located in proximity to either the nuclear periphery (Belmont et al., 1986) or the nucleolus (Bourgeois et al., 1985). The inactive X is recruited to the periphery by a direct interaction between Xist and LBR, a transmembrane protein anchored in the inner nuclear membrane (Chen et al., 2016). Disruption of Xist recruitment to the nuclear lamina results in a loss of X inactivation, but tethering the X to the lamina does not induce silencing. Therefore, positioning at the lamina is necessary but not sufficient for transcriptional silencing (Chen et al., 2016).

It remains unclear why peripheral localization contributes to transcriptional repression of *C. elegans* and mammalian X chromosomes. Sequences associated with the lamina tend to be enriched for heterochromatin marks and transcriptionally silenced (Ikegami et al., 2010), suggesting that localization to a transcriptionally repressive environment could contribute to Pol II exclusion from the X. However, this model does not explain the observation that even genes in the central region of the *C. elegans* X chromosome that are not lamin-associated show increased expression upon loss of anchoring. Disruption of Xist peripheral recruitment resulted in reduced localization of Xist to X chromosome regions with actively transcribed genes, suggesting that anchoring to the nuclear periphery may constrain X chromosome mobility in a way that facilitates Xist spreading, rather than causing repression directly (Chen et al., 2016).

Changing gene expression

Binding of the *C. elegans* DCC to hermaphrodite X chromosomes mediates H4K20me1 enrichment, chromosome compaction, *rex-rex* interactions, and TAD boundary formation. Which of these changes lead to transcriptional repression? Measurements of nascent transcription by GRO-seq showed an increase in engaged Pol II across the length of genes on X in a DCC mutant. Therefore, the DCC reduces Pol II recruitment or transcription initiation rather than regulating transcription elongation (Kruesi et al., 2013). Multiple lines of evidence show that the mechanism regulating Pol II recruitment must function chromosome-wide, rather than acting gene-by-gene. First, for genes on X, nearby DCC binding does not predict the degree of transcriptional repression (Jans et al., 2009). Second, twelve transgenes inserted at locations across X were all dosage compensated, independent of their proximity to a *rex* site (Wheeler et al., 2016). Finally, DCC binding on autosomes is not sufficient to repress nearby genes.

One specific DCC function known to control gene expression is demethylation of H4K20me2 catalyzed by the DCC component DPY-21 (Brejc et al., 2017). Worms with a catalytically dead *dpy-21* mutation are viable and fertile but show dosage compensation defects (detectable by genetic assays) and elevated expression of genes on X. The magnitude of repression loss is larger than that when peripheral anchoring is disrupted but less severe than the derepression in an *sdc-2* mutant (in which the DCC fails to load). Additional DCC activities beyond H4K20me2 demethylation are therefore crucial for transcriptional repression.

Because dosage compensation is a chromosome-wide process, the DCC-mediated chromosome-wide changes in higher order architecture may be important for reducing polymerase recruitment. The TAD structure established by the DCC is dispensable for dosage compensation, but TAD-independent DCC-mediated chromosome interactions between loci within hundreds of kb may be involved in repression. These interactions could be indicative of the DCC creating an X chromosome compartment with an environment unfavorable to polymerase recruitment.

Just as the *C. elegans* DCC remodels X chromosomes at multiple scales, binding of Xist to mammalian X chromosomes has diverse effects including enrichment of repressive chromatin marks, chromatin compaction, loss of TADs and compartments, and X localization to the nuclear lamina. Which of these functions are needed for transcriptional inactivation? X chromosome silencing is enacted by exclusion of Pol II from the Xist compartment (Chaumeil et al., 2006). The general transcription factors TBP and TAF10 are also excluded (Chaumeil et al., 2006).

Among the proteins that interact directly with Xist, SHARP is a transcriptional repressor. SHARP binds SMRT, a component of a co-repressor complex that activates the HDAC3 histone deacetylase. SHARP, SMRT, and HDAC3 are all required for exclusion of Pol II from the Xist territory and for X inactivation (McHugh et al., 2015), suggesting that SHARP induces silencing through HDAC3. Recruitment of PRC2, which is required for maintenance of X inactivation, also depends on SHARP and HDAC3, though whether this recruitment occurs through a direct interaction is not known (McHugh et al., 2015). How the structure of the inactive X is related to transcriptional silencing also remains unclear. Changes in TAD structure and X localization are not sufficient for transcriptional silencing but may be involved in Xist spreading.

Instead of regulating Pol II access to the X chromosome, the *D. melanogaster* MSL complex increases efficiency of transcription elongation. GRO-seq measurements of nascent transcription showed that X-linked genes have higher Pol II density compared to autosomal genes (Ferrari et al., 2013; Larschan et al., 2011). This Pol II enrichment is dependent on MSL2 and increases towards the 3' end of genes, indicating that the MSL complex promotes transcriptional elongation. The heightened transcriptional efficiency is correlated with the presence of the active chromatin mark H4K16ac, which is catalyzed by MOF (Larschan et al., 2011). MOF deposits H4K16ac across gene bodies on the male X, resulting in enrichment of the mark at the 3' ends of genes as well as transcription start sites (TSSs). In contrast, on autosomes and female X chromosomes, H4K16ac is enriched only at TSSs (Kind et al., 2008).

Binding of the *D. melanogaster* MSL complex is not known to alter X chromosome compaction, TAD structure, or nuclear positioning. Instead of a chromosome-wide mechanism for transcriptional regulation as employed in *C. elegans*, genes are activated through a local mechanism. The distance from a gene to the nearest HAS is correlated with its degree of dosage compensation (Straub et al., 2008), and depleting MSL1, MSL3, or MOF specifically results in downregulation of genes that are bound by the MSL complex (Kind et al., 2008).

Conclusions

In conclusion, the diverse strategies that have evolved to balance X chromosome expression between sexes in worms, mammals, and flies illustrate that gene expression across a chromosome can be controlled through mechanisms that act either locally or chromosome-

wide by regulating either Pol II recruitment or elongation. Dosage compensation complexes can remodel X chromosome chromatin marks, TAD structure, overall compaction, and nuclear positioning. In each case, recruitment of histone modifying enzymes is clearly essential for transcriptional regulation. Analyzing the dosage compensation complex functions that repress or activate transcription over an entire chromosome provides insight into modes of gene regulation that would be not attainable by simply examining the regulation of individual genes.

References

Akhtar A, Becker PB. 2000. Activation of Transcription through Histone H4 Acetylation by MOF, an Acetyltransferase Essential for Dosage Compensation in Drosophila. *Molecular Cell* **5**:367–375. doi:10.1016/S1097-2765(00)80431-1

Albritton SE, Kranz A-L, Winterkorn LH, Street LA, Ercan S. 2017. Cooperation between a hierarchical set of recruitment sites targets the X chromosome for dosage compensation. *eLife Sciences* **6**:e23645. doi:10.7554/eLife.23645

Alekseyenko AA, Peng S, Larschan E, Gorchakov AA, Lee O-K, Kharchenko P, McGrath SD, Wang CI, Mardis ER, Park PJ, Kuroda MI. 2008. A Sequence Motif within Chromatin Entry Sites Directs MSL Establishment on the Drosophila X Chromosome. *Cell* **134**:599–609. doi:10.1016/j.cell.2008.06.033

Barr ML, Bertram EG. 1977. A Morphological Distinction between Neurones of the Male and Female, and the Behaviour of the Nucleolar Satellite during Accelerated Nucleoprotein Synthesis In: Persaud TVN, editor. Problems of Birth Defects: From Hippocrates to Thalidomide and After. Dordrecht: Springer Netherlands. pp. 101–102. doi:10.1007/978-94-011-6621-8_11

Belmont AS, Bignone F, Ts'O POP. 1986. The relative intranuclear positions of barr bodies in XXX non-transformed human fibroblasts. *Experimental Cell Research* **165**:165–179. doi:10.1016/0014-4827(86)90541-0

Bourgeois CA, Laquerriere F, Hemon D, Hubert J, Bouteille M. 1985. New data on the in situ position of the inactive X chromosome in the interphase nucleus of human fibroblasts. *Hum Genet* **69**:122–129. doi:10.1007/BF00293281

Brejc K, Bian Q, Uzawa S, Wheeler BS, Anderson EC, King DS, Kranzusch PJ, Preston CG, Meyer BJ. 2017. Dynamic Control of X Chromosome Conformation and Repression by a Histone H4K20 Demethylase. *Cell* **171**:85-102.e23. doi:10.1016/j.cell.2017.07.041

Brockdorff N. 2017. Polycomb complexes in X chromosome inactivation. *Phil Trans R Soc B* **372**:20170021. doi:10.1098/rstb.2017.0021

Brown CJ, Hendrich BD, Rupert JL, Lafrenière RG, Xing Y, Lawrence J, Willard HF. 1992. The human XIST gene: Analysis of a 17 kb inactive X-specific RNA that contains conserved repeats and is highly localized within the nucleus. *Cell* **71**:527–542. doi:10.1016/0092-8674(92)90520-M

Buscaino A, Köcher T, Kind JH, Holz H, Taipale M, Wagner K, Wilm M, Akhtar A. 2003. MOF-Regulated Acetylation of MSL-3 in the Drosophila Dosage Compensation Complex. *Molecular Cell* **11**:1265–1277. doi:10.1016/S1097-2765(03)00140-0

Cai Y, Jin J, Swanson SK, Cole MD, Choi SH, Florens L, Washburn MP, Conaway JW, Conaway RC. 2010. Subunit Composition and Substrate Specificity of a MOF-containing Histone Acetyltransferase Distinct from the Male-specific Lethal (MSL) Complex. *J Biol Chem* **285**:4268–4272. doi:10.1074/jbc.C109.087981

Chaumeil J, Baccon PL, Wutz A, Heard E. 2006. A novel role for Xist RNA in the formation of a repressive nuclear compartment into which genes are recruited when silenced. *Genes Dev* **20**:2223–2237. doi:10.1101/gad.380906

Chen C-K, Blanco M, Jackson C, Aznauryan E, Ollikainen N, Surka C, Chow A, Cerase A, McDonel P, Guttman M. 2016. Xist recruits the X chromosome to the nuclear lamina to enable chromosome-wide silencing. *Science* aae0047. doi:10.1126/science.aae0047

Chuang P-T, Albertson DG, Meyer BJ. 1994. DPY-27: A chromosome condensation protein homolog that regulates C. elegans dosage compensation through association with the X chromosome. *Cell* **79**:459–474. doi:10.1016/0092-8674(94)90255-0

Clemson CM, Hall LL, Byron M, McNeil J, Lawrence JB. 2006. The X chromosome is organized into a gene-rich outer rim and an internal core containing silenced nongenic sequences. *PNAS* **103**:7688–7693. doi:10.1073/pnas.0601069103

Crane E, Bian Q, McCord RP, Lajoie BR, Wheeler BS, Ralston EJ, Uzawa S, Dekker J, Meyer BJ. 2015. Condensin-driven remodelling of X chromosome topology during dosage compensation. *Nature* **523**:240–244. doi:10.1038/nature14450

Csankovszki G, Collette K, Spahl K, Carey J, Snyder M, Petty E, Patel U, Tabuchi T, Liu H, McLeod I, Thompson J, Sarkesik A, Yates J, Meyer BJ, Hagstrom K. 2009. Three Distinct Condensin Complexes Control C. elegans Chromosome Dynamics. *Current Biology* **19**:9–19. doi:10.1016/j.cub.2008.12.006

Darrow EM, Huntley MH, Dudchenko O, Stamenova EK, Durand NC, Sun Z, Huang S-C, Sanborn AL, Machol I, Shamim M, Seberg AP, Lander ES, Chadwick BP, Aiden EL. 2016. Deletion of DXZ4 on the human inactive X chromosome alters higher-order genome architecture. *Proc Natl Acad Sci USA* **113**:E4504-4512. doi:10.1073/pnas.1609643113

Davis TL, Meyer BJ. 1997. SDC-3 coordinates the assembly of a dosage compensation complex on the nematode X chromosome. *Development* **124**:1019–1031.

Dawes HE, Berlin DS, Lapidus DM, Nusbaum C, Davis TL, Meyer BJ. 1999. Dosage Compensation Proteins Targeted to X Chromosomes by a Determinant of Hermaphrodite Fate. *Science* **284**:1800–1804. doi:10.1126/science.284.5421.1800

Eils R. 1996. Three-dimensional reconstruction of painted human interphase chromosomes: active and inactive X chromosome territories have similar volumes but differ in shape and surface structure. *The Journal of Cell Biology* **135**:1427–1440. doi:10.1083/jcb.135.6.1427

Engreitz JM, Pandya-Jones A, McDonel P, Shishkin A, Sirokman K, Surka C, Kadri S, Xing J, Goren A, Lander ES, Plath K, Guttman M. 2013. The Xist lncRNA Exploits Three-Dimensional Genome Architecture to Spread Across the X Chromosome. *Science* **341**:1237973. doi:10.1126/science.1237973

Ercan S, Giresi PG, Whittle CM, Zhang X, Green RD, Lieb JD. 2007. X chromosome repression by localization of the *C. elegans* dosage compensation machinery to sites of transcription initiation. *Nature Genetics* **39**:403–408. doi:10.1038/ng1983

Ferrari F, Plachetka A, Alekseyenko AA, Jung YL, Ozsolak F, Kharchenko PV, Park PJ, Kuroda MI. 2013. "Jump Start and Gain" Model for Dosage Compensation in Drosophila Based on Direct Sequencing of Nascent Transcripts. *Cell Reports* **5**:629–636. doi:10.1016/j.celrep.2013.09.037

Figueiredo MLA, Kim M, Philip P, Allgardsson A, Stenberg P, Larsson J. 2014. Non-coding roX RNAs Prevent the Binding of the MSL-complex to Heterochromatic Regions. *PLOS Genetics* **10**:e1004865. doi:10.1371/journal.pgen.1004865

Froberg JE, Pinter SF, Kriz AJ, Jégu T, Lee JT. 2018. Megadomains and superloops form dynamically but are dispensable for X-chromosome inactivation and gene escape. *Nature Communications* **9**:5004. doi:10.1038/s41467-018-07446-w

Fudenberg G, Imakaev M, Lu C, Goloborodko A, Abdennur N, Mirny LA. 2016. Formation of Chromosomal Domains by Loop Extrusion. *Cell Reports* **15**:2038–2049. doi:10.1016/j.celrep.2016.04.085

Furuhashi H, Nakajima M, Hirose S. 2006. DNA supercoiling factor contributes to dosage compensation in Drosophila. *Development* **133**:4475–4483. doi:10.1242/dev.02620

Gdula MR, Nesterova TB, Pintacuda G, Godwin J, Zhan Y, Ozadam H, McClellan M, Moralli D, Krueger F, Green CM, Reik W, Kriaucionis S, Heard E, Dekker J, Brockdorff N. 2018. The non-canonical SMC protein SmcHD1 antagonises TAD formation on the inactive X chromosome. *bioRxiv* 342147. doi:10.1101/342147

Gelbart ME, Larschan E, Peng S, Park PJ, Kuroda MI. 2009. *Drosophila* MSL complex globally acetylates H4K16 on the male X chromosome for dosage compensation. *Nature Structural & Molecular Biology* **16**:825–832. doi:10.1038/nsmb.1644

Giorgetti L, Lajoie BR, Carter AC, Attia M, Zhan Y, Xu J, Chen CJ, Kaplan N, Chang HY, Heard E, Dekker J. 2016. Structural organization of the inactive X chromosome in the mouse. *Nature* **advance online publication**. doi:10.1038/nature18589

Gruenbaum Y, Margalit A, Goldman RD, Shumaker DK, Wilson KL. 2005. The nuclear lamina comes of age. *Nature Reviews Molecular Cell Biology* **6**:21–31. doi:10.1038/nrm1550

Hilfiker A, Hilfiker-Kleiner D, Pannuti A, Lucchesi JC. 1997. mof, a putative acetyl transferase gene related to the Tip60 and MOZ human genes and to the SAS genes of yeast, is required for dosage compensation in Drosophila. *The EMBO Journal* **16**:2054–2060. doi:10.1093/emboj/16.8.2054

Hirano T. 2016. Condensin-Based Chromosome Organization from Bacteria to Vertebrates. *Cell* **164**:847–857. doi:10.1016/j.cell.2016.01.033

Hsu DR, Chuang PT, Meyer BJ. 1995. DPY-30, a nuclear protein essential early in embryogenesis for Caenorhabditis elegans dosage compensation. *Development* **121**:3323–3334.

Ikegami K, Egelhofer TA, Strome S, Lieb JD. 2010. Caenorhabditis elegans chromosome arms are anchored to the nuclear membrane via discontinuous association with LEM-2. *Genome Biol* **11**:R120. doi:10.1186/gb-2010-11-12-r120

Jans J, Gladden JM, Ralston EJ, Pickle CS, Michel AH, Pferdehirt RR, Eisen MB, Meyer BJ. 2009. A condensin-like dosage compensation complex acts at a distance to control expression throughout the genome. *Genes Dev* **23**:602–618. doi:10.1101/gad.1751109

Jiang J, Jing Y, Cost GJ, Chiang J-C, Kolpa HJ, Cotton AM, Carone DM, Carone BR, Shivak DA, Guschin DY, Pearl JR, Rebar EJ, Byron M, Gregory PD, Brown CJ, Urnov FD, Hall LL, Lawrence JB. 2013. Translating dosage compensation to trisomy 21. *Nature* **500**:296–300. doi:10.1038/nature12394

Kind J, Vaquerizas JM, Gebhardt P, Gentzel M, Luscombe NM, Bertone P, Akhtar A. 2008. Genome-wide Analysis Reveals MOF as a Key Regulator of Dosage Compensation and Gene Expression in Drosophila. *Cell* **133**:813–828. doi:10.1016/j.cell.2008.04.036

Kruesi WS, Core LJ, Waters CT, Lis JT, Meyer BJ. 2013. Condensin controls recruitment of RNA polymerase II to achieve nematode X-chromosome dosage compensation. *eLife* **2**:e00808. doi:10.7554/eLife.00808

Lam KC, Mühlpfordt F, Vaquerizas JM, Raja SJ, Holz H, Luscombe NM, Manke T, Akhtar A. 2012. The NSL Complex Regulates Housekeeping Genes in Drosophila. *PLOS Genetics* **8**:e1002736. doi:10.1371/journal.pgen.1002736

Larschan E, Bishop EP, Kharchenko PV, Core LJ, Lis JT, Park PJ, Kuroda MI. 2011. X chromosome dosage compensation via enhanced transcriptional elongation in *Drosophila*. *Nature* **471**:115–118. doi:10.1038/nature09757

Lau AC, Nabeshima K, Csankovszki G. 2014. The C. elegans dosage compensation complex mediates interphase X chromosome compaction. *Epigenetics & Chromatin* **7**:31. doi:10.1186/1756-8935-7-31

Lieb JD, Albrecht MR, Chuang P-T, Meyer BJ. 1998. MIX-1: An Essential Component of the C. elegans Mitotic Machinery Executes X Chromosome Dosage Compensation. *Cell* **92**:265–277. doi:10.1016/S0092-8674(00)80920-4

Lieb JD, Capowski EE, Meneely P, Meyer BJ. 1996. DPY-26, a Link Between Dosage Compensation and Meiotic Chromosome Segregation in the Nematode. *Science* **274**:1732–1736. doi:10.1126/science.274.5293.1732

Lieberman-Aiden E, Berkum NL van, Williams L, Imakaev M, Ragoczy T, Telling A, Amit I, Lajoie BR, Sabo PJ, Dorschner MO, Sandstrom R, Bernstein B, Bender MA, Groudine M, Gnirke A, Stamatoyannopoulos J, Mirny LA, Lander ES, Dekker J. 2009. Comprehensive Mapping of Long-Range Interactions Reveals Folding Principles of the Human Genome. *Science* **326**:289–293. doi:10.1126/science.1181369

Loda A, Brandsma JH, Vassilev I, Servant N, Loos F, Amirnasr A, Splinter E, Barillot E, Poot RA, Heard E, Gribnau J. 2017. Genetic and epigenetic features direct differential efficiency of Xist-mediated silencing at X-chromosomal and autosomal locations. *Nature Communications* **8**:690. doi:10.1038/s41467-017-00528-1

McDonel P, Jans J, Peterson BK, Meyer BJ. 2006. Clustered DNA motifs mark X chromosomes for repression by a dosage compensation complex. *Nature* **444**:614–618. doi:10.1038/nature05338

McHugh CA, Chen C-K, Chow A, Surka CF, Tran C, McDonel P, Pandya-Jones A, Blanco M, Burghard C, Moradian A, Sweredoski MJ, Shishkin AA, Su J, Lander ES, Hess S, Plath K, Guttman M. 2015. The *Xist* lncRNA interacts directly with SHARP to silence transcription through HDAC3. *Nature* **521**:232–236. doi:10.1038/nature14443

Meller VH, Gordadze PR, Park Y, Chu X, Stuckenholz C, Kelley RL, Kuroda MI. 2000. Ordered assembly of roX RNAs into MSL complexes on the dosage-compensated X chromosome in Drosophila. *Current Biology* **10**:136–143. doi:10.1016/S0960-9822(00)00311-0

Mets DG, Meyer BJ. 2009. Condensins Regulate Meiotic DNA Break Distribution, thus Crossover Frequency, by Controlling Chromosome Structure. *Cell* **139**:73–86. doi:10.1016/j.cell.2009.07.035

Nonet ML, Meyer BJ. 1991. Early aspects of Caenorhabditis elegans sex determination and dosage compensation are regulated by a zinc-finger protein. *Nature* **351**:65–68. doi:10.1038/351065a0

Nozawa R-S, Boteva L, Soares DC, Naughton C, Dun AR, Buckle A, Ramsahoye B, Bruton PC, Saleeb RS, Arnedo M, Hill B, Duncan RR, Maciver SK, Gilbert N. 2017. SAF-A Regulates Interphase Chromosome Structure through Oligomerization with Chromatin-Associated RNAs. *Cell* **169**:1214-1227.e18. doi:10.1016/j.cell.2017.05.029

Pferdehirt RR, Kruesi WS, Meyer BJ. 2011. An MLL/COMPASS subunit functions in the C. elegans dosage compensation complex to target X chromosomes for transcriptional regulation of gene expression. *Genes Dev* **25**:499–515. doi:10.1101/gad.2016011

Raja SJ, Charapitsa I, Conrad T, Vaquerizas JM, Gebhardt P, Holz H, Kadlec J, Fraterman S, Luscombe NM, Akhtar A. 2010. The Nonspecific Lethal Complex Is a Transcriptional Regulator in Drosophila. *Molecular Cell* **38**:827–841. doi:10.1016/j.molcel.2010.05.021

Ramírez F, Lingg T, Toscano S, Lam KC, Georgiev P, Chung H-R, Lajoie BR, de Wit E, Zhan Y, de Laat W, Dekker J, Manke T, Akhtar A. 2015. High-Affinity Sites Form an Interaction Network to Facilitate Spreading of the MSL Complex across the X Chromosome in Drosophila. *Molecular Cell* **60**:146–162. doi:10.1016/j.molcel.2015.08.024

Rao SSP, Huntley MH, Durand NC, Stamenova EK, Bochkov ID, Robinson JT, Sanborn AL, Machol I, Omer AD, Lander ES, Aiden EL. 2014. A 3D Map of the Human Genome at Kilobase Resolution Reveals Principles of Chromatin Looping. *Cell* **159**:1665–1680. doi:10.1016/j.cell.2014.11.021

Scott MJ, Pan LL, Cleland SB, Knox AL, Heinrich J. 2000. MSL1 plays a central role in assembly of the MSL complex, essential for dosage compensation in Drosophila. *The EMBO Journal* **19**:144–155. doi:10.1093/emboj/19.1.144

Snyder MJ, Lau AC, Brouhard EA, Davis MB, Jiang J, Sifuentes MH, Csankovszki G. 2016. Anchoring of Heterochromatin to the Nuclear Lamina Reinforces Dosage Compensation-Mediated Gene Repression. *PLOS Genet* **12**:e1006341. doi:10.1371/journal.pgen.1006341

Straub T, Grimaud C, Gilfillan GD, Mitterweger A, Becker PB. 2008. The Chromosomal High-Affinity Binding Sites for the Drosophila Dosage Compensation Complex. *PLOS Genetics* **4**:e1000302. doi:10.1371/journal.pgen.1000302

Sural TH, Peng S, Li B, Workman JL, Park PJ, Kuroda MI. 2008. The MSL3 chromodomain directs a key targeting step for dosage compensation of the *Drosophila melanogaster* X chromosome. *Nature Structural & Molecular Biology* **15**:1318–1325. doi:10.1038/nsmb.1520

Torres EM, Williams BR, Amon A. 2008. Aneuploidy: Cells Losing Their Balance. *Genetics* **179**:737–746. doi:10.1534/genetics.108.090878

Towbin BD, González-Aguilera C, Sack R, Gaidatzis D, Kalck V, Meister P, Askjaer P, Gasser SM. 2012. Step-Wise Methylation of Histone H3K9 Positions Heterochromatin at the Nuclear Periphery. *Cell* **150**:934–947. doi:10.1016/j.cell.2012.06.051

Tsai CJ, Mets DG, Albrecht MR, Nix P, Chan A, Meyer BJ. 2008. Meiotic crossover number and distribution are regulated by a dosage compensation protein that resembles a condensin subunit. *Genes Dev* **22**:194–211. doi:10.1101/gad.1618508

Wang C-Y, Jégu T, Chu H-P, Oh HJ, Lee JT. 2018. SMCHD1 Merges Chromosome Compartments and Assists Formation of Super-Structures on the Inactive X. *Cell*. doi:10.1016/j.cell.2018.05.007

Wheeler BS, Anderson E, Frøkjær-Jensen C, Bian Q, Jorgensen E, Meyer BJ. 2016. Chromosome-wide mechanisms to decouple gene expression from gene dose during sex-chromosome evolution. *eLife* **5**:e17365. doi:10.7554/eLife.17365

Wutz A, Rasmussen TP, Jaenisch R. 2002. Chromosomal silencing and localization are mediated by different domains of *Xist* RNA. *Nature Genetics* **30**:167–174. doi:10.1038/ng820

Yonker SA, Meyer BJ. 2003. Recruitment of C. elegans dosage compensation proteins for gene-specific versus chromosome-wide repression. *Development* **130**:6519–6532. doi:10.1242/dev.00886

Zheng S, Villa R, Wang Jia, Feng Y, Wang Jinfeng, Becker PB, Ye K. 2014. Structural basis of X chromosome DNA recognition by the MSL2 CXC domain during Drosophila dosage compensation. *Genes Dev* **28**:2652–2662. doi:10.1101/gad.250936.114

Chapter 2
X chromosome dosage compensation and lifespan: interplay between chromosome structure and gene expression

Abstract

Interphase chromosomes are highly organized, but the mechanisms that establish higher order structures and their importance for transcription are not well understood. We investigated how chromosome architecture is established and its relationship to gene expression in the context of *Caenorhabditis elegans* X-chromosome dosage compensation, a process that modulates both gene expression and higher-order structure chromosome-wide to equalize gene expression between XO males and XX hermaphrodites. A dosage compensation complex (DCC) equalizes X expression by repressing transcription from the two hermaphrodite Xs by half while also establishing a unique structure composed of megabase-scale topologically associating domains (TADs). DCC-dependent TAD boundaries all contain a strong DCC binding site (*rex* site). We determined the requirements for creating a DCC-dependent boundary by making a series of *rex* site deletions and insertions and measuring the resulting chromosome structure. Single *rex* deletions eliminated the associated TAD boundaries. Furthermore, insertion of a *rex* site at a new location on X defined a new boundary, providing the first example of an inserted binding site creating a new TAD boundary. Therefore, DCC binding at a strong *rex* site is necessary and sufficient for boundary formation.

Deleting all eight of the *rex* sites at DCC-dependent boundaries recapitulated the TAD structure of a DCC mutant, though DCC binding remained at *rex* sites within TADs. Eliminating boundaries by deleting a series of cis elements uniquely allowed us to measure transcription when TAD structure was disrupted chromosome-wide but most DCC binding was retained. The 8 *rex* deletion worms lacked dosage compensation phenotypes, and embryos did not show changes in X chromosome expression, indicating that TAD boundaries are neither a cause nor consequence of X repression. The absence of TADs allowed us to identify additional DCC-mediated X chromosome structure. We discovered that the DCC promotes intrachromosomal DNA interactions X-chromosome-wide between loci within a megabase of each other, which may be important for transcriptional repression. Although disrupted TAD structure did not affect dosage compensation, it resulted in increased thermosensitivity, accelerated aging, and shortened lifespan, suggesting that while TADs are not required for proper gene expression in embryos, they are important for proper gene expression later in development.

Contributions

Phil Frankino, Ryo Higuchi-Sanabria, Qiming Yang, Qian Bian, Katie Podshivolova, and Aram Shin contributed to the experiments described in this chapter. I worked with Qian Bian to make *rex* site deletions and Qiming Yang to make *rex* site insertions. Qiming performed ChIP-seq experiments on *rex* insertion strains. Aram Shin performed Hi-C in one *rex* insertion strain. Hermaphrodite lifespan experiments and measurements of oxidative stress tolerance were performed by Phil Frankino and Ryo Higuchi-Sanabria in Andy Dillin's lab. Measurements of worm locomotion during aging using the multi-worm tracker were performed by Katie

Podshivolova in Cynthia Kenyon's lab. I performed all other Hi-C and ChIP-seq experiments, and all RNA-seq, male lifespans, thermotolerance assays, and data analysis.

Introduction

Genomes must be properly packaged to enable chromosomes to fit into the nucleus and be accessible for transcription, repair, and other functions. To meet these requirements, chromosomes are physically organized into a series of structures ranging from kilobase-scale chromatin loops to chromosome territories comprising hundreds of megabases. Unravelling the functions of these interrelated structures requires the ability to precisely manipulate the structures, which has been challenging because the DNA sequences and factors required for chromosome organization are not well understood.

Here we focus on topologically associating domains (TADs) of approximately one megabase that are characteristic of metazoan chromosomes. Loci within the same TAD tend to interact with each other while being insulated from interactions with loci in neighboring TADs. In mammalian cells, the boundaries between TADs are enriched for binding sites of proteins important for shaping chromosome architecture, including the structural maintenance of chromosomes (SMC) complex cohesin and the zinc-finger protein CTCF. These architectural proteins are necessary to establish boundaries, but the mechanisms by which they define the locations of boundaries are not known. Proteins important for TAD formation, such as cohesin, have other essential roles in processes like chromosome segregation, making evaluation of the functional significance of TADs challenging, especially at the organismal level.

We investigated how TADs are established and their relationship to gene expression in the context of *Caenorhabditis elegans* X-chromosome dosage compensation, a process that modulates both gene expression and higher-order structure chromosome-wide. The Dosage Compensation Complex (DCC), a specialized condensin complex, equalizes expression of X-linked genes between sexes by repressing transcription from the two hermaphrodite Xs by half to equal transcription from the single male X. The DCC also establishes a unique structure composed of TADs of approximately one megabase (Crane et al., 2015). In the absence of the DCC, X structure resembles the structure of autosomes with fewer, less regular TAD boundaries. DCC-dependent TAD boundaries all contain a single strong DCC recruitment site (*rex* site) (Crane et al., 2015). DCC binding near a particular gene is neither necessary nor sufficient for dosage compensation of that gene, indicating that the DCC acts at a distance to repress transcription, (Jans et al., 2009; Wheeler et al., 2016). Therefore, the DCC-dependent TAD structure could plausibly underlie the mechanism of gene repression.

Mechanisms employed by the DCC to remodel the topology of X chromosomes and define TADs are likely to be broadly relevant because condensin and other SMC complexes play key roles in shaping chromosome architecture in eukaryotes and prokaryotes. For example, cohesin is required for the formation of most TAD boundaries in mammalian cells (Rao et al., 2017; Schwarzer et al., 2017), condensin compacts mitotic chromosomes (Gibcus et al., 2018), and SMC-condensin resolves newly replicated sister origins from each other during DNA replication in *Bacillis subtilis* (Wang et al., 2017). In addition to the condensin subunits, the DCC includes proteins important for assembly of the complex onto X (SDC-2 and SDC-3) and a histone demethylase (DPY-21) responsible for enriching the histone mark H4K20me1 on X. Loss of H4K20me1 enrichment results in both partial disruption of dosage compensation and weakening of DCC-dependent TAD boundaries (Brejc et al., 2017)

In principle, the loss of TAD boundaries in the absence of the DCC could be either a cause or consequence of transcriptional changes. In mammalian cells, when disruption of a TAD

boundary results in merging of adjacent TADs, enhancers can physically interact with additional genes and ectopically activate them (Franke et al., 2016; Lupiáñez et al., 2015). However, defining the general relationship between TAD structure and transcription has been challenging because architectural proteins that establish TADs (like the DCC in *C. elegans* or CTCF and cohesin in mammalian cells) also bind and function at other locations outside TAD boundaries, making it unclear whether the transcriptional changes resulting from their depletion are caused exclusively by altered TAD structure or other functions of the proteins. In other contexts, transcription can control chromosome structure. In Caulobacter, transcription drives the formation of boundaries between chromosomal interaction domains (Le and Laub, 2016).

We identified the requirements for creating a DCC-dependent boundary by making a series of *rex* site deletions and insertions and measuring the resulting chromosome structure. Single *rex* deletions eliminated the associated TAD boundaries, revealing that DCC binding at a strong *rex* site is necessary for boundary formation. Insertion of a *rex* site at a new location on X defined a new boundary, indicating that DCC binding at a boundary is sufficient to define the boundary. Deleting all eight of the *rex* sites at DCC-dependent boundaries recapitulated the TAD structure of a DCC mutant. These *8rexΔ* animals provided a unique opportunity to measure transcription when TAD structure was disrupted across an entire chromosome but most DCC binding was retained. The *8rexΔ* worms lacked dosage compensation phenotypes, and embryos did not show changes in X chromosome expression, indicating that TAD structure is not responsible for dosage compensation. The absence of TADs allowed us to identify additional DCC-mediated X chromosome structure. We discovered that the DCC promotes DNA interactions across the X between loci within a megabase, both within TADs and across TAD boundaries. These interactions may be important for transcriptional repression. Although TAD organization does not mediate dosage compensation, abrogating TAD structure by deleting *rex* sites resulted in accelerated aging, shortened lifespan, and reduced thermotolerance, suggesting a role for chromosome structure in regulating stress and aging programs.

Results

Each DCC-dependent boundary was eliminated by deleting the single *rex* site at the boundary

To dissect the mechanisms by which the DCC establishes TAD boundaries, we analyzed the potential contributions of multiple factors to the formation of these boundaries. First, the presence of a strong *rex* site at every DCC-dependent boundary suggested that DCC binding at these *rex* sites may define the location of boundaries. Second, DCC-mediated interactions between DCC-dependent boundaries are among the strongest long-range interactions on the X chromosome, suggesting that boundary formation could require not only DCC binding at *rex* sites, but also interactions between adjacent DCC-dependent boundaries. Intra-TAD *rex-rex* interactions mediated by the DCC are among the strongest interactions within TADs, raising the possibility that DCC-dependent intra-TAD interactions could help hold domains together, passively creating boundaries.

We first evaluated the role of DCC binding to *rex* sites at boundaries. Using Cas9, we sequentially deleted the single *rex* site located at each of the eight DCC-dependent TAD boundaries (Figure 1A). Seven *rex* sites are in intergenic regions, and each *rex* deletion removed 400-1100 bp, encompassing all motifs known to be important for DCC binding. The exception

(*rex-33*) is located in the final intron of the essential gene *mom-1* (Thorpe et al., 1997), causing us to delete the 1300-bp intron in its entirety. To verify that the deletions eliminated DCC binding, we performed ChIP-seq using antibodies for the DCC-specific SMC protein DPY-27 and a non-condensin DCC subunit, SDC-3, which is required for binding of all condensin subunits to X. Binding of both DPY-27 and SDC-3 was lost entirely at the deleted sites, while DCC binding at the remaining *rex* sites remained intact (Figure 1—figure supplement 1).

We examined the effects of *rex* deletions on chromosome structure by performing in situ Hi-C on three categories of embryos: wild-type embryos, a series of mutant embryos with increasing numbers of *rex* deletions, and *sdc-2* mutant embryos lacking DCC binding to X. Previous FISH experiments showed that deleting *rex-47* greatly diminished the associated TAD boundary (Crane et al., 2015). We confirmed this result by Hi-C. We compared distance-normalized Hi-C interactions (Z scores) between *rex-47Δ* and wild-type embryos and found an increase in interactions across the deleted *rex* site (Figure 1B), confirming boundary loss. To quantify the extent of loss, we created X chromosome insulation profiles, as described previously (Crane et al., 2015). To generate an insulation profile, we calculated an insulation score for each locus across X by summing all Hi-C interactions within a 500-kb window surrounding that locus. When comparatively few interactions occur across a locus, it has a low insulation score. Such a local minimum in the insulation profile is defined as a TAD boundary. *rex-47* resides at a local minimum in the wild-type insulation profile, and the valley was eliminated in *rex-47Δ*, indicating complete loss of the TAD boundary (Figure 1B). Thus, high DCC occupancy at the *rex* site defined the location of the boundary.

Next, we examined *3rexΔ*, in which the two *rex* sites (*rex-14* and *rex-8*) located at the boundaries flanking *rex-47* were deleted along with *rex-47*. All three boundaries in the center of X were eliminated (Figure 1C), providing the opportunity to ask whether the strongest *rex* sites that define boundaries impede weaker sites from doing so. When these three strongest *rex* sites were deleted, no new boundaries emerged in the center of X at the weaker *rex* sites, indicating that strong *rex* sites do not inhibit weaker rex sites from forming boundaries. Similarly, in *6rexΔ*, in which three additional *rex* sites on the right end of X were deleted, the TAD boundaries were eliminated at the additional deleted sites, and no new boundaries emerged at remaining *rex* sites (Figure 1D).

Deleting all eight *rex* sites at the DCC-dependent boundaries recapitulated the chromosome-wide disrupted TAD structure of the *sdc-2(y93, RNAi)* embryonic lethal mutant, which lacks DCC binding on X. In both the *8rexΔ* and DCC mutants, seven TAD boundaries were eliminated, and the boundary at *rex-32* was dramatically weakened (Figure 1E-I), while autosomal boundaries were unchanged (Figure 1—figure supplement 2A-E). Although the DCC remained bound at dozens of other sites across the X chromosome in *8rexΔ* embryos, removing only the eight *rex* sites at DCC-dependent TAD boundaries disrupted the TAD structure of X comparably to the structure in DCC mutant embryos. The thorough disruption of DCC-dependent TAD boundaries allowed us to examine DCC-dependent structure separate from TADs that remains in *8rexΔ*.

The DCC mediates specific interactions between pairs of *rex* sites, including *rex* sites at TAD boundaries and *rex* sites within TADs (Crane et al., 2015). DCC-mediated interactions between non-boundary *rex* sites remained in *8rexΔ*, indicating that these interactions are not sufficient to create TADs. To evaluate how interactions between the remaining *rex* sites were

affected when the boundary sites were removed, we examined interactions among the 30 *rex* sites with the highest DCC occupancy, excluding the eight boundary *rex* sites. These 22 other *rex* sites exhibited DCC-dependent interactions, and interactions increased in the absence of DCC-dependent TADs (Figure 1J). The increase resulted from higher interactions both across the deleted boundaries and between *rex* sites within the same TAD (Figure 1—figure supplement 2F-G). Therefore, interactions between non-boundary *rex* sites are not sufficient to create TADs. Instead, DCC binding at the eight *rex* sites at DCC-dependent boundaries is essential to define the location of TADs.

Inserting a single *rex* site creates a new boundary on X

We next explored whether a single *rex* site is sufficient to create a boundary. In the *8rexΔ* chromosome, which lacks all DCC-dependent boundaries, we inserted a *rex* site (*rex-32*) that makes a boundary at its endogenous location into a new location in the middle of X that is 250 kb from the nearest boundary (Figure 2A). The inserted *rex* site bound the DCC at a level comparable to its endogenous location (Figure 2—figure supplement 2A), and it defined a new boundary of similar strength to the boundary at its endogenous site (Figure 2B,C,F). Therefore, a single high-affinity DCC binding site is sufficient to create a TAD boundary on X. This boundary is the sole DCC-dependent boundary on the chromosome, revealing that boundary formation does not require interactions between DCC-dependent boundaries.

A second *rex* site (*rex-8*) inserted 1.4 Mb downstream of the newly inserted *rex-32* site also defined a new TAD boundary (Figure 2D-F). In this case, the inserted *rex-32* interacted with *rex-8*. In the presence of this boundary-to-boundary interaction, the boundary at *rex-32* was weakened slightly compared to embryos with only the single *rex-32* insertion (Figure 2F). Therefore, interactions between adjacent DCC-dependent boundaries do not contribute to boundary strength.

To investigate whether a *rex* site is sufficient to create a new boundary in the context of the wild-type 3D architecture, we inserted *rex-32* into a new, non-boundary location on the right side of the wild-type X chromosome. Again, *rex-32* recruited the DCC at a level similar to that at its endogenous location (Figure 2—figure supplement 2B) and defined a new boundary (Figure 2G). Therefore, the wild-type X structure is not fully constrained and can be further subdivided into new domains when an additional *rex* site is inserted.

Because a single strong *rex* site is sufficient to create a boundary at a new location, we assessed whether all high-occupancy *rex* sites block DNA interactions between the loci flanking the *rex* sites. The DCC-dependent change in insulation score at a *rex* site is highly correlated with the level of SDC-3 binding (Figure 2—figure supplement 1B), and the eight *rex* sites that define boundaries are among the 13 highest occupancy SDC-3 binding sites in the genome. Five additional *rex* sites with higher SDC-3 binding than *rex-47* did not form boundaries but did show a relative increase in insulation score in DCC mutants, indicating an increase in interactions between loci flanking the *rex* sites. (Figure 2—figure supplement 1A). Thus, DCC binding at these non-boundary *rex* sites does indeed alter chromosome structure. However, DCC binding may be insufficient to create strong boundaries due to unknown factors that modulate TAD structure (such as lamin binding), or DCC-dependent boundary formation may be overwhelmed by very strong DCC-independent boundaries nearby.

We also inserted three *rex* sites from the center of X (*rex-14*, *rex-47*, and *rex-8*) into the center of chromosome I with the same spacing as on X. We used the *3rexΔ* background in which these *rex* sites were deleted from X to allow unique mapping of reads to the new insertion locations. ChIP-seq analysis revealed that the inserted *rex* sites recruited the DCC, but with only about 20 percent of the binding as that at their endogenous locations on X (Figure 2—figure supplement 2C). The inserted *rex* sites did not create boundaries on chromosome I (Figure 2—figure supplement 2D-F). The lack of new boundaries is consistent with the observation that *rex* sites on X with the same low level of DCC binding do not define TAD boundaries, but we cannot rule out whether some other unique characteristic of X chromosomes, such as widespread DCC binding or H4K20me1 enrichment, is necessary for DCC-dependent boundary formation.

Together, our results establish that the DCC forms boundaries through high-occupancy binding at *rex* sites located at the boundaries and not through intra-TAD interactions. A single inserted *rex* site is sufficient to define a boundary at a new location on X, and interactions with a second inserted *rex* site do not strengthen the boundary, revealing that interactions with other boundaries are not necessary to form a boundary.

Adding and subtracting boundaries affects the strength of neighboring and distant boundaries

Our series of deletions provided a unique setting to investigate how adding and subtracting boundaries affects the strength of neighboring and distant boundaries. We found, for example, that in *8rexΔ* versus *6rexΔ* chromosomes the four DCC-independent TAD boundaries flanking the two additional *rex* deletions became stronger (Figure 2—figure supplement 3A). Composite profiles showed that, overall, when a boundary was deleted, the adjacent boundaries were strengthened (p=0.02, paired T test; Figure 2H), while boundaries two away from deleted boundaries showed no consistent pattern of change (p=0.60, Figure 2H).

Conversely, when a new boundary was created, the adjacent boundaries were weakened. For example, when the inserted *rex-32* established a new TAD boundary in the center of the *8rexΔ* chromosome, the upstream DCC-independent boundary became weaker. Furthermore, the local minimum in the *8rexΔ* insulation profile downstream of the site for *rex-32* insertion disappeared upon insertion of *rex-32* (Figure 2F). Changes in the strength of DCC-independent boundaries resulting from alteration of DCC-dependent boundaries reveal that a boundary can influence the strength of an adjacent boundary even when boundaries are established through different mechanisms.

Boundary deletions can also have long-range effects on the strength of distant boundaries. For example, when *rex* sites were deleted on the right side of X, boundaries on the left side of the chromosome were altered (Figure 2—figure supplement 3B). Thus, deletions can affect the strength of boundaries over 10 Mb away. The intricate interplay between distant boundaries highlights the complexity of predicting the long-range effects of altering chromosome structure and suggests the intriguing possibility that perturbation of one site could affect the functions of broad genomic regions.

DCC binding at strong *rex* sites induces DCC binding nearby

rex insertions and deletions allowed us to examine how removing strong DCC binding sites affects DCC binding across the X chromosome. Information about changes in DCC binding

caused by deleting eight strong *rex* sites is important for teasing apart the effect of TAD boundary loss on gene expression from any effect of reduced DCC binding.

Thousands of DCC peaks of varying strengths are detectable on X by ChIP-seq analysis (Albritton et al., 2017; Crane et al., 2015). These peaks represent two categories of DCC binding sites: recruitment sites (*rex* sites), which bind the complex autonomously even when not on X chromosomes, and secondary sites called *dox* sites (dependent on X), which exhibit DCC binding only when on X chromosomes. Recruitment sites are distinguished by their sequence composition and chromatin environment (Albritton et al., 2017; Ercan et al., 2007; Jans et al., 2009; Pferdehirt et al., 2011). ChIP-seq experiments cannot differentiate whether *rex* sites are the initial entry point for loading the DCC onto X chromosomes or whether the complex is first loaded at other locations and accumulates at *rex* sites. Furthermore, the mechanisms by which the DCC is distributed across X chromosomes are not known.

We determined whether loss of strong *rex* sites affects nearby DCC binding by calculating the ratio of SDC-3 and DPY-27 binding on *8rexΔ* versus wild-type X chromosomes. Binding of both DCC components was reduced up to 16-fold immediately adjacent to the deletions and gradually returned to wild-type levels at ~20 kb on either side of the deleted sites (Figure 3A-B, Figure 3—figure supplement 1A-G). Binding was reduced at small peaks near the deleted sites as well as in the intervening non-peak regions, revealing that DCC binding does not occur exclusively at locations where ChIP-seq peaks are detected. Beyond 20 kb from the deleted *rex* sites, DCC binding was generally retained on the *8rexΔ* chromosome, providing an opportunity to measure how gene expression is affected when the DCC is assembled onto X but TADs are disrupted.

Similarly, we compared DCC binding around *rex* sites inserted in new locations on *8rexΔ* X chromosomes to binding on *8rexΔ* chromosomes lacking the *rex* insertion. DCC binding was enriched ~16 fold around the inserted sites, and binding gradually decreased to wild-type levels ~15 kb from the insertions (Figure 3C,D, Figure 3—figure supplement 1H). Together, loss of DCC binding around deleted sites and gain around inserted sites suggest that one mechanism by which the DCC is distributed across the chromosome is by spreading several kilobases from strong *rex* sites.

TADs do not mediate transcriptional repression during dosage compensation

To determine whether disrupted X chromosome structure alters dosage compensation, we initially inspected the *8rexΔ* worms for dosage compensation defects. Complete disruption of dosage compensation causes XX-specific embryonic lethality, and weak disruption of dosage compensation causes dumpy (Dpy) and egg-laying defective (Egl) phenotypes. Dosage compensation defects can also be detected by a sensitive genetic assay. Mutations in *xol-1*, the master regulator of sex determination and dosage compensation, are lethal to males because the DCC binds inappropriately to the single X and represses its expression. *xol-1* mutant males are rescued by mutations that disrupt the dosage compensation process. *8rexΔ* worms do not display any of these dosage compensation phenotypes. They have a normal brood size, and 100 percent of the animals are viable and not Dpy or Egl (Supplementary Table 1). The deletions do not rescue *xol-1* mutant males (see Methods).

To assay dosage compensation more thoroughly and directly, we measured gene expression genome-wide. Disrupting the TAD structure of an entire chromosome by deleting a

series of binding sites rather than depleting a protein provided a unique opportunity to observe the effects on gene expression when chromosome structure is altered but the majority of DCC binding remains. We preformed RNA-seq on mixed-stage embryos of three genotypes: wild-type, *8rexΔ*, and a DCC mutant lacking DCC binding on X.

Assaying embryos allowed us to measure elevation in X expression in a severe dosage compensation mutant (*sdc-2(y93, RNAi)*) before the animals died. However, using embryos required carefully matching the stages of the embryo populations between genotypes. The X chromosome is silenced in the germline (Fong et al., 2002; Kelly et al., 2002; Tzur et al., 2018), and as silencing is lost in early embryos, average expression of genes on X increases for approximately the first five hours of embryogenesis while autosome expression remains steady (Figure 4—figure supplement 1A). Therefore, comparing populations of embryos that are not precisely stage matched could introduce X-chromosome-wide artifacts in the analysis of transcript levels (Figure 4—figure supplement 1B). To avoid such confounding factors, we first determined whether embryogenesis proceeds at the same rate in *8rexΔ* and wild-type animals by filming embryos during their development. The average time to progress from comma to two-fold stage and then to hatching was identical (Figure 4—figure supplement 1C), indicating that embryogenesis occurs with similar timing.

For each RNA-seq replicate, we attempted to harvest stage-matched populations of embryos by growing worms and collecting embryos of all genotypes in parallel. We then computationally compared the age distribution of wild-type and *8rexΔ* embryo populations by assessing expression levels of autosomal genes that change during development (see Methods). We selected the five best-matched wild-type and *8rexΔ* replicates, excluding other replicates in which the wild-type embryos clearly had higher expression of late genes and lower expression of early genes compared to *8rexΔ*.

We found that while median X expression was elevated 1.5-fold in the DCC mutant compared to wild type, genes on X were not overexpressed in *8rexΔ* (median fold change 0.97 compared to wild type) (Figure 4A-B). Consistent with previous measurements (Crane et al., 2015; Kruesi et al., 2013), average expression in the DCC mutant was elevated less than two-fold, which may be because genes are dosage compensated to varying degrees, because the DCC had not yet loaded in the youngest embryos, and because the mutant condition may not have completely depleted the protein. No individual genes showed significant differential expression between wild-type and *8rexΔ* embryos.

To determine whether a relationship exists between changes in TAD boundaries and transcription, we calculated the average change in gene expression in a 400-kb sliding window along the X chromosome. No correlation between change in expression and distance to a DCC-dependent boundary was evident in either *8rexΔ* or DCC mutant embryos (Figure 4C). Genes within 100 kb of an altered boundary did not show dramatic expression differences compared to genes farther from a boundary, though the limited number of expressed genes near boundaries precludes a definitive comparison. These observations reinforce the conclusion that dosage compensation is a chromosome-wide process that represses genes across X regardless of their proximity to altered TAD boundaries (Crane et al., 2015). In both *8rexΔ* and DCC mutant embryos, X chromosome TAD boundaries were lost, but X-linked expression was elevated in the DCC mutant and unchanged in *8rexΔ*. Therefore, DCC-dependent TADs are neither a cause nor

consequence of transcriptional repression; the changes in chromosome topology and gene expression result from two separate roles of the DCC.

The DCC promotes interactions at the scale of 0.1-1 Mb independently of TAD boundary formation

The complete disruption of DCC-dependent TAD boundaries on *8rexΔ* chromosomes not only revealed that dosage compensation occurs without TAD organization, it allowed us to discover DCC-dependent structure separate from TADs that could be important for long-range transcriptional repression. By comparing the X topology of DCC mutant embryos to *8rexΔ* embryos, we identified DCC-dependent structure that is retained in the absence of TADs. We found that in DCC mutants, interactions were lost across the X chromosome between loci within ~1 Mb of the diagonal compared to interactions in *8rexΔ* embryos, while the pattern of interactions on autosomes was unchanged (Figure 5A,B,F). We visualized interactions at different length scales by plotting the average interaction frequencies between loci at increasing distances. The interaction frequencies scale with genomic distance, with different slopes at different length scales (Figure 5—figure supplement 1). This "scaling factor" was shallowest for loci separated by 0.1 – 1 Mb, and the X chromosome had more interactions than autosomes at these distances, while X and autosomes had matching scaling factors below 0.1 Mb and over 1 Mb (Figure 5C). The 0.1 – 1 Mb interactions on X are mediated by the DCC, as evidenced by X-chromosome interactions matching autosome interactions in the DCC mutant (Figure 5E). X chromosome-wide reduction in interactions in the DCC mutant was also reflected in the insulation profile, which was shifted down relative to that of wild-type and *8rexΔ* chromosomes (Figure 5A). In *8rexΔ* embryos, the higher interactions on X compared to autosomes remained, indicating that they occur independently of TAD structure (Figure 5D). Therefore, in addition to creating TAD boundaries, the DCC confers a unique structure on X by promoting interactions at the scale of hundreds of kb.

The DCC also compacts the overall volume of the X chromosome territory (Brejc et al., 2017; Lau et al., 2014). To determine whether this compaction is specifically due to the DCC's function in establishing TAD structure, we measured the volume of the X chromosome using immunofluorescence for DPY-27 in intestines of wild-type, *8rexΔ*, and *dpy-21(null)* adults. *dpy-21(null)* is a viable DCC mutant in which all other components of the DCC load, but expression is elevated, and the worms are Dpy (Brejc et al., 2017; Yonker and Meyer, 2003). As shown previously (Brejc et al., 2017; Lau et al., 2014), the volume of the X chromosome territory expanded in *dpy-21(null)* compared to wild type. The volume was unchanged in *8rexΔ* (Figure 5G). Therefore, the DCC-mediated compaction of the X chromosome territory is unrelated to TAD structure but could reflect the increased chromatin interactions at 0.1 – 1 Mb.

The DCC's dual functions in establishing boundaries and compacting chromatin at the 100-kb scale are consistent with a mechanism in which the DCC creates TADs and compacts chromosomes through loop extrusion. In this model, a factor extrudes a chromatin loop of increasing size until it reaches a barrier element, which halts extrusion (Fudenberg et al., 2016). When loop extruders load across a chromosome, they create loops at many loci, which is reflected by increased interactions at the length scale of loops. Because the loops do not cross the extrusion barriers, the barriers delineate boundaries between TADs. Our mutant phenotypes are consistent with the condensin portion of the DCC acting as a loop extruder that

is halted when the DCC encounters high affinity *rex* sites. Although the TADs per se are not essential for dosage compensation, the loop extrusion that facilitates TAD formation promotes DNA interactions in the 0.1-1 Mb range that might be important for compaction and transcriptional repression during dosage compensation.

Destroying DCC-dependent TADs results in reduced thermotolerance and accelerated aging

Although disrupting X structure did not result in statistically significant changes in gene expression in embryos under normal growth conditions, we found that chromosome architecture is important for the gene expression programs activated by heat stress. When worms are exposed to heat stress, the presence of unfolded proteins triggers the expression of hundreds of genes, including chaperones important for protein refolding (Brunquell et al., 2016). Similarly, the presence of unfolded proteins in the endoplasmic reticulum (ER) or mitochondria triggers transcriptional upregulation of genes involved in restoring homeostasis to those organelles (Higuchi-Sanabria et al., 2018). To judge whether *8rexΔ* worms can successfully tolerate proteotoxic stress and induce these transcriptional programs, we first heat stressed worms at 37°C during day 1 of adulthood and measured their survival. After seven hours, survival of *8rexΔ* adults was significantly lower than that of wild-type adults ($p=0.01$, paired T test, Figure 6A).

In contrast, the *8rexΔ* worms did not show increased sensitivity to other proteotoxic stresses. We induced ER unfolded protein stress using tunicamycin, which causes accumulation of unfolded glycoproteins in the ER, and we induced mitochondrial unfolded protein stress using paraquat, which causes accumulation of reactive oxygen species. The *8rexΔ* worms were not more sensitive to these stresses than wild type worms (Figure 6B and 6C). Therefore, removing DCC-dependent TAD structure specifically impairs thermotolerance but does not generally compromise the response to all forms of proteotoxic stress.

To assess whether *rex* deletions affect additional aspects of adult worm performance, we measured the lifespan of *8rexΔ* animals. Median lifespan of *8rexΔ* hermaphrodites was 18 days, compared to 22 days for wild-type hermaphrodites (Figure 6D). This significant shortening ($p<0.0001$, Mantel-Cox test) is comparable to the lifespan defect observed in mutants of *daf-16*, a key transcription factor that integrates signals from the insulin/IGF-1 and other signaling pathways to regulate genes involved in lifespan and stress responses (Calo et al., 2018; Lin et al., 2001). Lifespans of *8rexΔ* and wild-type males were equivalent at 15 days (Figure 6E), indicating that the lifespan defect of *8rexΔ* hermaphrodites is sex-dependent and DCC-dependent. The defect is therefore a bona fide consequence of disrupting DCC-dependent *rex* function, rather than a consequence of defects in DCC-independent processes caused either by *rex* deletions or an off-target mutation introduced during deletion of *rex* sites.

To judge whether the *8rexΔ* worms die prematurely from an aging defect instead of general "sickness" throughout development, we used a multi-worm tracker to measure locomotory speed and behavior during adulthood. Wild-type worms show a characteristic decline in locomotion throughout adulthood. We found that hermaphrodite *8rexΔ* worms move normally at day 1 of adulthood, but their movement then declines more rapidly than that of wild-type worms.

The decline was evident in both the speed of normal explorative movement in the absence of a stimulus and the speed of movement in response to delivering a controlled

mechanical stimulus (the tap of the plate) (Figure 6F and G, Figure 6—figure supplement 1D and E). A tap elicits multifaceted behavior: worms increase their speed, reverse the direction of motion, and then turn. We quantified this escape response by delivering the stimulus and measuring the worms' speed (which reflects their fastest movement ability) and distance traveled backward (the magnitude of the escape response). By both metrics, the escape response declined more rapidly during adulthood of *8rexΔ* mutants than wild-type animals (Figure 6G and H). In general, the response of *8rexΔ* mutants to a stimulus declined faster than their unstimulated movement.

We also monitored animal size during adulthood (Figure 6--figure supplement 1F). Wild-type animals continue to increase in size for the first six days of adulthood and then shrink. Although the *8rexΔ* mutants were the same size as wild-type animals at adult day 1 and increased in size somewhat until day 6, they never reached the same size as wild-type animals, and they shrank in size faster (Figure 6—figure supplement 1F).

The precipitous decline in explorative locomotive speed, maximal escape speed, magnitude of escape response, and body size, despite all of these metrics being similar between *8rexΔ* and wild-type worms on day 1 of adulthood, indicates that *8rexΔ* worms are healthy at the onset of adulthood but have a rapid-aging phenotype. These results suggest that although aberrant chromosome structure does not affect gene expression early in development, the aging program is misregulated later in development.

The reduced thermotolerance and accelerated aging could be due to expression changes of a few genes on X with roles in these processes. Alternatively, the phenotypes could result from the cumulative effect of misregulation of many genes, as in aneuploid cells in which overexpression of genes from an entire chromosome causes proteotoxic stress regardless of which chromosome is aneuploid (Oromendia and Amon, 2014). To distinguish between these possibilities, we measured the lifespan of worms with subsets of the eight *rex* sites deleted. The full reduction in lifespan observed in *8rexΔ* is seen when only *rex-32* and *rex-33* (at the leftmost two boundaries) were deleted, while deleting the other six *rex* sites had no effect on lifespan (Figure 6D). Therefore, the aging defect is likely caused by specific misregulated genes in proximity to *rex-32* or *rex-33*, rather than a cumulative consequence of many changes across the entire chromosome. Deleting either *rex-32* or *rex-33* individually did not reduce lifespan as dramatically as the two deletions together (Figure 6—figure supplement 1A). The reduction in lifespan is therefore due to a combined effect of the two *rex* deletions, presumably involving misregulation of multiple genes.

Discussion

Metazoan chromosomes are organized into megabase-scale TADs, but the mechanisms that establish the domains and their relationship to gene expression are not well understood. Unlike other studies that have abolished TAD structure by depleting a protein that is essential for boundary formation and also plays other roles in gene expression and development, we eliminated DCC-dependent TAD boundaries across the X chromosome by deleting a series of DCC binding sites. We discovered that the DCC-dependent TAD structure of *C. elegans* X chromosomes is established by DCC binding to eight high-occupancy sites (Figure 1). DCC binding at a single *rex* site is necessary and sufficient for TAD boundary formation (Figure 2). By disrupting TAD structure while leaving most DCC binding intact, we found that TAD boundaries

are neither a cause nor consequence of transcriptional repression during dosage compensation (Figure 4). We also uncovered a new feature of DCC-dependent chromosome structure, which is not dependent on TAD boundaries: the DCC promotes DNA interactions at the scale of 0.1 – 1 Mb, which could be responsible for gene repression (Figure 5). Although disrupted TAD structure does not affect dosage compensation, it results in increased thermosensitivity, accelerated aging, and shortened lifespan (Figure 6), suggesting that TADs are important for proper gene expression under stress conditions.

Mechanism of TAD boundary formation

We discovered the requirements for establishing DCC-dependent TAD boundaries by making a series of *rex* site deletions and insertions. Strong *rex* sites define the location of DCC-dependent boundaries, and a single *rex* site inserted into a new location on X is sufficient to define a new TAD boundary (Figure 2). These results rule out a model in which intra-TAD interactions hold the domain together and the boundaries are defined passively. Although strong interactions are often observed between DCC-dependent boundaries and between adjacent boundaries in mammalian cells, we found that interactions between boundaries are not required for boundary formation. This observation provides strong experimental evidence for the conclusion from simulations of chromosome interactions that TADs are not formed by single, stable boundary-to-boundary loops (Fudenberg et al., 2016).

Instead of a model in which specific DCC-mediated interactions are important for boundary formation, our results are consistent with the popular loop extrusion model for TAD boundary formation and chromosome compaction. In this model, a factor extrudes a chromatin loop of increasing size until it reaches a barrier element, which blocks progression of the extrusion (Fudenberg et al., 2016). When loop extruders load across a chromosome, they create loops at many loci, which is reflected in increased interactions at the length scale of the loop size. Because the loops do not cross extrusion barriers, the barriers delineate boundaries between TADs. In mammalian cells, evidence points to the SMC complex cohesin acting as a loop extruder while binding of the zinc finger protein CTCF to DNA blocks extrusion (Fudenberg et al., 2018), and the SMC complex condensin can extrude DNA loops in vitro (Ganji et al., 2018).

Our results fulfill all the predictions for the DCC, a condensin complex, acting as a loop extruder while eight strong *rex* sites act as extrusion barriers. First, eliminating an extrusion barrier should eliminate the boundary, and each *rex* deletion did indeed abolish the associated boundary. Second, inserting an extrusion barrier at a new location should delineate a new boundary, and we found that *rex* sites inserted in three new locations on X each create a new boundary. In contrast, in mouse embryonic fibroblasts, CTCF recruitment to a new location failed to create a new boundary (Barutcu et al., 2018). Third, eliminating the loop extruder should result in TAD boundary loss and an overall reduction in interactions at the length scale of the loops (Fudenberg et al., 2018) as we observe in the DCC mutant. Finally, removal of extrusion barriers is predicted to eliminate TADs while leaving other DCC-mediated interactions unchanged. Indeed, in *8rexΔ*, TAD boundaries are lost, but overall 0.1 – 1 Mb interactions on X remain.

Multiple DCC components likely function as the loop extruder and extrusion barrier, analogous to the roles played by cohesin and CTCF in boundary formation in mammalian cells.

Perhaps the condensin portion of the DCC extrudes chromatin loops analogously to cohesin while non-condensin components of the complex (such as SDC-2 and SDC-3) bind independently at *rex* sites. The extruding complex could then be halted by bound SDC proteins (Figure 7). It is also possible that the SDC subunits, which are required for condensin loading, move with the condensin, and extrusion is halted by strong binding of the SDC subunits to a *rex* site. A loop extrusion model for DCC movement along the chromosome also provides an explanation for how the DCC subunit DPY-21, a histone demethylase, enriches H4K20me1 across the X chromosome. DPY-21 could travel with the extruding condensin complex, providing access for DPY-21 to demethylate H4K20me2 at all loci across X regardless of proximity to high-occupancy DCC binding sites.

TADs and transcription

Because the DCC acts at a distance to repress transcription on X, DCC-dependent TAD organization was an attractive candidate for mediating the process of long-range, chromosome-wide dosage compensation. However, we found that disrupting megabase-scale TAD structure while retaining most DCC binding and DCC-mediated interactions does not cause dosage compensation phenotypes nor significantly change X-linked expression in embryos (Figure 4). Therefore, TAD structure itself does not repress or activate transcription.

In mammalian cells, loss of a TAD boundary can change transcription by allowing enhancers to ectopically activate genes that were previously in separate TADs (Lupiáñez et al., 2015; Valton and Dekker, 2016), but this mode of regulation by TAD boundaries is likely limited to specific genes. Studies that eliminated TADs genome-wide by depleting cohesin, the cohesin loader, or CTCF found modest expression changes for hundreds of genes, but no widespread ectopic activation (Nora et al., 2017; Rao et al., 2017; Schwarzer et al., 2017). Similarly, we found no broad activation of genes on the *C. elegans* X chromosome when TADs were eliminated. Mechanisms involving ectopic activation of a gene by an enhancer in an adjacent TAD after boundary disruption may not be relevant in *C. elegans.* Although putative enhancers have been identified (Chen et al., 2013; Daugherty et al., 2017; Jänes et al., 2018), no long-range interactions are known to activate gene expression. Additionally, the *C. elegans* genome is gene-dense, with an average of 158 protein-coding genes per TAD on X (Spieth et al., 2014), compared to approximately seven protein-coding genes per TAD in the human genome (Dowen et al., 2014).

Our study expands on previous work by separating the consequences of eliminating TAD boundaries from other defects caused by removing multi-functional architectural proteins that create TADs. Interpreting the effects of depleting proteins essential for TAD boundary formation is difficult because the proteins also bind locations outside of TAD boundaries and likely alter gene expression and other biological processes through multiple mechanisms. For example, after one day of CTCF depletion in mouse embryonic stem cells, the majority of the genes with reduced expression had CTCF bound within 1 kb of the transcription start site (though they were not specifically positioned at TAD boundaries), suggesting that CTCF may activate gene expression by binding promoters rather than merely establishing TADs (Nora et al., 2017). By deleting a series of DCC binding sites, we found that binding of an architectural protein indeed has distinct functions at different genomic locations. DCC binding to *rex* sites at TAD boundaries is necessary for creation of the boundaries, but the binding at other locations,

and resulting DCC-mediated structure unrelated to TADs, is sufficient for transcriptional repression.

TAD-independent DCC-mediated architecture

Comparing *8rexΔ* to DCC mutant X chromosome structure provided an opportunity to identify additional aspects of DCC-dependent architecture (not related to TAD boundaries) that may be important for gene repression. We discovered that the DCC promotes chromatin interactions at the 0.1 to 1 Mb length scale. The loss of these interactions in the DCC mutant is consistent with the effect of removing SMC complexes in other contexts. Loss of cohesin loading in mouse cells and loss of condensin in yeast both result in reduced interactions at distances below 200 kb (Paul et al., 2018; Schwarzer et al., 2017).

The DCC-mediated interactions at the hundred-kb scale are a plausible mechanism for enacting transcriptional repression because they occur chromosome-wide, consistent with observations that degree of repression is not correlated with a gene's distance from a *rex* site or TAD boundary (Crane et al., 2015; Jans et al., 2009; Wheeler et al., 2016) (Figure 4). Perhaps the increased interactions are indicative of the DCC creating an X chromosome compartment with an environment unfavorable to polymerase recruitment. If the DCC-mediated interactions at the hundred-kb scale drive dosage compensation, then repression is achieved not by loops between specific loci but through a dynamic ensemble of loops that varies between individual cells. DCC binding across the chromosome, not only at *rex* sites, is needed for this chromosome-wide structure that may be important for gene expression.

Chromosome structure and lifespan

Although loss of DCC-dependent TADs does not compromise dosage compensation, DCC binding at TAD boundaries is necessary for normal lifespan and thermotolerance, suggesting that chromosome structure is important for proper gene expression in some contexts. Gene expression changes that cause thermosensitivity may not be detectable by RNA-seq in embryos because they include increased transcriptional variance undetectable in a population measurement or because loss of TAD structure could interfere with the cells' ability to rapidly upregulate expression of genes on X that function during heat shock but not normal growth. The *8rexΔ* phenotypes could be a cumulative effect of subtle changes in many genes that together disrupt proteostasis, making worms less able to tolerate heat stress and aging. However, our finding that the reduced lifespan is due to deleting only the two left-most boundary *rex* sites favors the idea that a few specific genes in proximity to *rex-32* and *rex-33* are responsible for the phenotypes. Genes that are induced in response to heat shock or that change in expression during aging are potential candidates for controlling the phenotypes. In a genome-wide study, 815 genes were upregulated in wild-type worms after heat shock (Brunquell et al., 2016) including 149 on the X and 40 in the TADs surrounding *rex-32* and *rex-33*. In a study of gene expression during wild-type aging, expression of 1309 genes changed significantly between the first and twelfth days of adulthood, including 237 genes on X and 78 in the TADs surrounding *rex-32* and *rex-33* (Jänes et al., 2018). The reduced thermotolerance, shortened lifespan, and accelerated aging resulting from disrupted chromosome architecture are likely caused by a combined effect of misregulating multiple of these candidate genes.

Methods

C. elegans strains

Description	Strain name	Genotype	Source
Wild type	N2	Wild type	*Caenorhabditis* Genetics Center
DCC mutant	TY0810 grown on *sdc-2* RNAi bacteria	*sdc-2(y93, RNAi)*	(Miller et al., 1988)
dpy-21(null)	TY3936	*dpy-21(e428)*	(Yonker and Meyer, 2003)
rex-32Δ	TY5648	*rex-32(y572) X*	(Lo et al., 2013)
rex-47Δ	TY5815	*rex-47(y671) X*	(Crane et al., 2015)
rex-32Δ rex-33Δ	TY5826	*rex-32(y572) rex-33 (y743) X*	This study
3rexΔ	TY5818	*rex-14(y738) rex-47(y671) rex-8(y737) X*	This study
6rexΔ	TY5824	*rex-14(y738) rex-47(y671) rex-8(y737) rex-43(y741) rex-48(y742) rex-35(y740) X*	This study
8rexΔ	TY5827	*rex-32(y572) rex-33(y743) rex-14(y738) rex-47(y671) rex-8(y737) rex-43(y741) rex-48(y742) rex-35(y740) X*	This study
xol-1Δ	TY5755	*xol-1(y684) X*	This study
8rexΔ xol-1Δ	TY5828	*rex-32(y572) rex-33(y743) rex-14(y738) xol-1(y744) rex-47(y671) rex-8(y737) rex-43(y741) rex-48(y742) rex-35(y740) X*	This study
8rexΔ plus *rex-32*	TY5868	*rex-32(y572) rex-33(y743) yIs197 rex-14(y738) rex-47(y671) rex-8(y737) rex-43(y741) rex-48(y742) rex-35(y740) X*	This study
8rexΔ plus *rex-32 & rex-8*	TY5872	*rex-32(y572) rex-33(y743) yIs197 rex-14(y738) yIs201 rex-47(y671) rex-8(y737) rex-43(y741) rex-48(y742) rex-35(y740) X*	This study
rex-32 insert	TY5854	*dpy-27(y679) III; yIs187 X*	This study
3rexΔ plus *rex-47* on I	TY5859	*yIs190 I; rex-14(y738) rex-47(y671) rex-8(y737) X*	This study

3rexΔ plus *rex-8* & *rex-47* on I	TY5860	*yIs190 yIs192 I; rex-14(y738) rex-47(y671) rex-8(y737) X*	This study
3rexΔ plus rex-14, *rex-8* & *rex-47* on I	TY5867	*yIs196 yIs190 yIs192 I; rex-14(y738) rex-47(y671) rex-8(y737) X*	This study

Worm growth

Worms were grown at 20°C on either NGM plates with HB101 bacteria, NGM plates with OP50 bacteria, or RNAi plates (NGM agar with 1 mM IPTG and 100 µg/mL carbenicillin) with HT115 bacteria with an RNAi plasmid (*sdc-2* or L4440 negative control). Bacteria were grown as in (Crane et al., 2015). To collect embryos, starved L1s were plated on bacteria and grown at 20°C for three days. The gravid adults were then bleached to isolate mixed-stage embryos. When *sdc-2(y93)* worms were grown on RNAi bacteria from L1 stage, their progeny died as embryos or L1s.

rex deletions and insertions

rex-32 and *rex-47* deletions have been previously published (Crane et al., 2015; Lo et al., 2013). All other *rex* deletions and insertions were made using CRISPR/Cas9. To generate *6rexΔ*, the right six *rex* sites at DCC-dependent boundaries were sequentially deleted, and the resulting strain was outcrossed four times using TY0456 *dpy-6(e14) unc-3(e151) X*. To generate *rex-32Δ rex-33Δ*, *rex-33* was deleted in TY5648 (in which *rex-32* is deleted) and outcrossed three times using *lon-2(e678) X*. To build *8rexΔ*, *6rexΔ* was crossed to *rex-32Δ rex-33Δ* and recombinant F2s with all eight *rex* deletions were selected. All other strains used for Hi-C experiments were outcrossed at least two times.

For *rex-14*, *rex-8*, *rex-43*, *rex-48*, and *rex-35* deletions, worms were injected with plasmids encoding Cas9 and the sgRNA along with either a plasmid or oligo repair template as in (Farboud and Meyer, 2015). Repair templates consisted of a 6 bp NcoI restriction site flanked by homology arms (500-1000 bp for plasmids or at least 50 bp for oligos). Each deletion replaced the *rex* site with a 6 bp NcoI restriction site (to facilitate screening for deletions). The *rex-33* deletion was made using a Cas9 RNP along with an oligo repair template (Farboud et al., 2018), and all *rex* site insertions were made as in (Farboud et al., 2018) using the Cas9 RNP, gBlocks (IDT) with ~200 bp homology arms as repair templates, and either *dpy-10* or *rol-6* co-conversion markers. The locations and sizes of insertions and deletions and guide RNA sequences are listed below.

site	**Deletion location**	**Deletion size (bp)**	**Genomic location**	**gRNA**
rex-32	X:2996734-2997626	892	intergenic	constructed using TALENs (Lo et al., 2013)
rex-33	X:6296494-6297792	1298	final intron of *mom-1*	ccatttacatttggcgcagg and taacttattttacagaaaac

rex-14	X:8035969-8037090	1121	intergenic	atccacattactgtggttgg and cctttcacaacactcttttttc
rex-8	X:11093785-11094686	901	intergenic	agttgaaacaccatggagcgg and gcaacttatcggtgtcgcgg
rex-47	X:9465542-9465960	418	intergenic	GTAGTCACACCGAATTGATA (Crane et al., 2015)
rex-43	X:13700642-13701123	481	intergenic	ttggattgtgttcatcgtgg and aatgtcattaggttaaatg
rex-48	X:14525672-14526080	408	intergenic	ccagcatttttgagtgctt
rex-35	X:16681790-16682252	462	intergenic	ctatatacatgtttgaaac and tgttattctatttctaaag

***rex* site**	**Insertion location**	**Inserted sequence**	**Insertion size (bp)**	**gRNA**
rex-32	X:7812122	X:2996832-2997424	592	gtagaatgctccgtgtatgg
rex-8	X:9198531	X:11093928-11094681	754	agtggactccatcacactgg
rex-14	I:5448650	X:8036158-8036657	500	atttactgccaaacaggggg
rex-47	I:6858675	X:9465601-9466019	419	ttccaaatcaggccgtaggg
rex-8	I:8507023	X:11093891-11094686	796	cgtggtagtggtagaagcgg
rex-32	X:15574677	X:2996832-2997424	592	ttatgtagtctctttcagtg

Hi-C and analysis

Wild-type and *rex* site deletion and insertion worms were grown on NGM plates with HB101 bacteria and *sdc-2(y93)* worms were grown on RNAi plates with *sdc-2* RNAi bacteria. In situ Hi-C was performed on mixed staged embryos and data processed as in (Brejc et al., 2017). Hi-C was performed for two biological replicates of wild type, TY5815 *rex-47Δ*, TY5824 *6rexΔ*, TY5827 *8rexΔ*, and TY0810 DCC mutant and a single replicate for TY5818 *3rexΔ*, TY5868 *8rexΔ plus rex-32*, TY5872 *8rexΔ plus rex-32 & rex-8*, TY5854 *rex-32* insert, TY5859 *3rexΔ* plus *rex-47* on I, TY5860 *3rexΔ* plus *rex-47 & rex-8* on I, and TY5867 *3rexΔ* plus *rex-14, rex-47 & rex-8* on I. Z score subtraction heatmaps were generated by comparing single Hi-C replicates of each genotype. Patterns of boundary loss and gain were completely reproducible between replicates. For strains with two replicates, interaction frequencies after iterative correction from the two replicates were combined. Insulation plots, 3D plots, boundary pileups in Figure 2H, and scaling plots were generated using the combined replicates. To calculate the X chromosome *3rexΔ* insulation plot in Figure 1C, single replicates of two strains with identical X chromosome genotypes were combined: TY5818 *3rexΔ* and TY5860 *3rexΔ* plus *rex-47 & rex-8* on I. Average interaction frequencies at increasing distances in Figure 3C-E were calculated using fragment-level (unbinned) contacts using the *hiclib* library for Python (https://bitbucket.org/mirnylab/hiclib).

ChIP-seq

Wild-type, *8rexΔ*, TY5872 *8rexΔ* plus *rex-32* & *rex-8*, and TY5867 *3rexΔ* plus *rex-14*, *rex-8* & *rex-47* on I strains were grown on RNAi plates with HT115 bacteria, and approximately 0.5 g of mixed-stage embryos were isolated as above and frozen in liquid nitrogen. Embryos were washed once in 2% formaldehyde in M9 buffer and then fixed for 30 minutes with gentle rocking in 50 ml 2% formaldehyde in M9 buffer. Embryos were washed in 10mM Tris-HCl (pH 7.5) and then in FA buffer (150 mM NaCl, 50 mM HEPES-KOH pH 7.6, 1 mM EDTA, 1% Triton X-100, 0.1% sodium deoxycholate) and resuspended in FA buffer with protease inhibitors (5 mM DTT, protease inhibitor cocktail, 1 mM PMSF) to a total volume of 1 ml. Embryos were ground with 50 strokes in a 2 ml dounce homogenizer. Sarkosyl was added to a final concentration of 0.1% and chromatin was sheared in an S2 Covaris with duty cycle 20%, intensity 8, and 200 cycles/burst for 30 cycles of 60 s with 45 s of rest for a total time of 52 minutes. The extract was centrifuged at maximum speed for 15 minutes at 4°C. Supernatant containing approximately 2 mg total protein was incubated with 6.6 µg rabbit polyclonal anti-DPY-27 (rb699) (Chuang et al., 1994), rat polyclonal anti-SDC-3 (PEM4A) (Crane et al., 2015), or random IgG antibodies overnight at 4°C in a volume of at least 500 µl. 50 µl of Protein A Dynabeads (ThermoFisher Scientific, 10002D) were washed in FA buffer three times, added to the immunoprecipitation, and mixed at 4°C for at least 2 hours. Beads were then washed, DNA eluted, and libraries prepared as in (Kruesi et al., 2013). Libraries were sequenced with 50 bp reads on an Illumina HiSeq4000 platform.

ChIP-seq analysis

Adapters were trimmed using cutadapt version 1.2.1 (Martin, 2011) and reads were then aligned to the ce11 genome using bowtie2 version 2.3.0 (Langmead and Salzberg, 2012) with default settings. For comparisons involving strains with *rex* site insertions, the reference genome was modified to incorporate the *rex* insertions. Reads were sorted using SAMtools version 1.3.1 (Li et al., 2009) and read coverage was calculated by normalizing the read number in each 50 bp bin to the total read number using the bamCoverage function in deepTools version 2.5.0.1 (Ramírez et al., 2016) with the "normalizeUsingRPKM" option. Wild-type and *8rexΔ* analyses were performed with two combined biological replicates, and one replicate was used for TY5872 *8rexΔ* plus *rex-32* & *rex-8* and TY5867 *3rexΔ* plus *rex-14*, *rex-8* & *rex-47*.

To calculate the number of reads mapping to each *rex* site, SDC-3 peaks were first identified using macs2 version 2.1.1 (Zhang et al., 2008) with IgG as the control and the mfold parameter set to 3 50. The total SDC-3 reads in a 400 bp window surrounding each peak were summed and the IgG reads in the same window were subtracted. The peaks were then ranked based on this read number and the strongest 30 peaks (which were all on chromosome X) were used for analyses (*rex-48, rex-8, rex-23, rex-14, rex-32, rex-33, rex-43, rex-35, rex-16, rex-40, Prex-30, rex-45, rex-47, rex-34, Prex-7, rex-41, Prex-22, rex-6, rex-2, Prex-31, rex-24, rex-44, rex-36, Prex-6, rex-1, rex-42, Prex-1, rex-46, rex-39*).

To quantify DCC binding at inserted *rex* sites, reads were mapped to reference genomes modified to include the insertions (and deletions of the endogenous sites). Reads were summed in a 400 bp window around the peak of the inserted *rex* site as well as around four strong *rex* sites on X (*rex-40*, *rex-23*, *rex-16*, and *Prex-30*). Binding was normalized by dividing binding at the inserted *rex* site by the average binding at the other four *rex* sites.

The bigwigCompare function in deepTools version 2.5.0.1 (Ramírez et al., 2016) was used to calculate the $\log_2$ ratio of DCC binding between genotypes, and the median ratio in a 1 kb sliding window was plotted. Ratios were not calculated for the basepairs in the deletions or insertions.

ChIP-qPCR

ChIP-qPCR was used to quantify DCC binding at *rex-32* inserted in the wild-type background. ChIP using anti-SDC-3 antibody was performed on three biological replicates of mixed-stage TY5854 embryos as described above. After elution, DNA was diluted 3-fold and qPCR was performed using SYBR green (BioRad iQ SYBR Green Supermix 170–8886) on a BioRad CFX384 Real-Time System. The following oligos were used to measure binding 50 bp from the *rex-32* insertion, at the endogenous *rex-32*, and at other strong *rex* sites used for normalization (*rex-8*, *rex-16*, *rex-48*, and *rex-35*).

chrX_15574551F	CAGCGTAGTTGCTGACACTTAATGGTTC
chrX_15574627R	CTTTTAAGCAGTCGTCATGTACGTGTTCG
rex-32_F	CACTCCCCAGCTAATTTGGA
rex-32_R	TTCCCTTGTTGCGGAGATAG
rex-8_F	TTTATCCACCAACATGCATAAG
rex-8_R	CAGTGGATAACTACACAAGGG
rex-16_F	GTACAAACGCAGGGAAGAGA
rex-16_R	GACGCTACCACACCTTCAATA
rex-48_F	CTGCGCGATAGGCAATAGT
rex-48_R	GCACAATTCCAAGTCATCCATAC
rex-35_F	CCATATGTTGCCCAATGTTCC
rex-35_R	CGCAGGGAACATCAAATTAGTC

Standard curves were generated using input DNA, and binding at each *rex* site was calculated as a percentage of input. Binding at the inserted *rex-32* in Figure 2—figure supplement 2 was normalized to the average binding at five strong *rex* sites (*rex-32*, *rex-8*, *rex-16*, *rex-48*, and *rex-35*).

Measuring X chromosome volume

Intestines of adults (2 days post-L4) grown on OP50 bacteria were stained with anti-DPY-27 antibody (rb699) (Chuang et al., 1994) and DAPI, confocal images were scanned and deconvolved, and X chromosome volume was calculated as in (Brejc et al., 2017).

RNA-seq library preparation and analysis

For each RNA-seq replicate, worms were grown and embryos collected for all genotypes in parallel. Worms were grown on RNAi plates with HT115 bacteria with either *sdc-2* RNAi (for DCC mutant) or L4440 empty vector (for wild type and *8rexΔ*). For some replicates, mixed-stage embryos (majority pre-comma stage) were isolated by bleaching gravid hermaphrodites as above. Other replicates were skewed towards older embryos by bleaching young adults (68-70 hours after plating L1s) to isolate young embryos, letting the embryos develop at 20° for 7-8 hours until the majority were at the three-fold stage, and then freezing. RNA was isolated and

RNA-seq libraries were prepared as in (Brejc et al., 2017), and libraries were sequenced with 50 bp reads on an Illumina HiSeq4000 platform.

Reads were processed by trimming adapters using cutadapt version 1.2.1, aligning to the ce11 reference genome using TopHat version 2.1.1, and assembling using Cufflinks version 2.2.1 (Trapnell et al., 2012).

The wild-type and *8rexΔ* replicates that were most closely stage-matched were computationally identified. A published dataset that measured gene expression in single embryos through embryogenesis (whole embryo timecourse from (Hashimshony et al., 2015)) was used to select autosomal genes that had at least 1 transcript per million at some point in the time course and had at least a 20-fold change from their lowest to highest expression level. The expression levels for each of these 12,750 genes were scaled by subtracting the gene's mean expression and dividing by its standard deviation. The genes were k-means clustered into five clusters with similar temporal expression patterns using the kmeans function in R (Figure 5—figure supplement 1D). For each paired replicate of wild type and *8rexΔ*, expression of genes in each of the five clusters was compared between genotypes, and the five replicates in which the two genotypes had similar expression levels for genes in each cluster were selected. Two replicates of mixed-stage embryos and three replicates of late embryos were included, and other replicates in which the wild-type embryos clearly had higher expression of late genes and lower expression of early genes compared to *8rexΔ* were excluded. For the *sdc-2(y93, RNAi)* to wild type comparison, two replicates of mixed-stage embryos and one replicate of older embryos were used.

Replicates were combined using Cuffmerge and expression levels (fpkm) and fold changes were analyzed using cummeRbund version 2.20.0.

xol-1 rescue

A 3,035 bp deletion of the *xol-1* open reading frame (X:8041318-8043793) was made in the *rex* deletion background using Cas9 with two sgRNAs (GCTTCAACCTGCATTTCTGG and TGATTGATATGGGAAATGG). Ten *8rexΔ xol-1Δ* hermaphrodites were crossed to wild-type males, and the cross progeny were all either healthy hermaphrodites or inviable embryos. No viable male F1s were observed in the ten broods (approximately 3000 progeny), indicating that *8rexΔ* does not rescue *xol-1Δ* males.

Imaging timing of embryogenesis

To measure the timing of wild-type and *8rexΔ* embryogenesis, embryos of both genotypes were imaged simultaneously. 3.5 µl of a 1:10 dilution of Cell-Tak (Corning, catalog # 354240) and 1.8 µl of 1N NaOH were combined and 3 µl were pipetted onto a coverslip. After the coverslips dried, 2 µl of poly-L-lysine solution were added and allowed to dry, and coverslips were rinsed with ethanol and then water. Two-cell embryos of the first genotype in M9 buffer were transferred onto the Cell-Tak spot and aligned using an eyebrow hair. After the embryos settled, the coverslip was rinsed with M9 and the positions of the embryos were imaged. Two-cell embryos of the second genotype were then placed on a 2% agarose pad. The coverslip was placed on the agarose pad and sealed with rubber cement. Each embryo was imaged every 3 minutes for 13 hours using the Mark and Find function on a Leica SP8 WLL confocal microscope with a 20x objective in a room that was 22-23°C. The image of the embryos of the first

genotype was used to identify the genotype of each embryo, and the times when each embryo reached comma stage, completed two-fold stage, and hatched were determined. A total of 19 embryos of each genotype were imaged, over three separate days.

Thermotolerance

For each genotype, ten Day 1 adults were placed on each of five RNAi plates with HT115 bacteria. The plates were incubated at 37° and the number of living and dead worms counted after 5, 7, and 9 hours, with any worms that crawled onto the sides of the plates censored. At 5 hours, most worms were still alive, and by 9 hours, nearly all were dead, so the percentage of worms alive at 7 hours was reported for nine replicates performed on separate days.

Sensitivity to mitochondrial stress

Wild-type and *8rexΔ* worms were synchronized by bleaching and grown to day 1 of adulthood on empty vector HT115 bacteria. For a control with elevated mitochondrial stress tolerance, wild-type worms were grown on *daf-2* RNAi bacteria. For each condition, five worms were placed in each of 12 wells containing 50 µl of freshly prepared 0.2 M paraquat dichloride hydrate (Millipore Sigma 36541) in S-basal media (0.1 M NaCl, 0.05 M potassium phosphate pH 6, 5 µg/ml cholesterol), for a total of 60 worms. Worms were incubated at 20°C in a dark box. Every two hours, the number surviving worms was scored by observing each worm for movement (thrashing, pharyngeal pumping, etc.) for 15-20 seconds.

Lifespan analysis

Lifespan experiments were performed as in (Baird et al., 2014) using worms fed on HT115 bacteria. For male lifespan analysis, each male was placed on an individual plate. Sensitivity to ER stress was assayed by measuring lifespan on plates containing 20 ng/µl tunicamycin.

Worm tracking

Worm movement during aging was measured using a Multi-Worm Tracker as in (Podshivalova et al., 2017). Worms were grown on plates containing 50 µM FUDR to prevent progeny from developing. Worms were tracked every day or every other day for 1260 s with a tap stimulus after 900 s. For each genotype, eight plates each with 50 worms were tracked.

References

Albritton SE, Kranz A-L, Winterkorn LH, Street LA, Ercan S. 2017. Cooperation between a hierarchical set of recruitment sites targets the X chromosome for dosage compensation. *eLife Sciences* **6**:e23645. doi:10.7554/eLife.23645

Baird NA, Douglas PM, Simic MS, Grant AR, Moresco JJ, Wolff SC, Yates JR, Manning G, Dillin A. 2014. HSF-1–mediated cytoskeletal integrity determines thermotolerance and life span. *Science* **346**:360–363. doi:10.1126/science.1253168

Barutcu AR, Maass PG, Lewandowski JP, Weiner CL, Rinn JL. 2018. A TAD boundary is preserved upon deletion of the CTCF-rich Firre locus. *Nature Communications* **9**:1444. doi:10.1038/s41467-018-03614-0

Brejc K, Bian Q, Uzawa S, Wheeler BS, Anderson EC, King DS, Kranzusch PJ, Preston CG, Meyer BJ. 2017. Dynamic Control of X Chromosome Conformation and Repression by a Histone H4K20 Demethylase. *Cell* **171**:85-102.e23. doi:10.1016/j.cell.2017.07.041

Brunquell J, Morris S, Lu Y, Cheng F, Westerheide SD. 2016. The genome-wide role of HSF-1 in the regulation of gene expression in Caenorhabditis elegans. *BMC Genomics* **17**:559. doi:10.1186/s12864-016-2837-5

Calo E, Gu B, Bowen ME, Aryan F, Zalc A, Liang J, Flynn RA, Swigut T, Chang HY, Attardi LD, Wysocka J. 2018. Tissue-selective effects of nucleolar stress and rDNA damage in developmental disorders. *Nature* **554**:112–117. doi:10.1038/nature25449

Chen RA-J, Down TA, Stempor P, Chen QB, Egelhofer TA, Hillier LW, Jeffers TE, Ahringer J. 2013. The landscape of RNA polymerase II transcription initiation in C. elegans reveals promoter and enhancer architectures. *Genome Res* **23**:1339–1347. doi:10.1101/gr.153668.112

Chuang P-T, Albertson DG, Meyer BJ. 1994. DPY-27: A chromosome condensation protein homolog that regulates C. elegans dosage compensation through association with the X chromosome. *Cell* **79**:459–474. doi:10.1016/0092-8674(94)90255-0

Crane E, Bian Q, McCord RP, Lajoie BR, Wheeler BS, Ralston EJ, Uzawa S, Dekker J, Meyer BJ. 2015. Condensin-driven remodelling of X chromosome topology during dosage compensation. *Nature* **523**:240–244. doi:10.1038/nature14450

Daugherty AC, Yeo RW, Buenrostro JD, Greenleaf WJ, Kundaje A, Brunet A. 2017. Chromatin accessibility dynamics reveal novel functional enhancers in C. elegans. *Genome Res* **27**:2096–2107. doi:10.1101/gr.226233.117

Dowen JM, Fan ZP, Hnisz D, Ren G, Abraham BJ, Zhang LN, Weintraub AS, Schuijers J, Lee TI, Zhao K, Young RA. 2014. Control of Cell Identity Genes Occurs in Insulated Neighborhoods in Mammalian Chromosomes. *Cell* **159**:374–387. doi:10.1016/j.cell.2014.09.030

Ercan S, Giresi PG, Whittle CM, Zhang X, Green RD, Lieb JD. 2007. X chromosome repression by localization of the *C. elegans* dosage compensation machinery to sites of transcription initiation. *Nature Genetics* **39**:403–408. doi:10.1038/ng1983

Farboud B, Jarvis E, Roth TL, Shin J, Corn JE, Marson A, Meyer BJ, Patel NH, Hochstrasser ML. 2018. Enhanced Genome Editing with Cas9 Ribonucleoprotein in Diverse Cells and Organisms. *JoVE (Journal of Visualized Experiments)* e57350–e57350. doi:10.3791/57350

Farboud B, Meyer BJ. 2015. Dramatic Enhancement of Genome Editing by CRISPR/Cas9 Through Improved Guide RNA Design. *Genetics*. doi:10.1534/genetics.115.175166

Fong Y, Bender L, Wang W, Strome S. 2002. Regulation of the Different Chromatin States of Autosomes and X Chromosomes in the Germ Line of C. elegans. *Science* **296**:2235–2238. doi:10.1126/science.1070790

Franke M, Ibrahim DM, Andrey G, Schwarzer W, Heinrich V, Schöpflin R, Kraft K, Kempfer R, Jerković I, Chan W-L, Spielmann M, Timmermann B, Wittler L, Kurth I, Cambiaso P, Zuffardi O, Houge G, Lambie L, Brancati F, Pombo A, Vingron M, Spitz F, Mundlos S. 2016. Formation of new chromatin domains determines pathogenicity of genomic duplications. *Nature* **538**:265–269. doi:10.1038/nature19800

Fudenberg G, Abdennur N, Imakaev M, Goloborodko A, Mirny LA. 2018. Emerging Evidence of Chromosome Folding by Loop Extrusion. *Cold Spring Harb Symp Quant Biol* 034710. doi:10.1101/sqb.2017.82.034710

Fudenberg G, Imakaev M, Lu C, Goloborodko A, Abdennur N, Mirny LA. 2016. Formation of Chromosomal Domains by Loop Extrusion. *Cell Reports* **15**:2038–2049. doi:10.1016/j.celrep.2016.04.085

Ganji M, Shaltiel IA, Bisht S, Kim E, Kalichava A, Haering CH, Dekker C. 2018. Real-time imaging of DNA loop extrusion by condensin. *Science* eaar7831. doi:10.1126/science.aar7831

Gibcus JH, Samejima K, Goloborodko A, Samejima I, Naumova N, Nuebler J, Kanemaki MT, Xie L, Paulson JR, Earnshaw WC, Mirny LA, Dekker J. 2018. A pathway for mitotic chromosome formation. *Science* **359**:eaao6135. doi:10.1126/science.aao6135

Hashimshony T, Feder M, Levin M, Hall BK, Yanai I. 2015. Spatiotemporal transcriptomics reveals the evolutionary history of the endoderm germ layer. *Nature* **519**:219–222. doi:10.1038/nature13996

Higuchi-Sanabria R, Frankino PA, Paul JW, Tronnes SU, Dillin A. 2018. A Futile Battle? Protein Quality Control and the Stress of Aging. *Developmental Cell* **44**:139–163. doi:10.1016/j.devcel.2017.12.020

Jänes J, Dong Y, Schoof M, Serizay J, Appert A, Cerrato C, Woodbury C, Chen R, Gemma C, Huang N, Kissiov D, Stempor P, Steward A, Zeiser E, Sauer S, Ahringer J. 2018. Chromatin accessibility dynamics across C. elegans development and ageing. *eLife* **7**:e37344. doi:10.7554/eLife.37344

Jans J, Gladden JM, Ralston EJ, Pickle CS, Michel AH, Pferdehirt RR, Eisen MB, Meyer BJ. 2009. A condensin-like dosage compensation complex acts at a distance to control expression throughout the genome. *Genes Dev* **23**:602–618. doi:10.1101/gad.1751109

Kelly WG, Schaner CE, Dernburg AF, Lee M-H, Kim SK, Villeneuve AM, Reinke V. 2002. X-chromosome silencing in the germline of C. elegans. *Development* **129**:479–492.

Kruesi WS, Core LJ, Waters CT, Lis JT, Meyer BJ. 2013. Condensin controls recruitment of RNA polymerase II to achieve nematode X-chromosome dosage compensation. *eLife* **2**:e00808. doi:10.7554/eLife.00808

Langmead B, Salzberg SL. 2012. Fast gapped-read alignment with Bowtie 2. *Nature Methods* **9**:357–359. doi:10.1038/nmeth.1923

Lau AC, Nabeshima K, Csankovszki G. 2014. The C. elegans dosage compensation complex mediates interphase X chromosome compaction. *Epigenetics & Chromatin* **7**:31. doi:10.1186/1756-8935-7-31

Le TB, Laub MT. 2016. Transcription rate and transcript length drive formation of chromosomal interaction domain boundaries. *The EMBO Journal* **35**:1582–1595. doi:10.15252/embj.201593561

Li H, Handsaker B, Wysoker A, Fennell T, Ruan J, Homer N, Marth G, Abecasis G, Durbin R. 2009. The Sequence Alignment/Map format and SAMtools. *Bioinformatics* **25**:2078–2079. doi:10.1093/bioinformatics/btp352

Lin K, Hsin H, Libina N, Kenyon C. 2001. Regulation of the *Caenorhabditis elegans* longevity protein DAF-16 by insulin/IGF-1 and germline signaling. *Nature Genetics* **28**:139–145. doi:10.1038/88850

Lo T-W, Pickle CS, Lin S, Ralston EJ, Gurling M, Schartner CM, Bian Q, Doudna JA, Meyer BJ. 2013. Precise and Heritable Genome Editing in Evolutionarily Diverse Nematodes Using TALENs and CRISPR/Cas9 to Engineer Insertions and Deletions. *Genetics* **195**:331–348. doi:10.1534/genetics.113.155382

Lupiáñez DG, Kraft K, Heinrich V, Krawitz P, Brancati F, Klopocki E, Horn D, Kayserili H, Opitz JM, Laxova R, Santos-Simarro F, Gilbert-Dussardier B, Wittler L, Borschiwer M, Haas SA, Osterwalder M, Franke M, Timmermann B, Hecht J, Spielmann M, Visel A, Mundlos S. 2015. Disruptions of Topological Chromatin Domains Cause Pathogenic Rewiring of Gene-Enhancer Interactions. *Cell*. doi:10.1016/j.cell.2015.04.004

Martin M. 2011. Cutadapt removes adapter sequences from high-throughput sequencing reads. *EMBnet.journal* **17**:10–12. doi:10.14806/ej.17.1.200

Miller LM, Plenefisch JD, Casson LP, Meyer BJ. 1988. xol-1: A gene that controls the male modes of both sex determination and X chromosome dosage compensation in C. elegans. *Cell* **55**:167–183. doi:10.1016/0092-8674(88)90019-0

Nora EP, Goloborodko A, Valton A-L, Gibcus JH, Uebersohn A, Abdennur N, Dekker J, Mirny LA, Bruneau BG. 2017. Targeted Degradation of CTCF Decouples Local Insulation of Chromosome Domains from Genomic Compartmentalization. *Cell* **169**:930-944.e22. doi:10.1016/j.cell.2017.05.004

Oromendia AB, Amon A. 2014. Aneuploidy: implications for protein homeostasis and disease. *Disease Models & Mechanisms* **7**:15–20. doi:10.1242/dmm.013391

Paul MR, Markowitz TE, Hochwagen A, Ercan S. 2018. Condensin Depletion Causes Genome Decompaction Without Altering the Level of Global Gene Expression in Saccharomyces cerevisiae. *Genetics* genetics.301217.2018. doi:10.1534/genetics.118.301217

Pferdehirt RR, Kruesi WS, Meyer BJ. 2011. An MLL/COMPASS subunit functions in the C. elegans dosage compensation complex to target X chromosomes for transcriptional regulation of gene expression. *Genes Dev* **25**:499–515. doi:10.1101/gad.2016011

Podshivalova K, Kerr RA, Kenyon C. 2017. How a Mutation that Slows Aging Can Also Disproportionately Extend End-of-Life Decrepitude. *Cell Reports* **19**:441–450. doi:10.1016/j.celrep.2017.03.062

Ramírez F, Ryan DP, Grüning B, Bhardwaj V, Kilpert F, Richter AS, Heyne S, Dündar F, Manke T. 2016. deepTools2: a next generation web server for deep-sequencing data analysis. *Nucleic Acids Res* **44**:W160–W165. doi:10.1093/nar/gkw257

Rao SSP, Huang S-C, Hilaire BGS, Engreitz JM, Perez EM, Kieffer-Kwon K-R, Sanborn AL, Johnstone SE, Bascom GD, Bochkov ID, Huang X, Shamim MS, Shin J, Turner D, Ye Z, Omer AD, Robinson JT, Schlick T, Bernstein BE, Casellas R, Lander ES, Aiden EL. 2017.

Cohesin Loss Eliminates All Loop Domains. *Cell* **171**:305-320.e24. doi:10.1016/j.cell.2017.09.026

Schwarzer W, Abdennur N, Goloborodko A, Pekowska A, Fudenberg G, Loe-Mie Y, Fonseca NA, Huber W, Haering CH, Mirny L, Spitz F. 2017. Two independent modes of chromatin organization revealed by cohesin removal. *Nature* **551**:51–56. doi:10.1038/nature24281

Spieth J, Lawson D, Davis P, Gary W, Kevin H. 2014. Overview of gene structure in C. elegans. *WormBook* 1–18. doi:10.1895/wormbook.1.65.2

Thorpe CJ, Schlesinger A, Carter JC, Bowerman B. 1997. Wnt Signaling Polarizes an Early C. elegans Blastomere to Distinguish Endoderm from Mesoderm. *Cell* **90**:695–705. doi:10.1016/S0092-8674(00)80530-9

Trapnell C, Roberts A, Goff L, Pertea G, Kim D, Kelley DR, Pimentel H, Salzberg SL, Rinn JL, Pachter L. 2012. Differential gene and transcript expression analysis of RNA-seq experiments with TopHat and Cufflinks. *Nature Protocols* **7**:562–578. doi:10.1038/nprot.2012.016

Tzur YB, Winter E, Gao J, Hashimshony T, Yanai I, Colaiácovo MP. 2018. Spatiotemporal Gene Expression Analysis of the Caenorhabditis elegans Germline Uncovers a Syncytial Expression Switch. *Genetics* **210**:587–605. doi:10.1534/genetics.118.301315

Valton A-L, Dekker J. 2016. TAD disruption as oncogenic driver. *Current Opinion in Genetics & Development*, Cancer genomics **36**:34–40. doi:10.1016/j.gde.2016.03.008

Wang X, Brandão HB, Le TBK, Laub MT, Rudner DZ. 2017. Bacillus subtilis SMC complexes juxtapose chromosome arms as they travel from origin to terminus. *Science* **355**:524–527. doi:10.1126/science.aai8982

Wheeler BS, Anderson E, Frøkjær-Jensen C, Bian Q, Jorgensen E, Meyer BJ. 2016. Chromosome-wide mechanisms to decouple gene expression from gene dose during sex-chromosome evolution. *eLife* **5**:e17365. doi:10.7554/eLife.17365

Yonker SA, Meyer BJ. 2003. Recruitment of C. elegans dosage compensation proteins for gene-specific versus chromosome-wide repression. *Development* **130**:6519–6532. doi:10.1242/dev.00886

Zhang Y, Liu T, Meyer CA, Eeckhoute J, Johnson DS, Bernstein BE, Nusbaum C, Myers RM, Brown M, Li W, Liu XS. 2008. Model-based Analysis of ChIP-Seq (MACS). *Genome Biology* **9**:R137. doi:10.1186/gb-2008-9-9-r137

Figure legends

Figure 1 A *rex* site is necessary for formation of each DCC-dependent TAD boundary

A) Diagram showing locations of the eight *rex* sites at DCC-dependent boundaries, which are deleted in *8rexΔ*. A subset of the sites is deleted in *3rexΔ* and *6rexΔ*.

B, C, and D) X chromosome heatmaps show wild-type Hi-C Z scores subtracted from *rex-47Δ*, *3rexΔ*, and *6rexΔ* Z scores. Red indicates higher interactions in mutant. Blue indicates higher interactions in wild type. Black arrows show the position of deleted *rex* sites. The orange around each arrow indicates an increase in interactions around the deleted *rex* site, reflecting TAD boundary loss. Lower plots show insulation scores across the X chromosome for the *rex* deletion mutant, wild type, and their difference. Blue ticks mark the position of deleted *rex* sites and orange ticks mark DCC-dependent boundaries that remain in the mutant.

E, F, and G) X chromosome heatmaps show Hi-C interactions in *8rexΔ*, DCC mutant (*sdc-2(y93, RNAi)*), and wild-type embryos. Arrows mark the positions of DCC-dependent boundaries in wild type, which are lost in *8rexΔ* and DCC mutant.

H and I) Heatmaps compare *8rexΔ* and DCC mutant to wild-type Hi-C Z scores and lower plots show X chromosome insulation profiles. Black arrows and blue ticks mark the locations of DCC-dependent boundaries, which are lost in *8rexΔ* and DCC mutant.

J) 3D plots show the average Z scores for interactions among the 22 non-boundary *rex* sites with the highest SDC-3 binding. Interactions between sites within 4 Mb of each other are included.

Figure 1—figure supplement 1 DCC binding is lost at deleted *rex* sites

A) X chromosome SDC-3 and DPY-27 ChIP-seq profiles on X chromosomes for wild-type and *8rexΔ* embryos. Plots are scaled based on the binding at four strong *rex* sites that were not deleted (*rex-40*, *rex-23*, *rex-16*, and *Prex-30*). Blue stripes highlight the locations of the eight deleted *rex* sites.

Figure 1—figure supplement 2 Effect of *rex* deletions on chromosome structure is specific to X

A-E) Chromosome I heatmaps show wild-type Hi-C Z scores subtracted from *rex-47Δ*, *3rexΔ*, *6rexΔ*, *8rexΔ*, and *sdc-2(y93, RNAi)* Z scores. Red indicates higher interactions in mutant. Blue indicates higher interactions in wild type. Lower plots show insulation scores across I for the *rex* deletion mutant, wild type, and their difference.

F and G) Cumulative frequency of interaction Z scores for *rex-rex* interactions within the same TAD or across TAD boundaries in wild type, *8rexΔ*, and DCC mutant. The 22 non-boundary *rex* sites with the highest SDC-3 binding are included and interactions between sites within 4 Mb are included.

Figure 2 A *rex* site is sufficient to create a TAD boundary at a new location on X

A) Diagram showing locations on X of eight *rex* deletions and two *rex* sites inserted at new locations

B and D) Heatmaps show X chromosome Hi-C interactions with *rex-32* and *rex-8* insertions. Arrows mark the locations of inserted *rex* sites.

C and E) Z score subtraction heatmaps show increased (red) and decreased (blue) interactions in *8rexΔ* plus *rex-32* and *8rexΔ* plus *rex-32*, *rex-8* compared to *8rexΔ*. Arrows mark the locations of inserted *rex* sites.
F) Plot comparing X chromosome insulation scores in *8rexΔ* to *8rexΔ* with one or two inserted *rex* sites
G) Diagram shows the location of *rex-32* inserted on the wild-type X chromosome. Heatmap shows the difference between *rex-32* insertion and wild type Z scores. An arrow marks the location of the *rex-32* insertion.
H) Boundaries adjacent to deleted boundaries become stronger (p=0.02, paired T test), while boundaries two away from deleted boundaries were unchanged (p=0.60). Using Hi-C data from *rex-47Δ*, *3rexΔ*, *6rexΔ*, and *8rexΔ*, we calculated the average insulation profile around all boundaries adjacent to a deleted boundary and compared it to the average insulation at the same boundaries in the strain with fewer deletions (e.g. the boundary upstream of *rex-14* was stronger in *3rexΔ* compared to *rex-47Δ*). Two replicates for each of 12 boundaries were included for 24 total comparisons. The insulation scores at the boundaries were used to calculate a p value with a paired T test. Similar analysis was performed for the seven boundaries that are two boundaries away from deleted boundaries for 14 total comparisons.

Figure 2—figure supplement 1 Not all strong *rex* sites establish TAD boundaries.
A) X chromosome wild-type insulation profile and insulation difference between wild type and DCC mutant. Insulation was calculated by summing interactions in a 250-kb sliding window (unlike other figures which used a 500-kb window). *rex* sites were ranked based on number of SDC-3 ChIP-seq reads in the 400-bp surrounding the summit of the peak. All DCC-dependent boundaries (solid purple lines) contain one of the 13 highest occupancy *rex* sites. Five non-boundary *rex* sites have as much DCC binding as sites that establish boundaries (dotted purple lines) and show insulation changes. Insulation changes also occur at some *rex* sites of rank 14-30 (dotted orange lines).
B) Correlation between DCC binding and insulation change. For each of the strongest 30 *rex* sites, the insulation difference between DCC mutant and wild type is plotted against the amount of SDC-3 binding. *rex* sites at DCC-dependent boundaries are colored red. There are five *rex* sites with more binding than *rex-47* that do not create boundaries (*rex-23*, *rex-16*, *rex-40*, *Prex-30*, and *rex-45*).

Figure 2—figure supplement 2 *rex* sites inserted on chromosome I weakly recruit the DCC and do not create TAD boundaries
A) SDC-3 binding at *rex-32* and *rex-8* inserted at new locations on X is similar to binding at the endogenous sites. We normalized the binding at *rex-32* and *rex-8* to the average binding at four strong non-boundary *rex* sites within the same dataset (*rex-40*, *rex-23*, *rex-16*, and *Prex-30*). Binding was calculated by summing ChIP-seq reads mapping within 200 bp of the summit.
B) SDC-3 binding at *rex-32* inserted at 15.5 Mb on the wild-type X chromosome is equivalent to binding at the endogenous *rex-32* as measured by ChIP-qPCR. Binding is normalized to

the binding at five strong *rex* sites (*rex-32*, *rex-8*, *rex-16*, *rex-48*, and *rex-35*). Error bars show standard deviation of three biological replicates.

C) SDC-3 binding at three *rex* sites inserted on chromosome I is lower than binding at the endogenous sites on X. Binding was calculated and normalized as in A.

D-F) Chromosome I heatmaps shows wild-type Hi-C Z scores subtracted from Z scores in strains with one, two, or three *rex* sites inserted on chromosome I. *3rexΔ* is used as the wild-type reference. Arrows mark positions of inserted *rex* sites. Lower plots show the insulation in the presence and absence of the *rex* sites inserted on chromosome I and their difference. Blue ticks mark the locations of the *rex* insertions.

Figure 2—figure supplement 3 Removing TAD boundaries affects the strength of neighboring and distant boundaries

A) X chromosome insulation profiles comparing *6rexΔ* and *8rexΔ*. Blue ticks mark *rex* sites deleted in both mutants and red ticks mark *rex* sites deleted only in *8rexΔ*. Boundaries adjacent to the boundaries deleted only in *8rexΔ* are strengthened (arrows).

B) X chromosome insulation profiles comparing *3rexΔ* and *6rexΔ*. Blue ticks mark *rex* sites deleted in both mutants and red ticks mark *rex* sites deleted only in *6rexΔ*. Insulation changes at boundaries far from the deleted boundaries (arrows).

Figure 3 DCC binding at strong *rex* sites induces DCC binding nearby

A and B) SDC-3 and DPY-27 ChIP-seq in the 80-kb region surrounding *rex-48* in wild type and the *rex-48* deletion in *8rexΔ*. Reads were normalized using RPKM. Red ticks mark the location of the 408-bp deletion. Bottom plots display the $\log_2$ ratio of ChIP-seq reads in *8rexΔ* compared to wild type with each point showing the ratio in a 1-kb window (ratios were not calculated for the deleted region). Gray dashed lines show the median ratio for the X chromosome.

C and D) SDC-3 and DPY-27 ChIP-seq in the 80-kb region surrounding the location of the inserted *rex-32* in *8rexΔ* and *8rexΔ* plus *rex-32*,*rex-8*. Red ticks mark the location of the 592-bp insertion. As in A and B, bottom plots show the $\log_2$ ratio of DCC binding.

Figure 3—figure supplement 1 DCC binding at strong *rex* sites induces DCC binding nearby

A-G) SDC-3 ChIP-seq in the 80-kb region surrounding boundary *rex* sites in wild type and the deletions in *8rexΔ*. Reads were normalized using RPKM. Red ticks mark the locations of the deletions. Bottom plots display the $\log_2$ ratio of ChIP-seq reads in *8rexΔ* compared to wild type with each point showing the ratio in a 1-kb window (ratios were not calculated for the deleted region). Gray dashed lines show the median ratio for the X chromosome.

H) SDC-3 ChIP-seq in the 80-kb region surrounding the location of the inserted *rex-8* in *8rexΔ* and *8rexΔ* plus *rex-32*,*rex-8*. Red ticks mark the location of the 796-bp insertion. As above, bottom plots show the $\log_2$ ratio of DCC binding.

Figure 4 Expression of X-linked genes is unaffected by loss of TAD boundaries

A and B) Box plots show gene expression changes by chromosome in *8rexΔ* and *sdc-2(y93, RNAi)* compared to wild-type embryos. Five *8rexΔ* and three DCC mutant replicates were used. Numbers of genes included per chromosome are listed.

C) Median gene expression changes in DCC mutant or *8rexΔ* compared to wild type in a 400-kb sliding window on X. Blue vertical lines mark the location of *rex* sites deleted in *8rexΔ*.

Figure 4—figure supplement 1

A) Average expression of all the genes on each chromosome at each time point during embryogenesis using RNA-seq data from (Hashimshony et al., 2015)

B) Comparison of gene expression by chromosome in younger wild-type embryos to older wild-type embryos. Two replicates are included for each age. Because X chromosome silencing is gradually lost during early development, genes on X have lower expression in the younger population.

C) The average time for developed from comma stage to two-fold stage and hatching is equivalent for wild-type and *8rexΔ* embryos. Error bars show standard deviation.

D) Expression of genes that changes in expression during development. Using data from (Hashimshony et al., 2015), we selected genes that have >1 transcripts per million at some point during embryogenesis and change in expression at least 20-fold during embryogenesis. We scaled the expression of each gene by subtracting the mean and dividing by the standard deviation and k-means clustered them into five clusters.

Figure 5 The DCC promotes interactions between loci within 1 Mb

A and B) Heatmaps show *sdc-2(y93, RNAi)* minus *8rexΔ* Z scores for chromosomes X and I. Blue indicates a loss of interactions in DCC mutant, and arrows mark the locations of DCC-dependent TAD boundaries (which are absent in both mutants). Lower plots show the change in insulation in *8rexΔ* and DCC mutant compared to wild type with black ticks marking DCC-dependent boundaries on X.

C, D, and E) Scaling plots show the average interactions between loci at increasing distances on X and autosomes in wild type, *8rexΔ*, and DCC mutant.

F) Cumulative distributions of Z score differences between DCC mutant and *8rexΔ* for interactions at different distances. Interactions below 1 Mb are less frequent in DCC mutant than in *8rexΔ* on X but not autosomes.

G) Boxplots show the fraction of total chromatin (measured by DAPI staining) occupied by the X chromosome (measured by DPY-27 immunofluorescence) for n intestine nuclei of wild-type, *8rexΔ*, and *dpy-21(null)* adults.

Figure 5—figure supplement 1 The DCC mediates interactions at the 100 kb – 1 Mb scale on X.

A-C) Scaling plots show the average interactions between loci at increasing distances on X and autosomes in wild type, *8rexΔ*, and DCC mutant.

Figure 6 *8rexΔ* worms have reduced thermotolerance, shortened lifespan, and accelerated aging

A) Percent of wild-type and *8rexΔ* Day 1 adult worms surviving after 7 hours at 37°C in each of nine trials. Fifty worms of each genotype were counted.

B) Lifespan of wild-type and *8rexΔ* worms grown on plates with and without 20 ng/µl tunicamycin. For B-E, values from replicate experiments are presented in Supplementary Table 2.
C) Survival of wild-type and *8rexΔ* worms in 0.2 M paraquat. Wild-type worms grown on *daf-2* RNAi were used as a control with increased oxidative stress tolerance.
D) Lifespan of wild-type compared to *8rexΔ* ($p < 0.0001$, logrank test) and *rex-32Δ rex-33Δ* ($p < 0.0001$) hermaphrodite worms
E) Lifespan of male wild-type and *8rexΔ* worms ($p=0.25$, logrank test)
F) Average unstimulated speed of wild-type and *8rexΔ* worms during aging. For each genotype, the speed of worms on eight plates was measured throughout adulthood. The measurement included only moving worms (not those that had stopped moving or died). We calculated the mean speed of worms of each plate and plotted the mean and standard error of the mean of the eight plates. Asterisks indicate significant differences ($p<0.05$, t test).
G and H) Maximum speed and reversal distance in response to a stimulus for wild-type and *8rexΔ* worms during aging. A physical stimulus was delivered by tapping the worm plate and the worms' maximum speed and reversal distance in response to the stimulus were measured. Mean and standard error of the mean are plotted as in F.

Figure 6—figure supplement 1
A) Lifespan of wild-type compared to *rex-32Δ* ($p=0.06$, logrank test), *rex-33Δ* ($p=0.03$), and *rex-32Δ rex-33Δ* ($p<0.0001$). For A-C, values from replicate experiments are presented in Supplementary Table 2.
B) Lifespan of wild-type compared to *6rexΔ* ($p<0.0001$)
C) Lifespan of wild-type compared to *8rexΔ* ($p<0.0001$) and *8rexΔ+rex-32,rex-8* ($p<0.0001$)
D) Maximum unstimulated speed of wild-type and *8rexΔ* worms during aging. For each genotype, the speed of worms on eight plates was measured throughout adulthood. The measurement included only moving worms (not those that had stopped moving or died). We calculated the maximum speed of worms of each plate and plotted the mean and standard error of the mean of the eight plates. Asterisks indicate significant differences ($p<0.05$, t test).
E) Average speed wild-type and *8rexΔ* worms move in response to a mechanical stimulus during aging. The mean and standard error of the means of eight plates are plotted as in D.
F) Body length of wild-type and *8rexΔ* worms during aging. The mean and standard error of the means of eight plates are plotted as in D.

Figure 7 Model for DCC-dependent TAD formation by the DCC
DCC condensin (blue) loads onto chromatin and extrudes a loop of increasing size until it is halted by SDC proteins bound at a strong *rex* site (pink). Because the DCC-mediated loops do not cross strong *rex* sites, the *rex* sites define the location of TAD boundaries. When the strong *rex* sites are deleted (orange), TAD boundaries are lost, but other DCC-mediated interactions remain.

Supplementary Table 1

	Total embryos	Total adults	Viability	Average Brood Size
WT	2572	2593	1.008165	257
8rexΔ	2256	2310	1.023936	251

Viability and brood size of wild-type and *8rexΔ* worms

Supplementary Table 2

Genotype	Median Lifespan	N (total)	p value compared to WT	p value compared to *8rexΔ*
Trial 1				
WT	20	77 (108)		
8rexΔ	16	90 (120)	< 0.0001	
Trial 2				
WT	22	89 (120)		
8rexΔ	18	102 (120)	< 0.0001	
rex-32Δ rex-33Δ	18	88 (120)	< 0.0001	
rex-32Δ	20	98 (120)	0.055	0.0226
rex-33Δ	20	100 (120)	0.0304	0.0196
8rexΔ plus rex-32 & rex-8	18	103 (120)	< 0.0001	0.2218
Trial 3				
WT	20	78 (120)		
8rexΔ	16	100 (120)	< 0.0001	
6rexΔ	20	92 (120)	0.7959	< 0.0001
rex-32Δ rex-33Δ	16	109 (120)	< 0.0001	0.0632
Trial 4				
WT	18	92 (120)		
6rexΔ	18	88 (120)	0.1974	
rex-32Δ	17	78 (120)	0.189	
rex-33Δ	18	93 (120)	0.5062	
males				
WT males	15	120 (270)		
8rexΔ males	15	90 (300)	0.2546	
Tunicamycin Trail 1				
WT	19	96 (120)		
8rexΔ	17	94 (108)	0.0004	
WT tunicamycin	13	98 (120)	< 0.0001	< 0.0001
8rexΔ tunicamycin	12	102 (120)	< 0.0001	< 0.0001

Tunicamycin Trail 2

WT	24	92 (120)		
8rexΔ	20	84 (120)	< 0.0001	
WT tunicamycin	19	110 (120)	< 0.0001	0.3192
8rexΔ tunicamycin	19	105 (120)	< 0.0001	< 0.0001

Statistics for each lifespan experiment. N is the number of worm deaths counted (out of the total worms scored including those censored). P values were calculated using the logrank test.

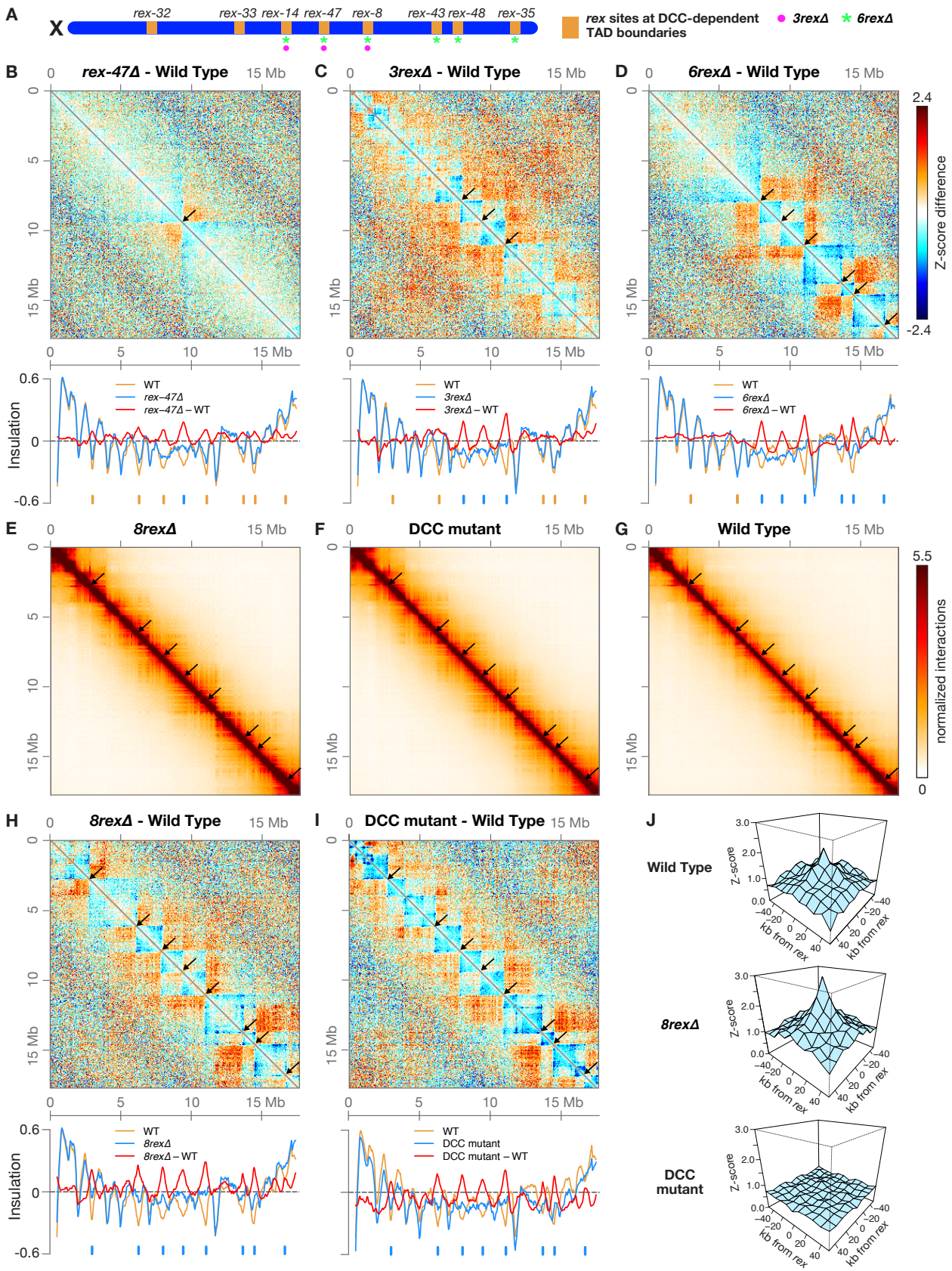
A
X
rex-32
rex-33
rex-14
rex-47
rex-8
rex-43
rex-48
rex-35
rex sites at DCC-dependent TAD boundaries
3rexΔ
6rexΔ
B
rex-47Δ - Wild Type
C
3rexΔ - Wild Type
D
6rexΔ - Wild Type
0
5
10
15 Mb
2.4
-2.4
Z-score difference
Insulation
0.6
-0.6
WT
rex–47Δ
rex–47Δ – WT
3rexΔ
3rexΔ – WT
6rexΔ
6rexΔ – WT
E
8rexΔ
F
DCC mutant
G
Wild Type
5.5
normalized interactions
H
8rexΔ - Wild Type
I
DCC mutant - Wild Type
8rexΔ – WT
DCC mutant
DCC mutant – WT
J
Wild Type
8rexΔ
DCC mutant
Z-score
kb from rex

Figure 1, Supplement 1

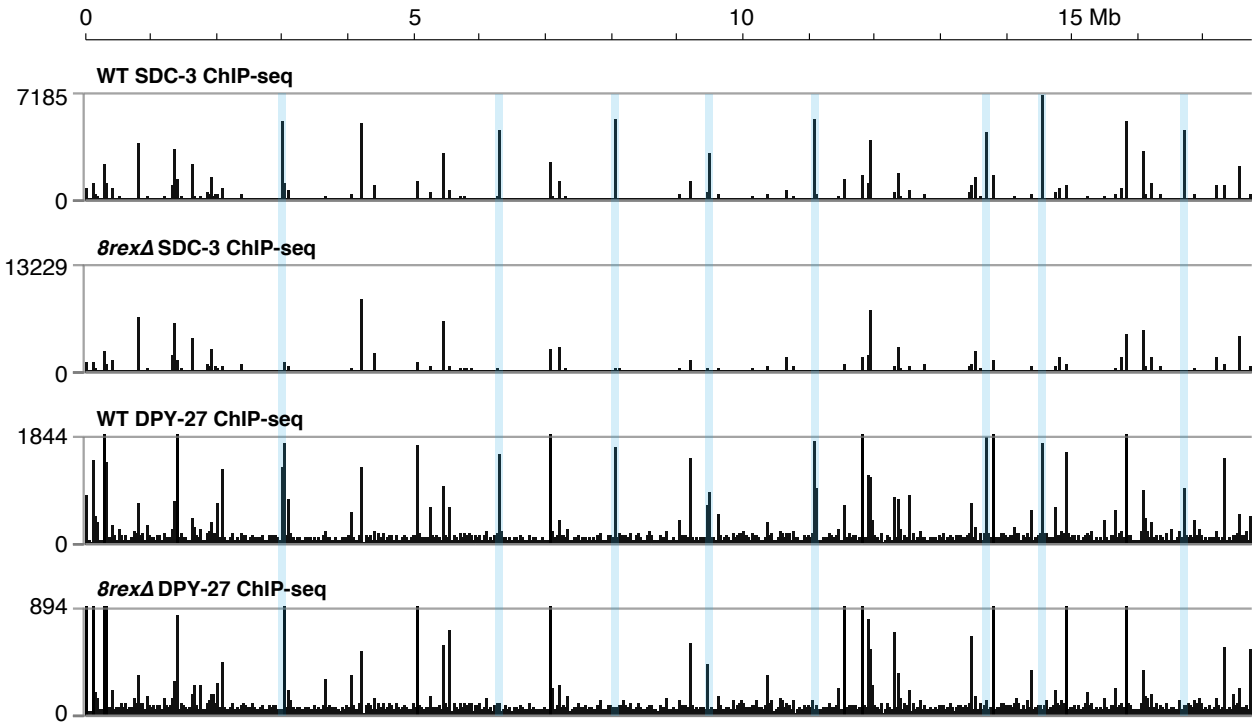

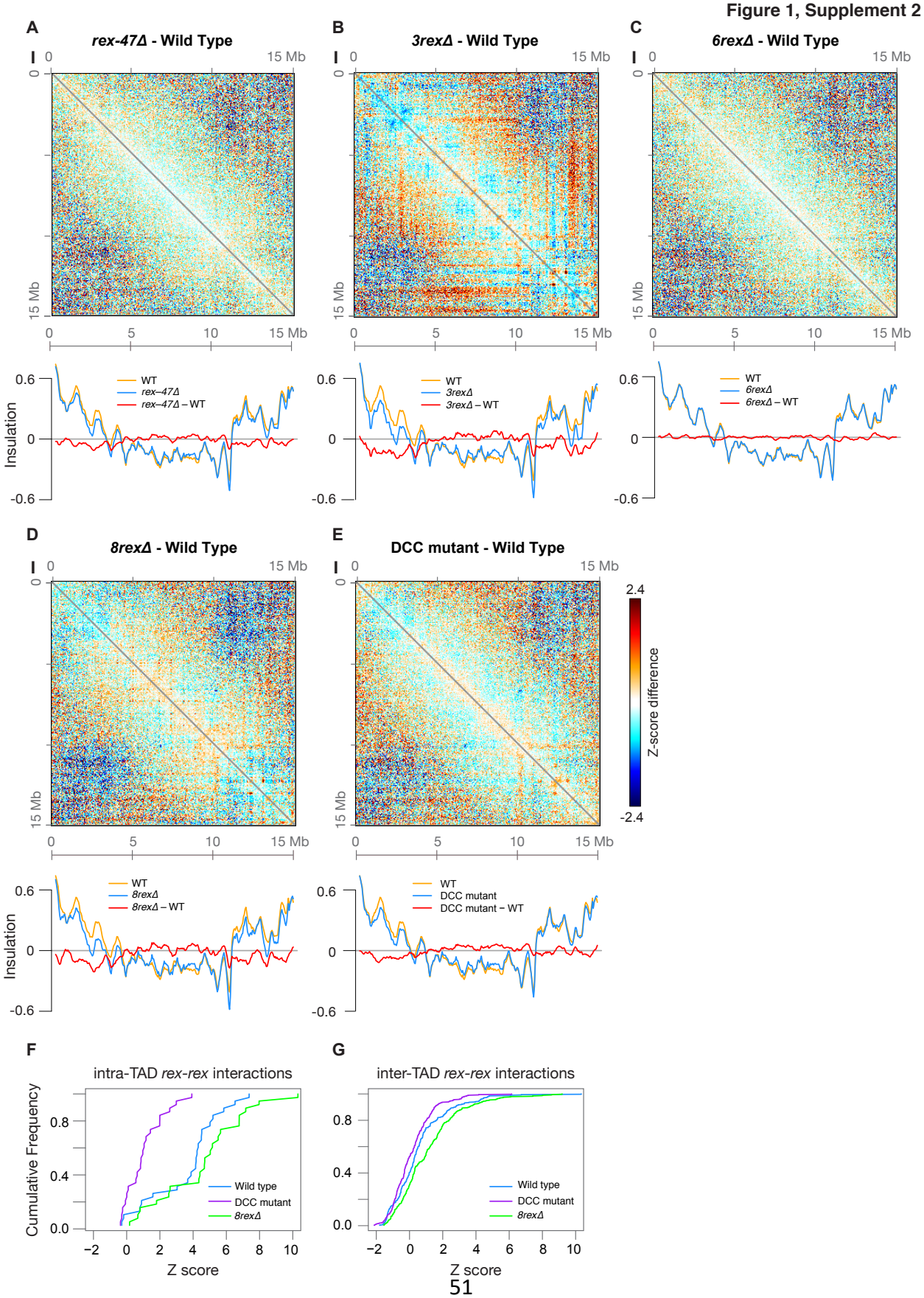
A
rex-47Δ - Wild Type
B
3rexΔ - Wild Type
C
6rexΔ - Wild Type
D
8rexΔ - Wild Type
E
DCC mutant - Wild Type
0
15 Mb
5
10
Insulation
0.6
-0.6
WT
rex–47Δ
rex–47Δ – WT
3rexΔ
3rexΔ – WT
6rexΔ
6rexΔ – WT
8rexΔ
8rexΔ – WT
DCC mutant
DCC mutant – WT
2.4
-2.4
Z-score difference
F
intra-TAD rex-rex interactions
G
inter-TAD rex-rex interactions
Cumulative Frequency
0.0
0.4
0.8
Wild type
DCC mutant
8rexΔ
−2
2
4
6
8
10
Z score

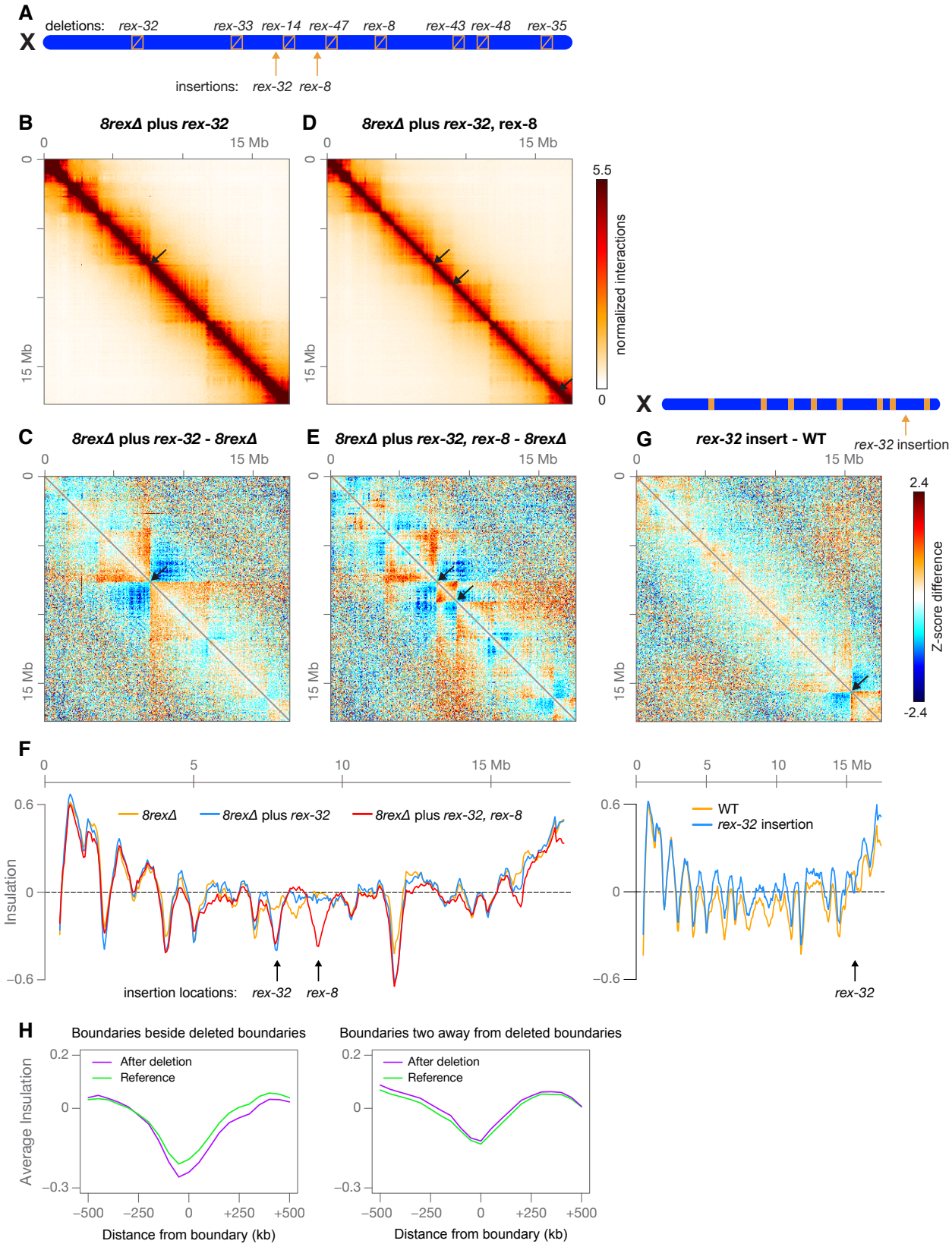
A
X
deletions: rex-32 rex-33 rex-14 rex-47 rex-8 rex-43 rex-48 rex-35
insertions: rex-32 rex-8
B
8rexΔ plus rex-32
D
8rexΔ plus rex-32, rex-8
0
15 Mb
5.5
normalized interactions
C
8rexΔ plus rex-32 - 8rexΔ
E
8rexΔ plus rex-32, rex-8 - 8rexΔ
G
rex-32 insert - WT
rex-32 insertion
2.4
Z-score difference
-2.4
F
Insulation
8rexΔ
8rexΔ plus rex-32
8rexΔ plus rex-32, rex-8
insertion locations: rex-32 rex-8
WT
rex-32 insertion
H
Boundaries beside deleted boundaries
Boundaries two away from deleted boundaries
Average Insulation
After deletion
Reference
Distance from boundary (kb)

Figure 2, Supplement 1

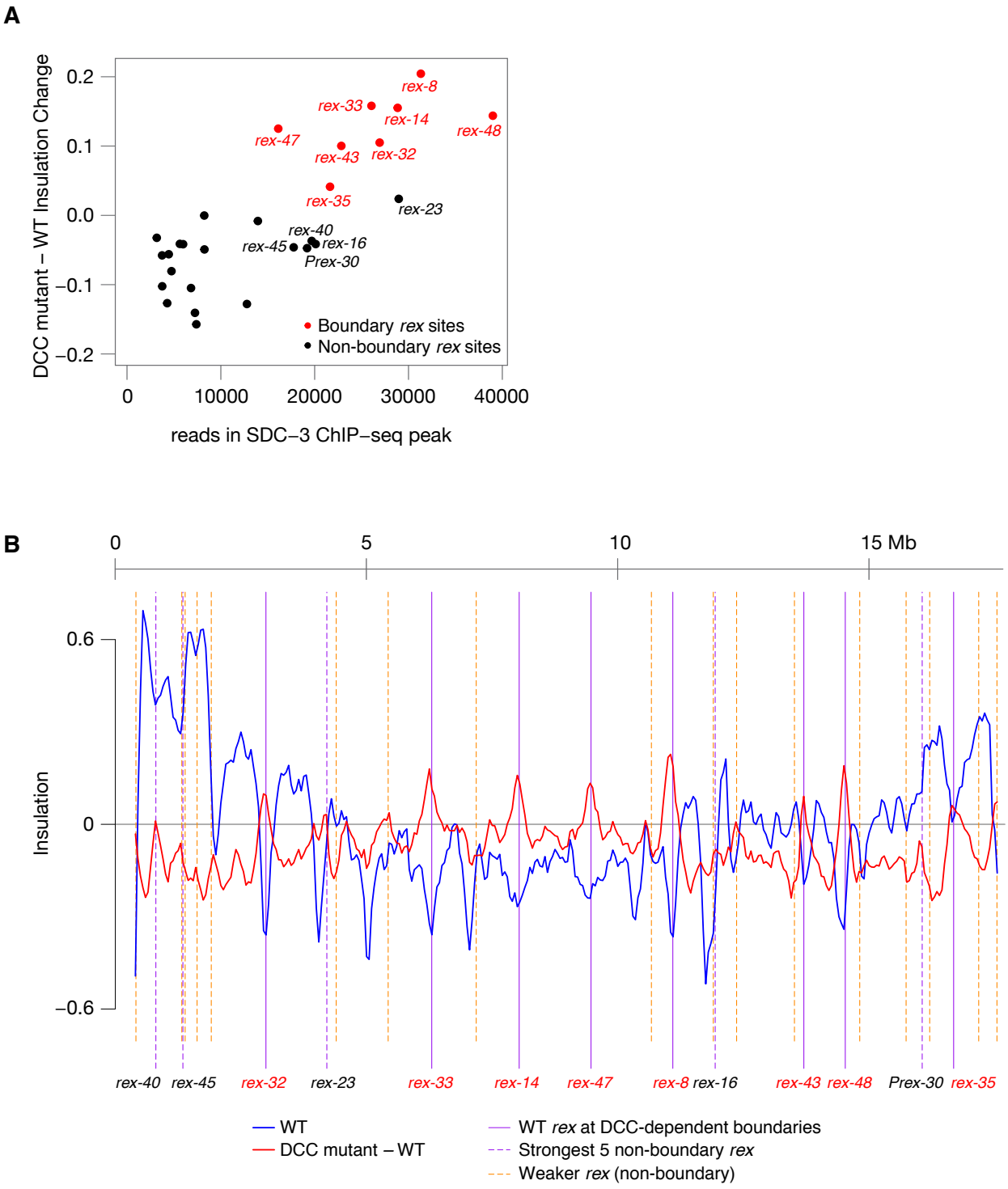

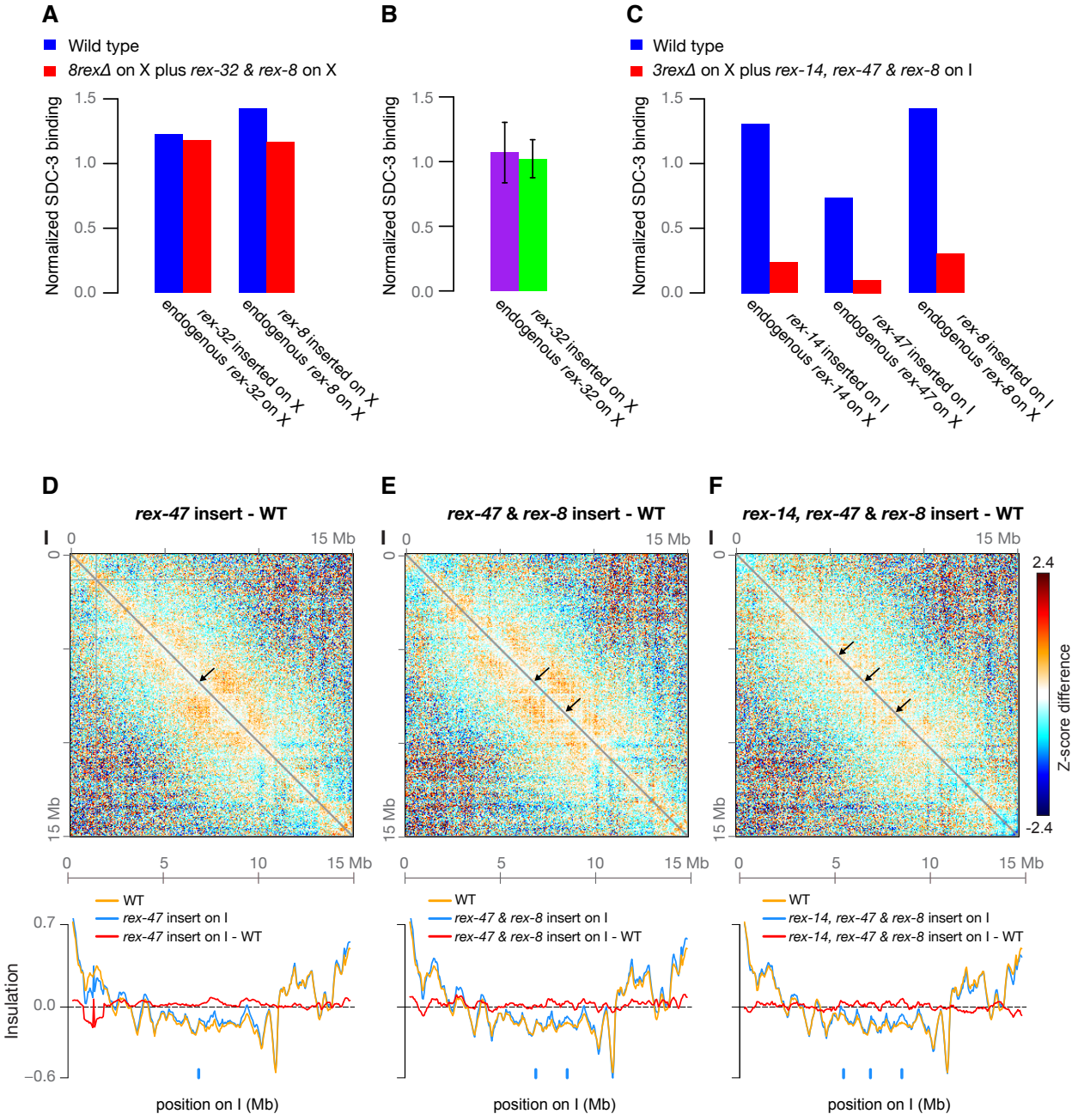
A
Wild type
8rexΔ on X plus rex-32 & rex-8 on X
Normalized SDC-3 binding
1.5
1.0
0.5
0.0
endogenous rex-32 on X
rex-32 inserted on X
endogenous rex-8 on X
rex-8 inserted on X
B
Wild type
8rexΔ on X plus rex-32 & rex-8 on X
Normalized SDC-3 binding
endogenous rex-32 on X
rex-32 inserted on X
C
Wild type
3rexΔ on X plus rex-14, rex-47 & rex-8 on I
Normalized SDC-3 binding
endogenous rex-14 on X
rex-14 inserted on I
endogenous rex-47 on X
rex-47 inserted on I
endogenous rex-8 on X
rex-8 inserted on I
D
rex-47 insert - WT
E
rex-47 & rex-8 insert - WT
F
rex-14, rex-47 & rex-8 insert - WT
I
0
15 Mb
2.4
-2.4
Z-score difference
0
5
10
15 Mb
WT
rex-47 insert on I
rex-47 insert on I - WT
rex-47 & rex-8 insert on I
rex-47 & rex-8 insert on I - WT
rex-14, rex-47 & rex-8 insert on I
rex-14, rex-47 & rex-8 insert on I - WT
Insulation
0.7
0.0
−0.6
position on I (Mb)

Figure 2, Supplement 3

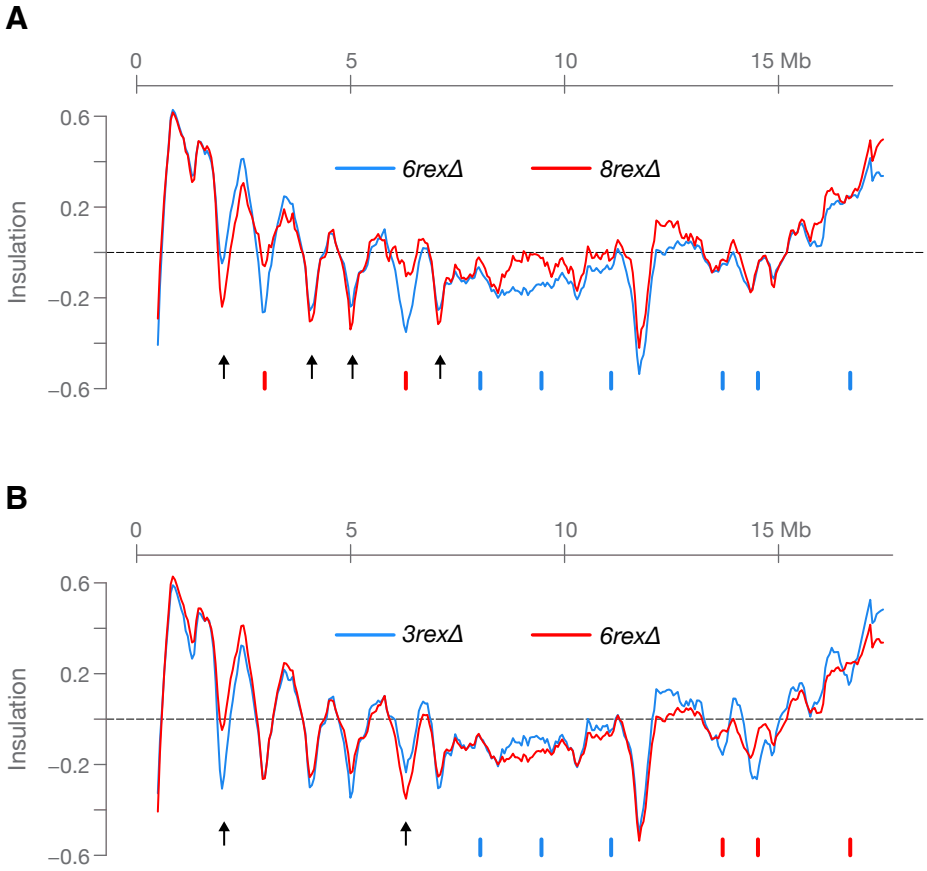

Figure 3

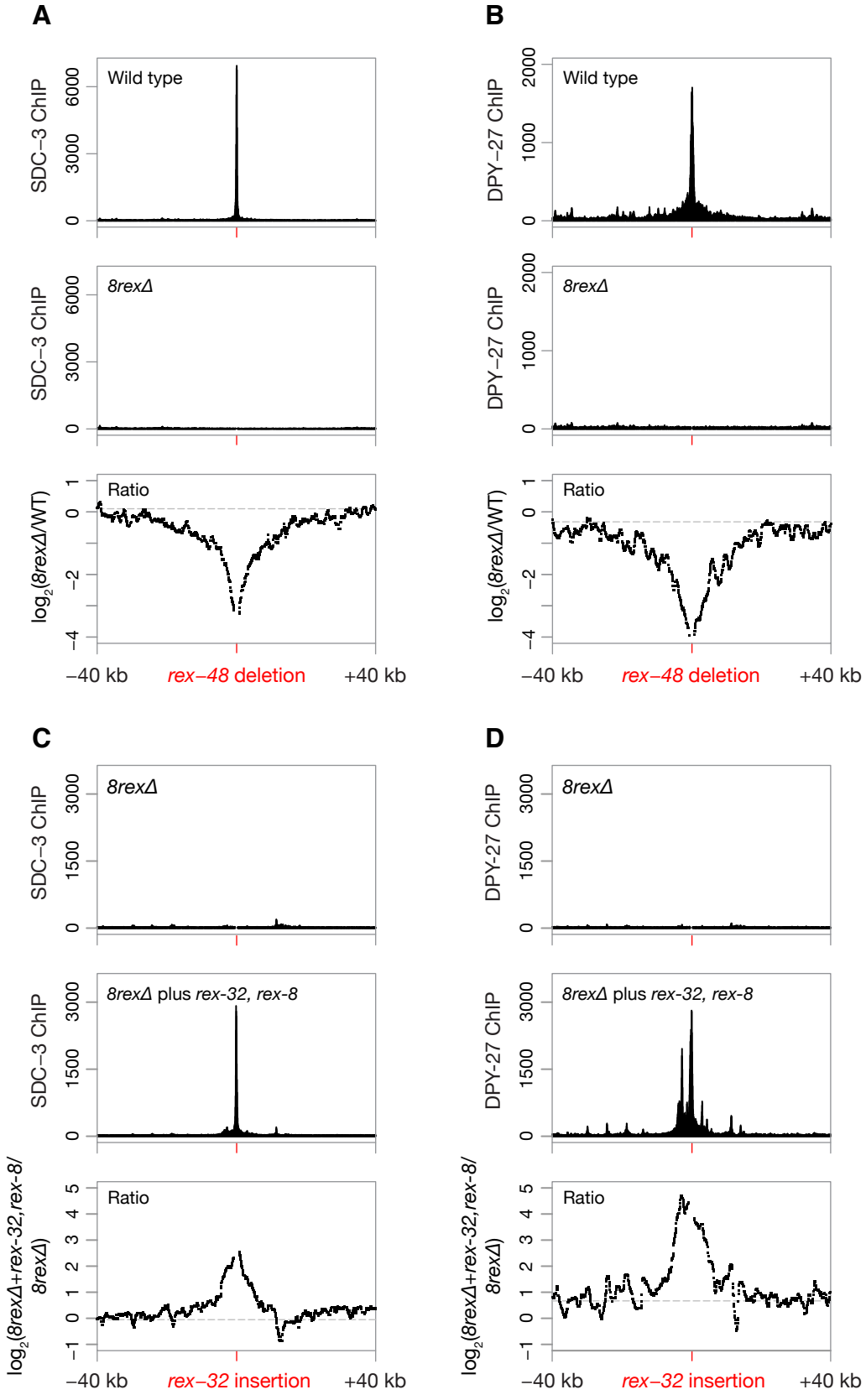
A
B
C
D
SDC–3 ChIP
DPY–27 ChIP
DPY-27 ChIP
Wild type
8rexΔ
8rexΔ plus rex-32, rex-8
Ratio
log2(8rexΔ/WT)
log2(8rexΔ+rex-32,rex-8/ 8rexΔ)
–40 kb
rex–48 deletion
rex–32 insertion
+40 kb

Figure 3, Supplement 1

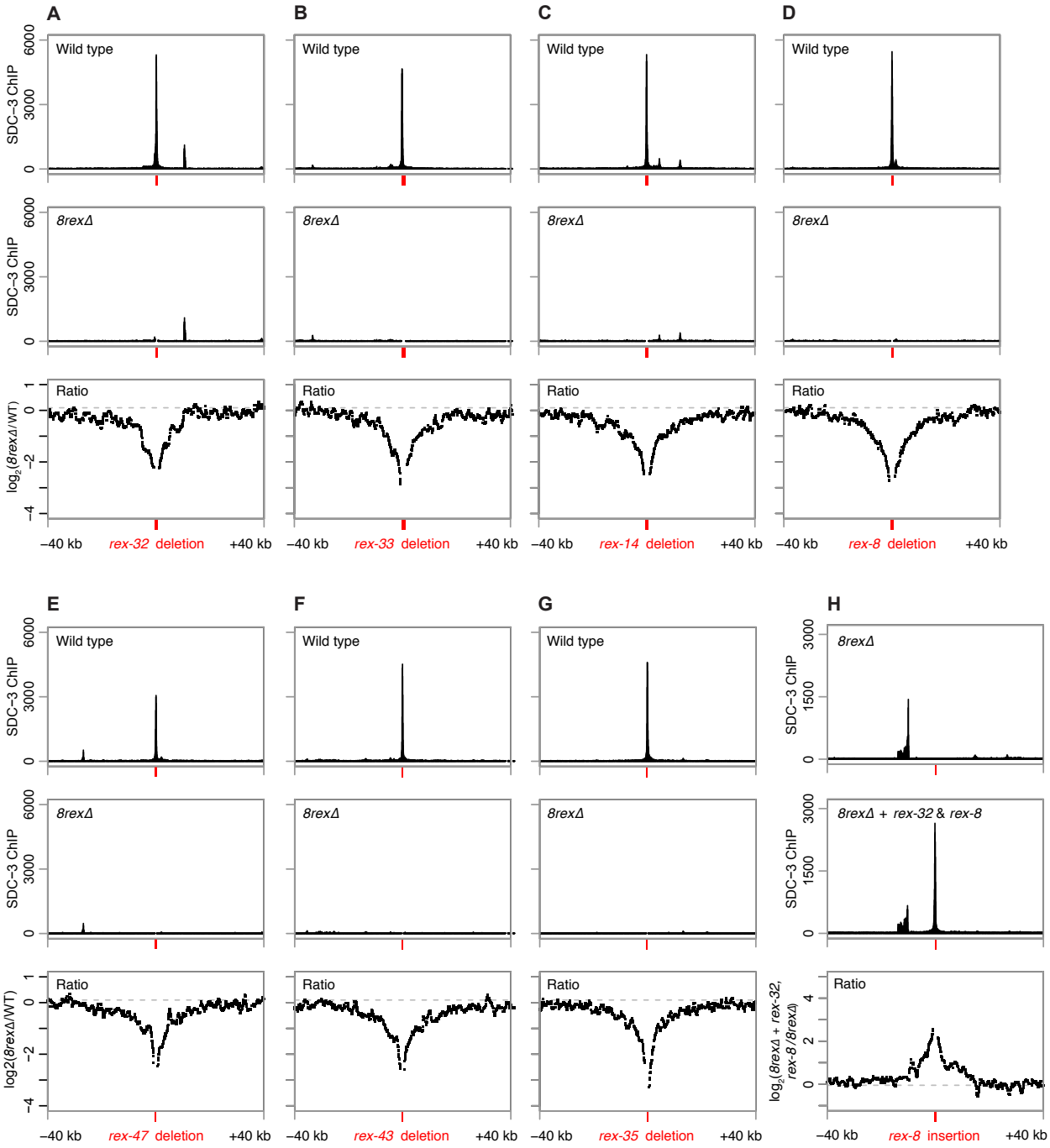

Figure 4

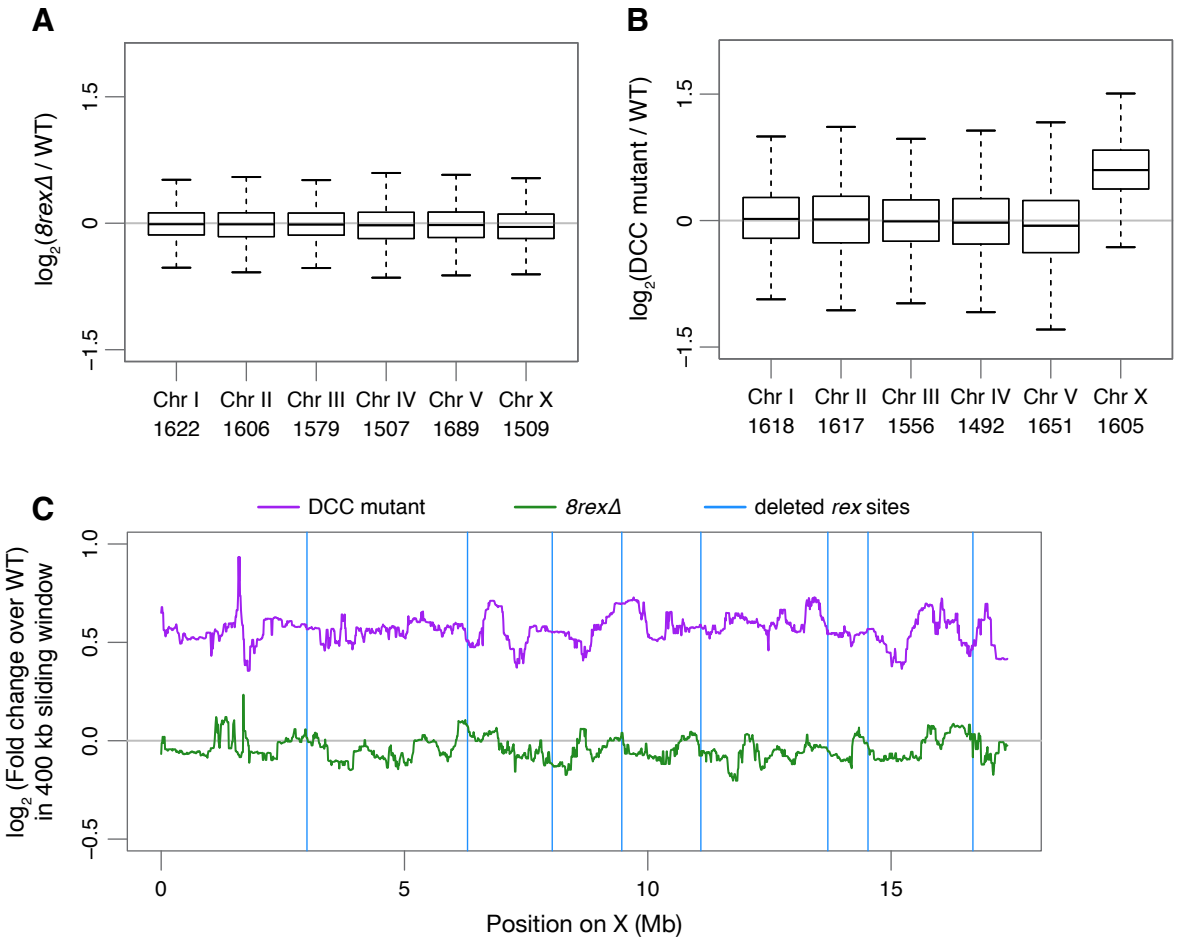
A
log2(8rexΔ / WT)
1.5
0
−1.5
Chr I 1622
Chr II 1606
Chr III 1579
Chr IV 1507
Chr V 1689
Chr X 1509
B
log2(DCC mutant / WT)
1.5
0
−1.5
Chr I 1618
Chr II 1617
Chr III 1556
Chr IV 1492
Chr V 1651
Chr X 1605
C
DCC mutant
8rexΔ
deleted rex sites
log2 (Fold change over WT) in 400 kb sliding window
1.0
0.5
0.0
−0.5
0
5
10
15
Position on X (Mb)

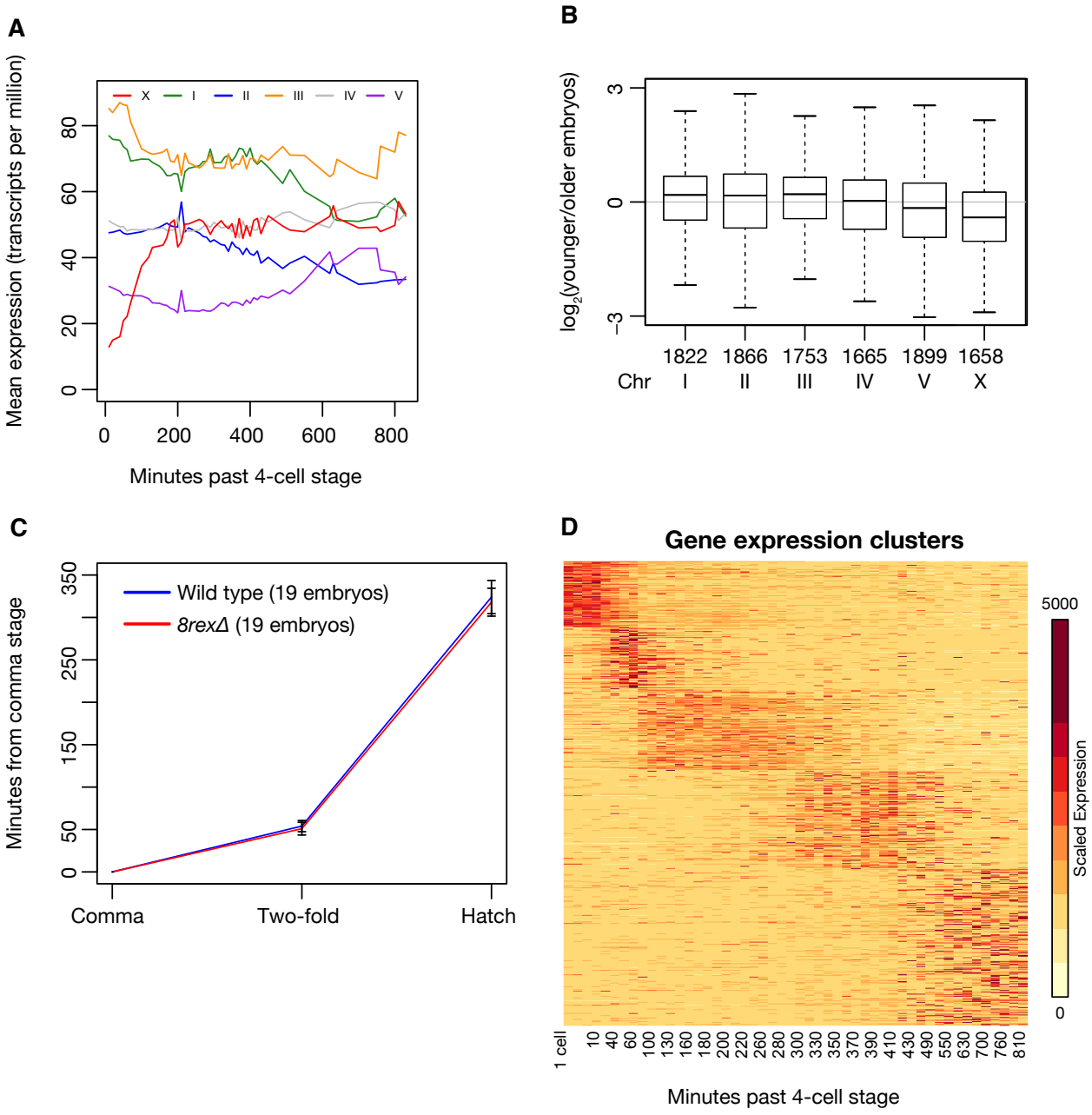
A
Mean expression (transcripts per million)
X
I
II
III
IV
V
0
20
40
60
80
0
200
400
600
800
Minutes past 4-cell stage
B
log2(younger/older embryos)
3
0
−3
1822
1866
1753
1665
1899
1658
Chr
I
II
III
IV
V
X
C
Minutes from comma stage
Wild type (19 embryos)
8rexΔ (19 embryos)
0
50
150
250
350
Comma
Two-fold
Hatch
D
Gene expression clusters
5000
Scaled Expression
0
1 cell
10
40
60
100
130
160
180
200
220
260
280
300
330
350
370
390
410
430
490
550
630
700
760
810
Minutes past 4-cell stage

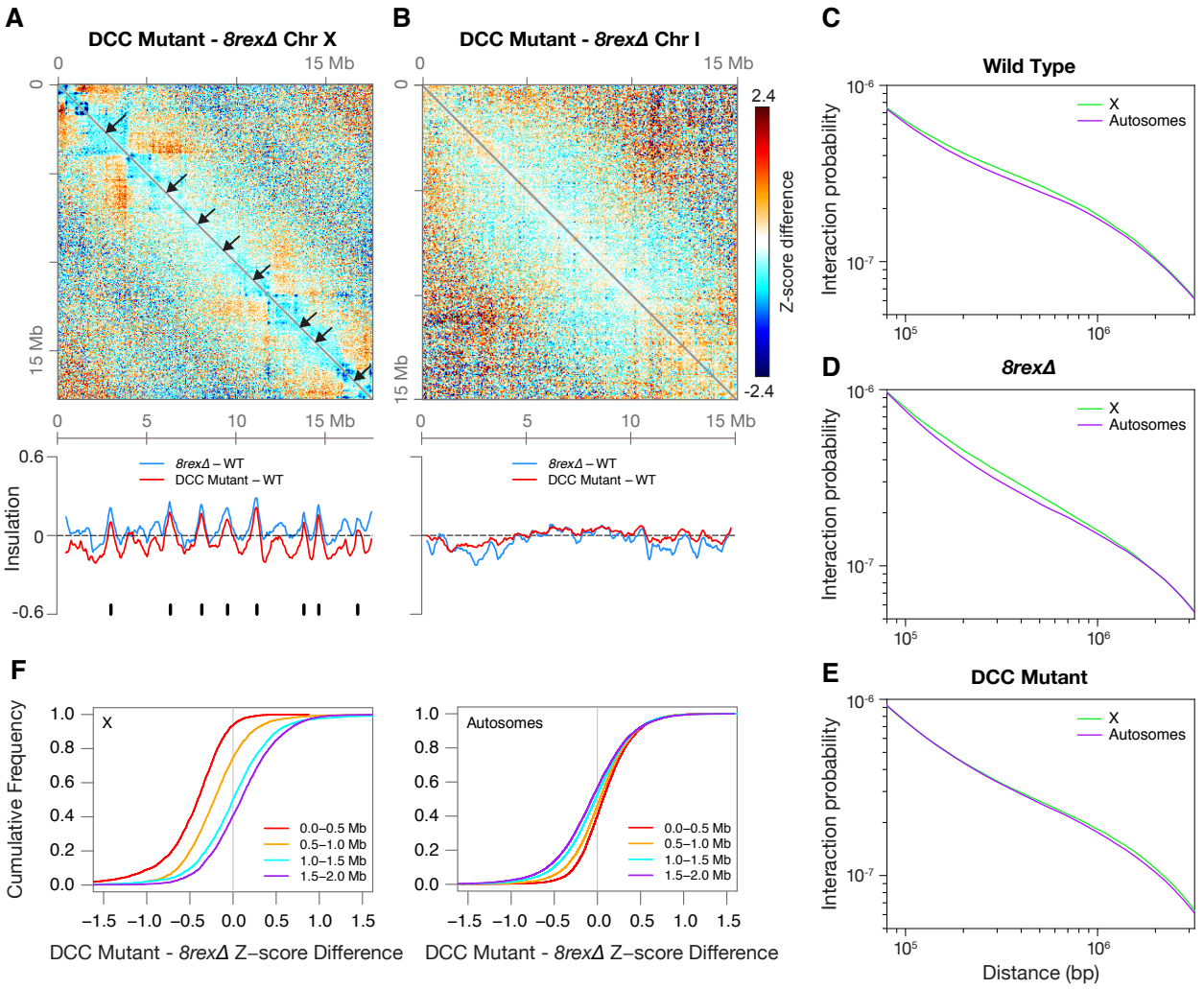
A
DCC Mutant - 8rexΔ Chr X
B
DCC Mutant - 8rexΔ Chr I
Z-score difference
Insulation
8rexΔ – WT
DCC Mutant – WT
C
Wild Type
D
8rexΔ
E
DCC Mutant
Interaction probability
X
Autosomes
Distance (bp)
F
Cumulative Frequency
0.0–0.5 Mb
0.5–1.0 Mb
1.0–1.5 Mb
1.5–2.0 Mb
DCC Mutant - 8rexΔ Z–score Difference

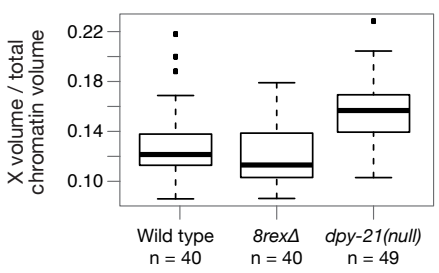
G
X volume / total chromatin volume
Wild type n = 40
8rexΔ n = 40
dpy-21(null) n = 49

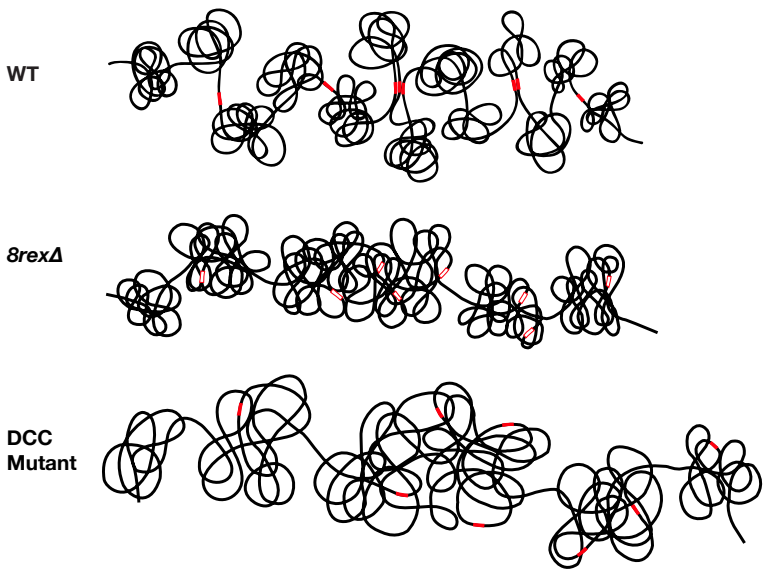
H
WT
8rexΔ
DCC Mutant

Figure 5, Supplement 1

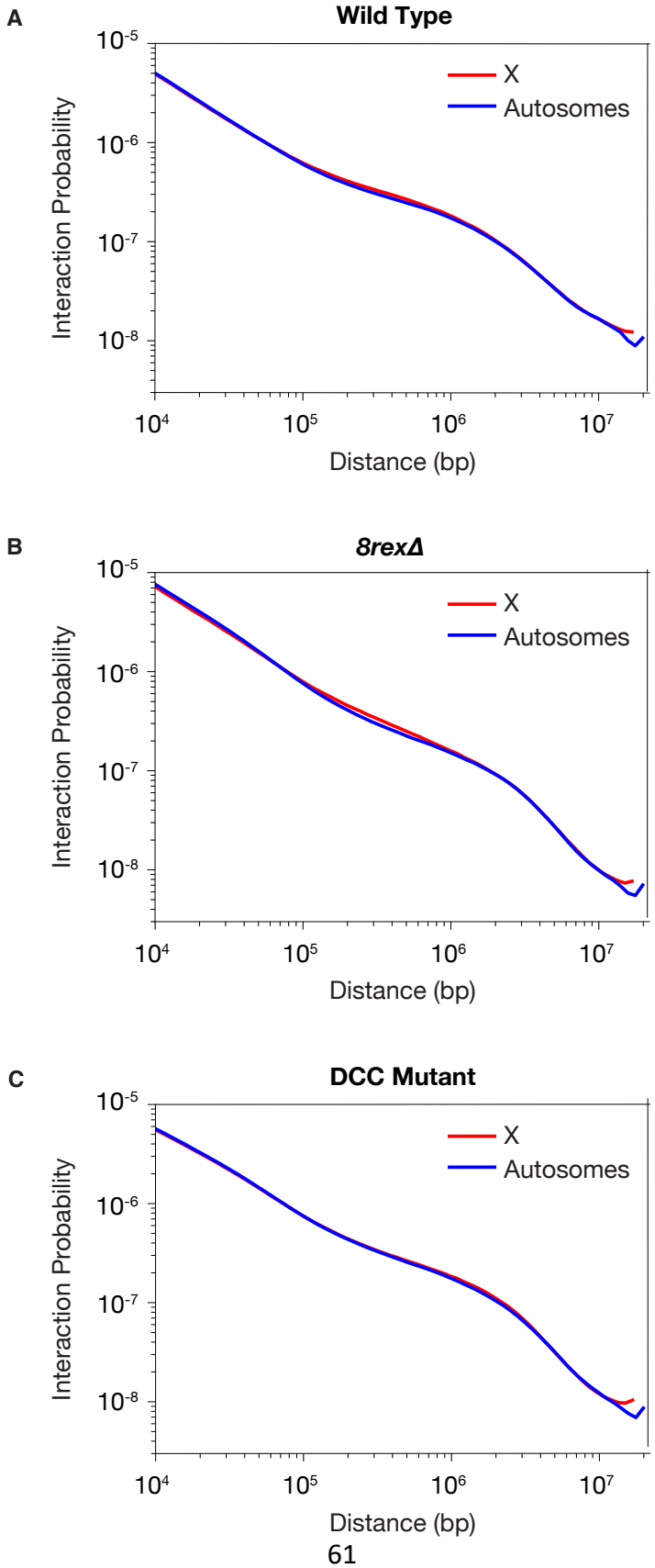

Figure 6

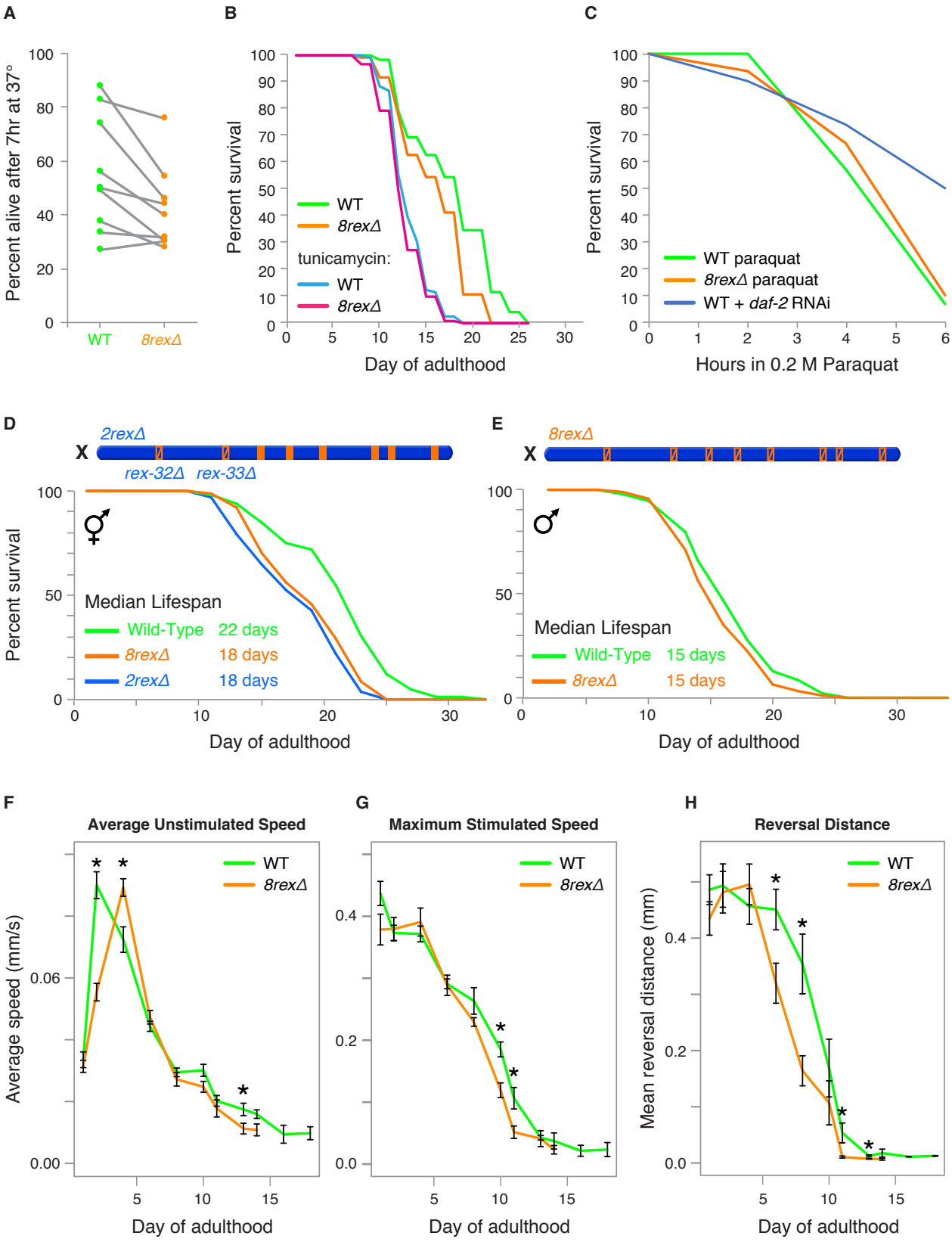
A
Percent alive after 7hr at 37°
WT
8rexΔ
B
Percent survival
WT
8rexΔ
tunicamycin:
WT
8rexΔ
Day of adulthood
C
Percent survival
WT paraquat
8rexΔ paraquat
WT + daf-2 RNAi
Hours in 0.2 M Paraquat
D
2rexΔ
X
rex-32Δ rex-33Δ
Percent survival
Median Lifespan
Wild-Type 22 days
8rexΔ 18 days
2rexΔ 18 days
Day of adulthood
E
8rexΔ
X
Median Lifespan
Wild-Type 15 days
8rexΔ 15 days
Day of adulthood
F
Average Unstimulated Speed
Average speed (mm/s)
WT
8rexΔ
Day of adulthood
G
Maximum Stimulated Speed
WT
8rexΔ
Day of adulthood
H
Reversal Distance
Mean reversal distance (mm)
WT
8rexΔ
Day of adulthood

Figure 6, Supplement 1

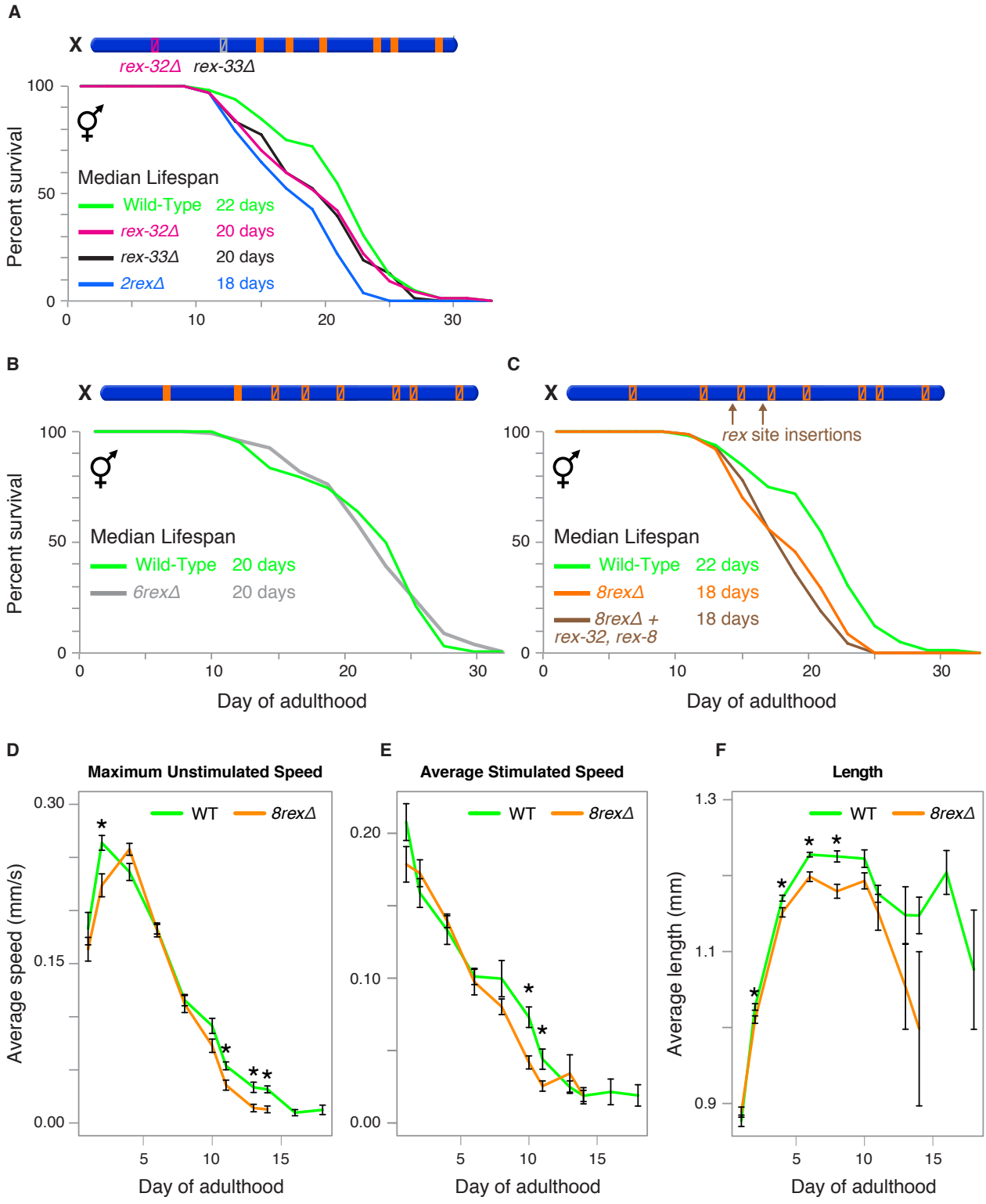

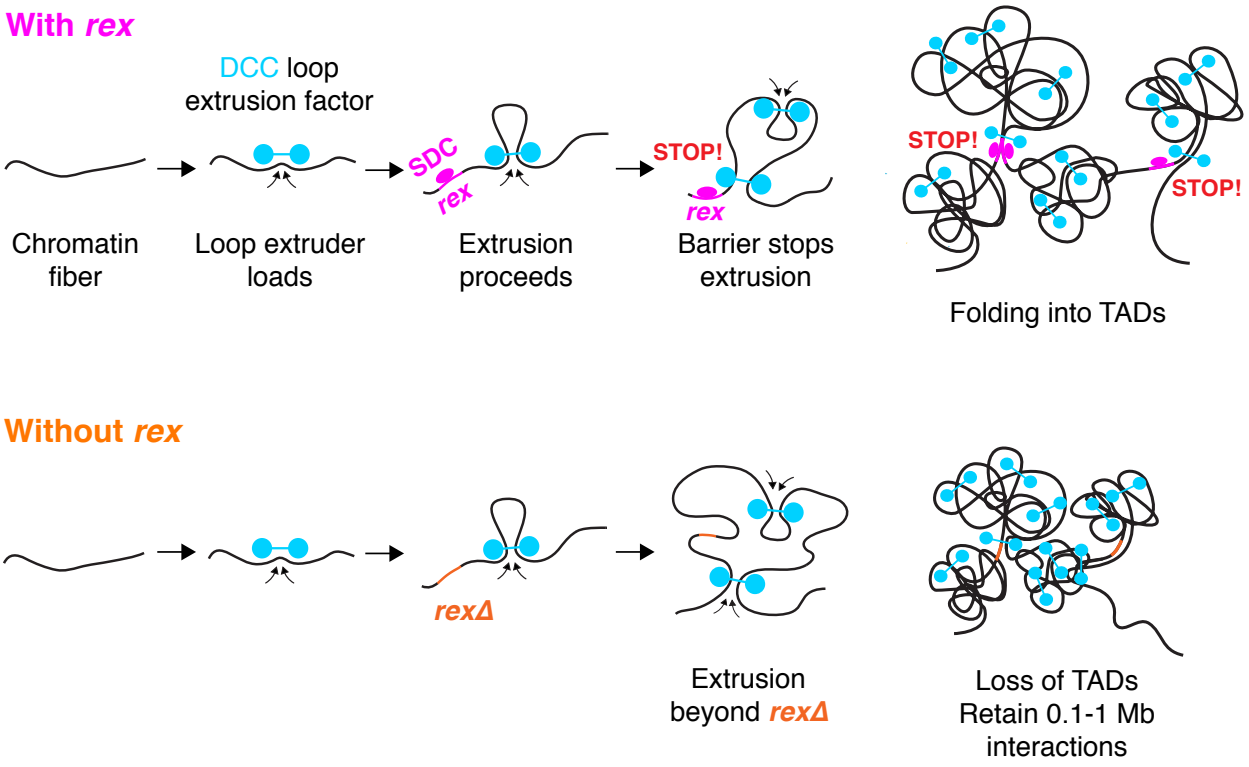
With rex
DCC loop extrusion factor
SDC
rex
STOP!
rex
STOP!
STOP!
Chromatin fiber
Loop extruder loads
Extrusion proceeds
Barrier stops extrusion
Folding into TADs
Without rex
rexΔ
Extrusion beyond rexΔ
Loss of TADs
Retain 0.1-1 Mb interactions

Appendix: Protocols

In addition to the experimental details provided in the Methods section of Chapter 2, here are step-by-step versions of the following protocols:

Growing 6L of HB101 Bacteria
Isolating Cas9 mutants
C. elegans in situ Hi-C protocol (with biotinylated nucleotides)
ChIP-seq Protocol
RNA-seq Protocol
Measuring *C. elegans* Thermotolerance Protocol
Filming timing of embryogenesis in two genotypes

Growing 6L of HB101 Bacteria

Materials:

- 6L TB media
- 600ml 1M KPO_4 pH 7
- Resuspension buffer: 10mM KPO_4 pH 7 10% glycerol (filter sterilized)
- Fresh HB101 growing on an LB plate

Day 1

1. Make sure you have enough autoclaved media and phosphate buffer.
2. Inoculate an overnight culture of HB101 in LB (you need ~6ml).
3. Sign up for the shaker and centrifuge.

Day 2

4. In each of 6 large baffled flasks, combine 900ml TB media, 100ml 1M phosphate buffer, and 1ml of HB101 culture. For RNAi bacteria, also add 100ug/ml ampicillin.
5. Shake the flasks at 37° at 200rpm for ~24hr in the shaker in room 135. Set the temperature on the shaker by holding down the * button while pushing the button with the up or down arrow.

Day 3

6. Rinse out the four centrifuge bottles with 70% ethanol and allow them to dry. Record the mass of an empty bottle for reference.
7. Spin down the 6L of bacteria at ~6000g for 15 minutes in the large centrifuge in room 135 (you will have to spin twice to fit everything). Use the scale to the left of the centrifuge to balance the bottles. Discard the supernatant.
8. Weigh the pellets and add a volume of resuspension buffer equal to the mass of the pellet (e.g. for a 25g pellet, add 25ml buffer).
9. Dislodge the pellet with a spatula and resuspend by vortexing thoroughly.
10. Aliquot the bacteria into 50ml conical tubes and freeze in liquid nitrogen. Store at -80.

Isolating Cas9 mutants

Compiled by Erika Anderson, April 2018

There are possible variations for every step, but this is what I generally do.

1. Place each injected worm on an individual plate and grow at 25° for three days.
2. Dilute HB101 bacteria in S media to OD 0.4.
3. Fill each well of two 96-well tissue culture plates with 50ul of the diluted HB101 food.
4. Pick one dpy or rol worm into each well. At this point, most of the dpy and rol F1s should be L4s or young adults.
5. Place the plates in a closed container with a damp paper towel at the bottom to prevent drying out. Grow the F1s at 25° until nearly all the wells have more than ten visible F2s (about 3 days).
6. Prepare two 96-well PCR plates by dispensing 10ul of lysis buffer (0.1mg/ml Proteinase K in 1x PCR buffer) into each well.
7. Using a multichannel pipette, transfer 10ul of worms in S media to the lysis buffer.
8. Freeze the lysis plates in liquid nitrogen.
9. In a thermocycler, heat the plates to 65° for 1 hour followed by 95° for 15 minutes (to inactivate the Proteinase K). For long-term storage, keep the lysate at -80° (but 4° is fine for a couple days).
10. PCR using your screening oligos. Taq is cheaper, but Phusion works much more robustly, especially for longer PCR products. I do a 20ul PCR using 1ul of the lysate. (Design your primers to give two different sized bands in wild type and mutant and put them outside the homology arms so there's no risk of amplifying your template if it forms an extrachromosomal array.)
11. Run the PCRs on a large 1% gel. It takes about 150ml of agarose, and you can load both 96-well plates on one gel if you use four combs.
12. If the Cas9 cut, you should see some smaller and larger bands of various sizes indicating large deletions or insertions by end joining. Identify the wells that have a band of the proper size for your desired insertion/deletion (To be sure of the size, I like to repeat the PCR for the promising candidates and run them side-by-side on a second gel.)
13. For the wells that are candidates for having the correct mutation, pipette the F2s from the well onto a regular NGM plate and transfer about 12 F2s to individual plates.
14. After the F2s have laid progeny, screen for homozygotes by transferring the F2 (or several F3s) to 10ul of lysis buffer and lysing and PCRing as before. Identify the F2s that have only the band corresponding to your insertion/deletion size and no wild-type band. (Sometimes I also use a second set of primers that will only give a product in the wild type.)
15. Submit 10ul of the PCR along with the sequencing primer at 10uM and the form here http://mcb.berkeley.edu/barker/dnaseq/order (Single Tube PCR Cleanup Order Form) to the sequencing facility for cleanup and sequencing. Get our PO from the lab FileMaker database.
16. If the sequence is correct, outcross the worms your desired number of times. Also sequence the *dpy-10* locus to make sure it's wild type.

C. elegans in situ Hi-C protocol (with biotinylated nucleotides)

Compiled by Erika Anderson, July 2016.

Crosslinking, isolating nuclei, and digestion

1. Bleach gravid hermaphrodites to obtain at least 0.5g of embryos. Freeze down in an equal volume of 1x M9 in 1ml aliquots and store at −80 °C
2. Thaw embryos on ice and supplement with 1 mM PMSF and 5 mM DTT.
3. Wash once in 30 ml formaldehyde solution (1× M9 solution with 2% (v/v) formaldehyde, Polysciences 18814-20) by spinning for 1 min at 2000rpm.
4. Crosslink in 50 ml of formaldehyde solution for 30 min at room temperature while shaking.
5. Wash once with 50 ml of 100 mM Tris-HCl, pH 7.5 to quench the reaction.
6. Wash twice with 50 ml of 1× M9.
7. Transfer to a 1.5ml tube and wash once in 1ml of lysis buffer (10 mM Tris-HCl, pH 8.0, 10 mM NaCl and 0.2% (v/v) Igepal CA-630 (Sigma I8896)) supplemented with 5 mM DTT, 1 mM PMSF, 0.1% (v/v) protease inhibitors (EMD 539134) and 0.5 mM EGTA. Spin at 2000g for 1min.
8. To obtain extract, dounce embryos 10 times using the large pestle A (Kontes 2 ml glass dounce, Spectrum 985-44182; clearance 0.076–0.127 mm), and then 10 times using the small pestle B (clearance 0.01–0.069 mm) on ice.
9. Spin extract for 5 min at 100*g* at 4 °C, and save the supernatant.
10. Resuspend the pellet in 750µl of supplemented lysis buffer and dounce again. Repeat steps 8-10 until the supernatant becomes clear (5-7 times).
11. Spin again at 100g for 5min, and remove supernatant to avoid broken carcasses.
12. Combine all supernatants. Mix 9ul of nuclei with 1ul of 10ug/ml DAPI and count the nuclei using a haemocytometer on the SP2. I dilute the nuclei 1:100 and count the nuclei in the center square. Nuclei/ml = (nuclei in the center square) x (dilution factor) x 10^4. Typical yield is ~$3x10^8$ nuclei from 0.5g of embryos.
13. Spin down 1.5 x 10^8 nuclei for 5 min at 2,000*g* at 4°C in a low retention tube. Unused nuclei can be resuspended in Nuclei storage buffer (50mM Tris-Cl pH 8.0, 25% glycerol, 5mM MgAc2, 0.1mM EDTA, 5mM DTT), frozen in liquid nitrogen, and stored at -80°.
14. Remove the supernatant, wash once with 500ul lysis buffer, and repeat the spin.
15. Gently resuspend pellet in 50ul of 0.5% SDS and incubate at 62°C for 5-10 min.
16. Add 145µl of water and 25µl of 10% Triton X-100 (Sigma, 93443) to quench the SDS. Mix well, avoiding excessive foaming. Incubate at 37°C for 15 minutes.
17. Add 25µl of 10X DpnII Buffer and 2ul (100U) of DpnII restriction enzyme and digest chromatin overnight at 37°C with rotation. A significant amount of digestion takes place within 2hr.

Biotin incorporation, ligation, and crosslink reversal

18. Incubate at 62°C for 20 minutes to inactivate restriction enzyme, then cool to room temperature.

19. To fill in the restriction fragment overhangs and mark the DNA ends with biotin, add 50µl of fill-in master mix:
    37.5µl of 0.4mM biotin-14-dATP (Life Technologies, 19524-016)
    1.5µl of 10mM dCTP
    1.5µl of 10mM dGTP
    1.5µl of 10mM dTTP
    8µl of 5U/µl DNA Polymerase I, Large (Klenow) Fragment exo minus
20. Mix by pipetting and incubate at 37°C for 45 minutes-1.5 hours with rotation.
21. Add 900µl of ligation master mix:
    535µl of water
    240µl of 5X T4 DNA ligase buffer (Invitrogen)
    100µl of 10% Triton X-100
    12µl of 10mg/ml Bovine Serum Albumin (100X BSA)
    13µl of 1 U/ µl T4 DNA Ligase (Invitrogen)
22. Mix by inverting and incubate at room temperature for 4 hours with slow rotation.
23. Degrade protein by adding 50µl of 20mg/ml proteinase K (NEB, P8102) and 120µl of 10% SDS and incubate at 55°C for 30 minutes.
24. Add 130µl of 5M sodium chloride and incubate at 68°C overnight or for at least 1.5 hours.

<u>DNA Purification, Shearing, and Size Selection</u>

25. Cool tubes at room temperature. Split into two 750µl aliquots in 2ml tubes and add 1.6X volumes of pure ethanol and 0.1X volumes of 3M sodium acetate, pH 5.2, to each tube. Mix by inverting and incubate on ice for 15 minutes.
26. Centrifuge at max speed at 4°C for 15 minutes. Keep the tubes on ice after spinning and carefully remove the supernatant by pipetting.
27. Resuspend, combining the two aliquots, in 800µl of 70% ethanol. Centrifuge at max speed for 5 minutes.
28. Remove all supernatant and wash the pellet once more with 800µl of 70% ethanol.
29. After removing all the ethanol, resuspend the pellet in 130µl of 1X Tris buffer (10 mM Tris-HCl, pH 8) and incubate at 37°C for 15 minutes to fully dissolve the DNA.
30. Transfer to a 130ul Covaris tube and shear on the S2 Covaris using this program:
    duty cycle, 10%
    intensity, 4
    cycles/burst, 200
    time, 55 s
31. Transfer sheared DNA to a fresh 1.5ml tube. Wash the Covaris vial with 70µl of water and add to the sample, bringing the total reaction volume to 200µl. Save 3ul to run on a gel to check shearing.
32. Warm a bottle of AMPure XP beads (Beckman Coulter, A63881) to room temperature. Add exactly 110µl (0.55X volumes) of beads to the reaction. Mix thoroughly by pipetting at least 8 times and incubate at room temperature for 5 minutes.
33. Separate on a magnet for 5min. Transfer the clear supernatant (which contains fragments under 500bp) to a fresh tube, avoiding any beads.

34. Add exactly 40µl of fresh AMPure XP beads to the solution. Mix by pipetting and incubate at room temperature for 5 minutes.
35. Separate on a magnet and keep the beads. Fragments in the range of 300-500bp will be retained on the beads. Discard the supernatant containing degraded RNA and short DNA fragments.
36. Keeping the beads on the magnet, wash twice with 700µl of freshly made 70% ethanol without mixing.
37. Spin for 10 seconds at 1000rpm, replace on the magnet, and remove the remaining ethanol. Leave the beads on the magnet for 3 minutes to allow residual ethanol to evaporate.
38. To elute DNA, add 300µl of 1X Tris buffer, gently mix by pipetting, incubate at room temperature for 5 minutes, separate on a magnet, and transfer the solution to a fresh 1.5ml tube.
39. Quantify DNA by Qubit dsDNA High Sensitivity Assay (Life Technologies, Q32854) and run 4ul on an agarose gel to verify successful size selection.
40. Quantify DNA by Qubit.

Biotin Pull-Down and Library Preparation

41. Resuspend Dynabeads MyOne Streptavidin T1 beads by vortexting (Life technologies, 65602) Wash 150µl of beads with 400µl of 1X Tween Washing Buffer (1X TWB: 5mM Tris-HCl (pH 7.5); 0.5mM EDTA; 1M NaCl; 0.05% Tween 20). Separate on a magnet for 1 min and discard the solution. Wash the beads twice more in 150ul of 1X Tween Washing Buffer.
42. Resuspend the beads in 300µl of 2X Binding Buffer (2X BB: 10mM Tris-HCl (pH 7.5); 1mM EDTA; 2M NaCl) and add to the reaction. Incubate at room temperature for 15 minutes with rotation to bind biotinylated DNA to the streptavidin beads.
43. Separate on a magnet for 2-3 min and remove the solution. To calculate how much DNA was pulled down by the beads, measure the concentration in the solution by Qubit.
44. Wash the beads by adding 600µl of 1X TWB and transferring the mixture to a new tube. Heat the tubes on a Thermomixer at 55°C for 2 min with mixing. Reclaim the beads using a magnet. Discard supernatant.
45. Repeat wash.
46. Resuspend beads in 100ul 1X End-Repair buffer and transfer to a new tube. Instead of End-Repair buffer, you can instead use PNK buffer:
    100mM MgCl2
    700mM Tris-HCl pH 7.5
    50mM DTT
    (You can stop here or before any of the library preparation steps and store the beads in the respective buffer at 4° overnight.) Reclaim beads and discard the buffer.
47. Resuspend beads in 100ul End Repair mix:
    10ul 10X End-Repair buffer
    10ul 2.4mM dNTP mix
    10ul 10mM ATP
    2ul End-Repair enzyme mix

68ul water

48. Incubate at room temperature for 45 minutes with gentle rotation.
49. Wash the beads by adding 600µl of 1X TWB and transferring the mixture to a new tube. Heat the tubes on a Thermomixer at 55°C for 2 min with mixing. Reclaim the beads using a magnet. Discard supernatant.
50. Repeat wash.
51. Resuspend beads in 100µl 1X NEBuffer 2 and transfer to a new tube. Reclaim beads and discard the buffer.
52. Resuspend beads in 100µl of dATP attachment master mix:
    10µl 1X NEBuffer 2
    50µl 1mM dATP
    5µl 5U/µl NEB Klenow exo minus (NEB, M0212)
    35ul water
53. Incubate at 37°C for 30 minutes with gentle rotation. Separate on a magnet and discard the solution.
54. Wash the beads by adding 600µl of 1X TWB and transferring the mixture to a new tube. Heat the tubes on a Thermomixer at 55°C for 2 min with mixing. Reclaim the beads using a magnet. Discard supernatant.
55. Repeat wash.
56. Resuspend beads in 100µl 1X Quick ligation reaction buffer (NEB, B6058) and transfer to a new tube.
57. Reclaim beads and discard the buffer.
58. Resuspend in 50ul of ligation master mix and record the sample-index combination:
    25ul 2x Quick ligase ligation buffer
    2ul adapter
    2ul quick ligase
    21ul water
59. Incubate at room temperature for 15 minutes with rotation. Separate on a magnet and discard the solution.
60. Wash the beads by adding 600µl of 1X TWB and transferring the mixture to a new tube. Heat the tubes on a Thermomixer at 55°C for 2 min with mixing. Reclaim the beads using a magnet. Remove supernatant.
61. Repeat wash.
62. Resuspend beads in 100µl 1X Tris buffer and transfer to a new tube. Reclaim beads and discard the buffer.
63. Resuspend in 50µl of 1X Tris buffer.

<u>Amplification and Purification</u>

64. Do a test PCR and run a gel to determine how many cycles of amplification are needed. I test 8, 6, and 4 cycles by running 1/8, 1/32, and 1/128 of the sample for 11 cycles.
    Hi-C library, amplified directly off the beads
    10ul 5X Phusion HF Buffer
    0.4ul 10mM dNTPs
    2ul NEXTflex Primer Mix (12.5uM)

0.5ul Phusion DNA Polymerase
Water to 50ul

Cycle:
98° for 30sec
[98° for 10sec, 65° for 30sec, 72° for 30sec] x cycle number
72° for 5min
Hold at 12°
Aim for a final library concentration around 6ng/ul, which should be faintly visible on the gel.

65. Amplify the library using the determined number of cycles (I have found 5-6 to be sufficient). To avoid any problems with beads inhibiting the PCR, I divide the beads between seven 50ul PCRs.
66. After amplification, bring the total library volume to 350ul.
67. Separate on a magnet. Transfer the solution to a fresh tube and discard the beads.
68. Warm a bottle of AMPure XP beads to room temperature. Gently shake to resuspend the magnetic beads. Add 245µl of beads to the PCR reaction (0.7X volumes). Mix by pipetting and incubate at room temperature for 5 minutes.
69. Separate on a magnet and remove the clear solution.
70. Keeping the beads on the magnet, wash once with freshly made 700µl of 70% ethanol without mixing.
71. Remove ethanol completely. To remove traces of short products, resuspend in 100µl of 1X Tris buffer and add another 70µl of AMPure XP beads. Mix by pipetting and incubate at room temperature for 5 minutes.
72. Separate on a magnet and remove the clear solution.
73. Keeping the beads on the magnet, wash twice with 700µl of freshly made 70% ethanol without mixing.
74. Leave the beads on the magnet for 5 minutes to allow the remaining ethanol to evaporate.
75. Add 25-50µl of 1X Tris buffer to elute DNA. Mix by pipetting, incubate at room temperature for 5 minutes, separate on a magnet, and transfer the solution to a fresh labeled tube. The result is a final in situ Hi-C library ready to be quantified and sequenced.
76. To check the library, clone using the Zero Blunt TOPO PCR Cloning Kit. Mix:
    1ul amplified library
    1ul salt solution
    3ul water
    1ul pCR-II-Blunt-TOPO vector
    Incubate at room temperature for 5 minutes. Transform 2ul into competent cells and plate on kanamycin plates.
77. Colony PCR using the following primers with annealing temperature 52° for Taq.
    EA235: CCA GTG AAT TGT AAT ACG ACT CAC TAT AGG G
    EA236: CGC CAA GCT ATT TAG GTG ACA CTA TAG

For more robust colony PCR, first pick individual colonies to 20ul of water using a pipette tip. Incubate at 95° for 15 min. Use 1ul of this bacteria lysis in the PCR.

78. Submit 10ul of the final library for bioanalyzer and 100bp paired end sequencing on the HiSeq4000.

Sources:
Crosslinking and nuclei isolation from (Crane et al., 2015)
Subsequent Hi-C steps from (Rao et al., 2014)
Library preparation from Meyer Lab ChIP-seq protocol

Crane, E., Bian, Q., McCord, R.P., Lajoie, B.R., Wheeler, B.S., Ralston, E.J., Uzawa, S., Dekker, J., and Meyer, B.J. (2015). Condensin-driven remodelling of X chromosome topology during dosage compensation. Nature.

Rao, S.S.P., Huntley, M.H., Durand, N.C., Stamenova, E.K., Bochkov, I.D., Robinson, J.T., Sanborn, A.L., Machol, I., Omer, A.D., Lander, E.S., et al. (2014). A 3D Map of the Human Genome at Kilobase Resolution Reveals Principles of Chromatin Looping. Cell *159*, 1665–1680.

ChIP-seq Protocol

compiled through combined efforts of many Meyer lab members

1. Bulking up for ChIP - Round 1

1. The night before, spread 8 MYOB or NGM plates with 1ml concentrated HB101 bacteria mixed with 1ml 1x M9 mix and leave at room temperature to dry.
2. Chunk one half of a recently starved small plate onto each large MYOB+HB101 plate.
3. Incubate at 20°C until most of the worms are gravid (~4 days).

2. Bleach Embryos for Bulk up

- Bleach solution
    - 36.5mL bleach (8.25%)
    - 12.5mL 10N NaOH
    - 201mL H_2O

4. Add ~5mL 1xM9 to each plate and shake on dancer ~15 minutes
5. Wash worms off plate over mesh in beaker
6. Pipette worms up and down with 25mL pipette to help wash off bacteria
7. Wash worms by pouring M9 from 500mL beaker over mesh
8. Transfer the gravid worms to a 250ml bottle (or a 50ml tube if you have <5ml of packed worms)
9. Spin for 1 min at 2000rpm and aspirate off excess M9.
10. Add at least 9 times the worm volume of bleach solution.
11. Shake and vortex bleach, periodically checking under scope for most of the worms to be broken but not completely disintegrated. It should take 3 - 5min.
12. Spin for 1min at 2000rpm, max brake
13. Remove bleach solution by pouring.
14. Wash twice in 250mL M9 - spin 1 min at 2000rpm, 7/9 brake
15. Transfer to 50mL conical and wash 1x in 50mL M9
16. Shake worms for ~24h at 20°C in 100mL sterile M9
17. Prepare MYOB or NGM plates with 2mL undiluted HB101

3. Plating starved L1s

18. Concentrate L1s by spinning for 1 min at 2000rpm
19. Resuspend in ~10mL 1xM9
20. Plate 100,000 L1s per HB101 plate

Repeat the bulking up steps until you have enough gravid hermaphrodites. 10-20 plates with 100,000 worms give plenty of material for a couple ChIPs.

Bleaching and Fixing Embryos for ChIP

1) Follow bleach protocol as before until step 12.
2) Filter embryos over a 40uM cell strainer into a 50ml tube to remove remaining pieces of adult carcasses.
    a. Pipette up and down to get as many embryos through the strainer as possible

b. After collecting the embryos that passed through in the filter, you can save the embryos that did not pass through the filter to hatch off in M9 for the 2nd ChIP replicate

3) Spin down, remove the supernatant, and freeze the pellet in liquid nitrogen. I use ~0.3-0.5g of embryos to get enough extract for three ChIPs.

Fixing, Douncing, and Covaris for ChIP

1) Thaw the pellet by washing with 50ml room temperature 1xM9 buffer
2) Wash the pellet in 30ml of fix solution (2% formaldehyde in 1x M9)
3) Fix in 50ml of fix solution for 10-30 min with gentle rocking.
4) Wash in 10mM Tris-HCl pH 7.5 to stop fixation
5) Wash the pellet once in FA and resuspend in FA buffer with protease inhibitors to a total volume of 1ml. Protease inhibitors: 5mM DTT (5uL of 1M DTT), 1mM PMSF (10 uL 100mM PMSF), 1:1000 PI (1uL)
6) Prepare the Covaris in advance by filling the basin with Millipore water, turning on the chiller, and degassing for 1 hour.
7) Pipet the embryos into a 2ml Dounce homogenizer. Grind with 50 slow strokes in the homogenizer.
8) Add sarkosyl to a final concentration of 0.1%
9) Transfer the embryos to a Covaris tube. (Use the same volume for all samples to ensure consistent shearing.)
10) Run the following program on an S2 Covaris:
    Step 1: Duty cycle: 20%, Intensity 8, Cycles/Burst: 200, Time: 60s
    Step 2: rest for 45s
    30 cycles, total time: 52:30
11) Centrifuge at max speed for 15 minutes at 4°C in refrigerated centrifuge
12) Keep supernatant, avoiding the white stuff on top (I spin down a couple times to try to avoid the white stuff as much as possible)
13) Determine the protein concentration using the BCA assay. Freeze the material and store at -80° if you are not proceeding immediately to ChIP
14) If you want to check the fragment size: mix 25ul of input material with 225uL ChIP elution buffer (10mM Tris-Cl pH 8.0, 1mM EDTA, 250mM NaCl, 1% SDS), and incubate for at least 3.5 hours at 65°C. Add 2uL of 10mg/mL ProteinaseK and 1uL of 20mg/mL RNaseA. Incubate at 55°C for 4 hours. Purify using Qiagen PCR cleanup. Run the DNA on a 1% agarose gel to check fragment size (should be about 200-600bp).

Immunoprecipitation

1. Thaw the frozen ChIP material on ice
2. To avoid any precipitate, centrifuge at max speed for 10 minutes at 4°C
3. Prepare each IP in a 1.5ml tube.
    Use 2mg total protein per IP (should be about 40ug of DNA)
    Add the amount of antibody you've determined gives a good signal-to-background ratio (We've used 6.6ug for anti-DPY-27 and anti-SDC-3 antibodies)
    Add FA buffer+ protease inhibitors to bring the total volume to at least 500ul. Make sure the sarkosyl concentration is below 0.05%

4) Mix at 4°C overnight
5) Freeze 50ul of material to use for input sample
6) Add 50ul magnetic ProteinA Dynabeads to each IP tube. Before using, wash the beads 3 times in FA buffer
7) Mix at 4°C for at least 2 hours.
   Note: After I did my ChIP experiments, Qiming found that this alternative gives improved signal-to-noise in ChIP-qPCR and works well for ChIP-seq: Mix antibody with ProteinA Dynabeads in a total volume of 1ml FA buffer. Rotate for 1 hour at room temperature. Remove liquid and combine the beads with your sample. Rotate for 1 hour at room temperature.
8) Wash the beads for 5 minutes at room temperature with the following buffers:
   a. twice with FA buffer
   b. once with FA+1M NaCl buffer
   c. once with FA+0.5M NaCl buffer
   d. once with TEL buffer
   e. twice with TE pH 8.0
9) Meanwhile, thaw the input sample and add elution buffer to bring the volume to 250ul.
10) For the ChIP samples, elute the beads twice with 125ul elution buffer at 65°C for 15 minutes and combine the elutions.
11) Add 2ul 10mg/ml RNaseA to the input and elutions and incubate at room temperature for 1-2 hours (optional)
12) Add 2ul 10mg/ml Proteinase K to the input and elutions and incubate at 65°C for at least 4 hours or overnight (to reverse the crosslinks).
13) Purify the DNA using Qiagen PCR clean up. Elute DNA in 34ul water.

Library Preparation and amplification

End repair using End-It DNA End Repair Kit from Epicentre, ER0720

1. Combine:
   34ul ChIP DNA (or 10ng of input DNA)
   5uL 10X End-Repair buffer
   5uL 2.5mM dNTP mix
   5uL 10mM ATP
   Water to bring reaction to 49uL
   1uL End-Repair enzyme mix

2. Incubate at room temperature for 45 minutes.
3. Purify using QIAquick PCR Purification Kit eluting in 34uL of EB.

Addition of A to 3' Ends

4. Combine:
   34uL DNA from previous step
   5uL NEB Buffer 2
   10uL 1mM dATP
   1uL Klenow fragment (3->5 exo-)
5. Incubate for 30 minutes at 37°.

6. Purify using QIAquick MinElute PCR Purification Kit. Elute in 12uL EB.

Note: We avoid repeated thawing and refreezing of dATP.

Adapter Ligation

7. Combine:
   12uL DNA from previous step
   15uL 2x DNA ligase buffer
   1uL NEXTflex barcode diluted 1:200
   2uL DNA ligase
8. Incubate reaction for 15 minutes at room temperature.
9. Purify using QIAquick PCR Purification Kit. Elute in 30ul.

Amplification

10. Determine the number of cycles of amplification needed. I test 17, 15, and 13 cycles, by running PCRs for 21 cycles with 1/16, 1/64, and 1/256 of the material.
11. Combine:
    1.875ul DNA
    10ul 5X Phusion HF Buffer
    2ul NEXTflex Primer mix (12.5uM)
    0.4 ul 10mM dNTPs
    0.5 ul Phusion DNA Polymerase
    Water to 50ul

    Note: The primers can be ordered directly from IDT rather than buying the mix.
    P5: 5' AAT GAT ACG GCG ACC ACC GA 3'
    P7: 5' CAA GCA GAA GAC GGC ATA CGA GAT 3'
12. Amplify with this program:
    30s at 98°
    [10s at 98°, 30s at 65°, 30s at 72°] x21 cycles
    5min at 72°
    Hold at 12°
13. Run the PCRs on a gel and choose the number of cycles based on being able to see a faint smear of the correct size.
14. Amplify the full library using the same program but with the determined number of cycles:
    remaining DNA
    10ul 5X Phusion HF Buffer
    2ul NEXTflex Primer mix (12.5uM)
    0.4 ul 10mM dNTPs
    0.5 ul Phusion DNA Polymerase
    Water to 50ul
15. Purify using the MinElute PCR Purification Kit and elute in 10-20ul.
16. Size select using Pippin prep to remove adaptor dimers.
17. Sequence with 50bp single-end reads.

FA buffer
50mM HEPES/KOH pH 7.5, 1mM EDTA, 150mM NaCl, 0.1% sodium deoxycholate, 1% TritonX-100

FA+1M NaCl buffer
50mM HEPES/KOH pH 7.5, 1mM EDTA, 1M NaCl, 0.1% sodium deoxycholate, 1% TritonX-100

FA+0.5M NaCl buffer
50mM HEPES/KOH pH 7.5, 1mM EDTA, 500mM NaCl, 0.1% sodium deoxycholate, 1% TritonX-100

TEL buffer
10mM Trs-Cl pH8.0, 1mM EDTA, 250mM LiCl, 1% sodium deoxycholate, 1% NP-40

TE
10mM Tris-Cl pH 8.0, 1mM EDTA

Elution buffer
10mM Tris-Cl pH 8.0, 1mM EDTA, 250mM NaCl, 1% SDS

RNA-seq Protocol

Compiled by Bayly Wheeler

RNA isolation protocol is a derivation of Life Tech's TRIzol protocol, originally developed by Chomczynski and Sacchi (Analytical Biochemistry, 1987)

RNA-seq protocol is adapted from three different protocols

- S. Lott for RNA seq from small amounts of total RNA for reagents from illumina
- Te-Wen Lo for standard RNA seq
- Will Kruesi for library preparation following standard Meyer lab protocol

RNA Isolation

1. Collect embryos in ~50 µl or less of aqueous buffer (up to about 150 µl ok)
2. Either freeze the sample or go to the next step IMMEDIATELY.
3. Thaw samples by vortexing at RT
4. Add 5 µL of a 20mg/mL glycogen solution
5. To fresh or frozen samples, add 1000µl TRIzol reagent (Life Technologies) and mix thoroughly/homogenize by pipetting up and down several times.
6. Vortex 10 sec on high.
7. Add 200 µl chloroform.
8. Vortex 30 sec on high.
9. Spin at full speed (~14K) for 5 min.
10. Transfer the aqueous phase to a clean (RNAse-free) 1.5 ml tube.
11. Add 0.7-0.8 volumes of isopropanol (usually 560 µl)
12. Mix well by shaking and vortexing.
13. Precipitate overnight at -20°C.
14. Spin at full speed (~14K g) for 15 min (I prefer 4ºC)
15. Carefully remove the supernatant by pipet.
16. Wash once with 500 µl 75% ethanol.
17. The pellet should be visible (opaque) after the addition of ethanol.
18. Spin at full speed for 5-10 min.
19. Carefully remove the supernatant by pipet.
20. Pulse spin (up to full speed) the tube to collect all residual ethanol at the bottom.
21. Remove remaining supernatant by pipet.
22. Allow the pellet to air dry for 1-2 min.
23. Dissolve the pellet in 250 µl RNAse-free water (unless you are worried that you started out with too few embryos, then resuspend in something closer to 50 µl)

1. **mRNA purification from Total RNA** you will need two heat blocks, one at 80°C and one at 65°C. Vortex beads vigorously in each step to resuspend and wash. Do not allow beads to dry. The Illumina mRNA-Seq sample prep guide has more guidance as to how to work with the beads.

1.1. Dilute 10ug of each RNA prep with nuclease-free H_2O to 50µL in a 1.5 mL RNase free non-sticky Eppendorf tube.
1.2. Heat the sample at 65°C for 5 minutes to disrupt the secondary structures and place the tube on ice.
1.3. Meanwhile, aliquot 100µL of Dynal oligo(dT) beads (Invitrogen, #610-06) into a 1.5mL RNase free non-sticky eppendorf tube.
1.4. Wash the beads twice with 100µL of Binding Buffer (20mM Tris-HCl pH 7.5, 1.0M LiCl and 2mM EDTA) and remove the supernatant.
1.5. Resuspend the beads in 50µL of Binding Buffer and add the 50µL of total RNA sample from step 2; rotate the tube at RT for 5 minutes and remove the supernatant.
1.6. Wash the beads twice with 100µL of Washing Buffer B (10mM Tris-HCl PH 7.5, 0.15M LiCl, 1mM EDTA).
1.7. Prepare for second round of oligo-dT purification by aliquoting 80µL of Binding Buffer to a fresh 1.5mL RNase free non-sticky Eppendorf tube.
1.8. Remove the supernatant from the beads of step 6, add 20µL of 10mM Tris-HCl and heat the beads at 80°C for 2 minutes to elute mRNA. Immediately put the beads on the magnet stand and transfer the supernatant (mRNA) to the tube from step 7. Add 100µL of Washing Buffer B to the remaining beads.
1.9. Heat the mRNA sample from step 8 at 65°C for 5 minutes to disrupt the secondary structures and place the tube on ice.
1.10. Meanwhile, wash the beads from step 8 twice with 100µL of Washing Buffer B, and remove the supernatant.
1.11. Add 100µL of mRNA sample from step 9 to the beads; rotate the tube at RT for 5 minutes.
1.12. Remove the supernatant and wash the beads twice with 100µL of Washing Buffer B.
1.13. Remove the supernatant from the beads, add 18µL of 10mM Tris-HCl, and heat the beads at 80^0C for 2 minutes to elute mRNA. Immediately put the beads on the magnet stand and transfer the supernatant (mRNA) to a fresh 200µL thin wall PCR tube, and there should be ~18µL of mRNA.

2. Fragment mRNA (SL)

2.1. Assemble the following reaction:

10x fragmentation buffer	2µL
mRNA	18µL (or mRNA plus water)

2.2. Incubate the tube in a PCR thermocycler at 70°C for 8 minutes. Put the tubes on ice and add 2µL of fragmentation stop solution.
2.3. Add 80 µL of 100% Ethanol to fragmented RNA sample. Then transfer RNA/Ethanol mix to a 1.5 mL tube containing 60 µL of SPRI beads. Elute the RNA in 12 µL of EB.

Perform SPRI purification by following "SPRI purification protocol" shown at the end of this protocol.

3. First strand cDNA synthesis (SL)

3.1 Assemble the following reaction:

- Random Primer (3ug/µL) 1 µL
- mRNA 11.1µL

3.2 Incubate the tube in a PCR thermocycler at 65°C for 5 minutes and put the tubes on ice.

3.3 Mix the following in order (make 10% extra reagent for multiple samples):

- 5× 1st strand buffer 4µL
- 100mM DTT 2µL
- dNTP mix (25mM) 0.4µL
- RNAseOUT (40U/µL) 0.5µL

3.4 Add 6.9µL mixture to the tube, mix well, and heat the sample at 25°C in a thermocycler for 2 min (with no heated lid).

3.5 Add 1µL Superscript III to the sample, and incubate the sample in a thermocycler with following program:

- Step 1 25°C 10min
- Step 2 50°C 50min
- Step 3 70°C 15min
- Step 4 4 °C Hold

4. Second strand cDNA synthesis (SL)

4.1. Put the tubes on ice.

4.2. Add 13µL of H_2O to the first strand cDNA synthesis mix.

4.3. Add the following reagents:

- 5 × second strand buffer 10µL
- dNTP mix (25mM) 1µL

4.4. Mix well, incubate on ice 5 minutes and add:

- RNaseH (2U/µL) 1µL
- DNA pol I (10U/µL) 5µL

4.5. Mix well and incubate at 16°C in a thermocycler for 2.5 hours.

4.6. Purify the DNA by adding 75 uL of SPRI beads to 50 µL of cDNA mix and elute in 33µL of EB solution. Perform SPRI purification by following "SPRI purification protocol" shown at the end of this protocol.

End of Day 1, store samples at -20°C. The rest of the protocol offers more opportunities to stop. Any time after SPRI purification, you can store at -20°C. Be sure to use non-stick tubes for long term storage.

5. End Repair (WK)

5.1. Assemble the following reagents

- cDNA 33 µL
- 10X End-Repair buffer 5 µL
- 2.5mM dNTP mix 5 µL
- 10mM ATP 5 µL
- Sterile water (50uL total volume) 1 µL
- End-Repair enzyme mix 1 µL

5.2. Incubate at room temperature for 45 minutes
5.3. Purify the DNA by adding 75 µL of SPRI beads to 50 µL of End-repair-mix and elute in 33µL of EB solution.

6. Adenylation of 3' ends (WK)

6.1. Assemble the following reagents

- DNA from step 1 34 µL
- Klenow Buffer (NEB Buffer 2) 5 µL
- 1mM dATP 10 µL
- Klenow fragment (3→5 exo-) 1 µL

6.2. Incubate for 30 minutes at 37°C in a thermocycler
6.3. Purify the DNA by adding 75 uL of SPRI beads to 50 µL of adenylation reaction and elute in 12µL of EB solution. Perform SPRI purification by following "SPRI purification protocol" shown at the end of this protocol.

7. Adapter ligation (WK modified specifically for use with Bioos adaptors and invitrogen ligase)

Notes about adapters: The preannealed adapters from Bioos are sensitive to temperature and salt concentration. Warming above room temperature or diluting

adapters such that the salt concentration is less than 10^{-5} M will denature the adapters and cause the reaction to fail.

7.1. Assemble the following reagents

- DNA from Step 2 12 µL
- 2x DNA Quick Ligase buffer 14.3 µL
- Adapters (1/5 dilution in EB) 1.3 µL
- DNA ligase 1 µL

7.2. Incubate reaction for 15 minutes at room temperature.

7.3. Purify the DNA by adding 28.6 ul of SPRI beads to 28.6 µL of adaptor-ligation-mix and elute in 30µL of EB solution.

8. PCR (SL)

8.1. I first do a test PCR with 10, 12, or 14 cycles to figure out the ideal amount of amplification and then amplify the rest of the material. Set up PCR master mix, make 10% extra reagent for multiple samples, and aliquot 20µL to each PCR tube:

- 5× HF Phusion Buffer 10µL
- Bioos primer mix 2µL
- 25mM dNTP mix 0.5µL
- Phusion polymerase 0.5µL
- H_2O 7µL

8.2. Add 30µL purified ligation mix to the PCR tube.

8.3. Run the following PCR cycle:

- 98°C 30 sec
- 98°C 10 sec ⟵
- 65°C 30 sec × determined number of cycles
- 72°C 30 sec
- 72°C 5 min
- 4°C ∞

8.4. Purify the DNA by adding 50 µL of SPRI beads to 50 µL of PCR product and elute in 15-35µL of EB solution (depending on how small of a sample you started with, and which loading proceedure you plan to use). Perform SPRI purification by following "SPRI purification protocol" shown at the end of this protocol.

How to perform SPRI (Ampure XP) purification:

1. Transfer *** µL of well mixed SPRI beads (Ampure XP) from stock bottle to each 1.5 mL sample tube.
2. Pipette up and down for at least 8 times for mixing thoroughly.
3. Incubate at room temperature for 15 min.
4. Place 1.5 mL tubes on magnet stand for ~5 min until the liquid appears clear.
5. Discard the supernatant.
6. Add 180 µL of freshly made 70% Ethanol to the 1.5 mL tube without disturbing the beads. Leave the tubes on the magnet for all wash steps.
7. Wait for 30 seconds and discard the supernatant (70% Ethanol) by using pipette to transfer.
8. Repeat step 6 and 7 for a total of two 70% Ethanol washes.
9. Spin down for 10 seconds at 1000 rpm to spin down any ethanol from side of tube.
10. Place each 1.5 mL tube on magnet stand for 30 seconds then remove all the remaining Ethanol. (There is a delicate balance here of wanting to remove all the ethanol and not wanting to dry the beads too much as this reduces elution efficiency.)
11. Add *** µL of EB to the dry pellet for eluting the DNA. Pipette mixing the pellet and then sit at room temp for 2 min and put on the magnet stand or plate.
12. Transfer clear supernatant to new tubes. Label with all the information and store in - 20 °C.

Measuring *C. elegans* Thermotolerance

Compiled by Erika Anderson, June 2018, based on protocol from Phil Frankino (Dillin Lab)

1. Bleach gravid adults (a couple small plates yield a sufficient number) and incubate the embryos at 20° overnight with shaking. I used a 15ml tube with 10ml of M9 and taped it horizontally on the shaker.
2. Plate L1s on empty vector L4440 bacteria on RNAi plates. I plate ~300 L1s on a large plate. Incubate at 20° for three days until the worms are Day 1 adults.
3. Pick 10 worms to each of five small RNAi plates seeded with empty vector bacteria. It's best to use new plates because they're less likely to crack. Add an empty plate to the top and bottom of the stack. Place in a 37° incubator. I make sure to position the plates far from the blower. If I'm doing more than two genotypes, I put one plate from each genotype in each stack and stagger the timing of the stacks to minimize the amount of time the worms are out of the incubator for counting.
4. After 5 hours, remove the plates and record how many animals are alive, dead, and censored from the assay (due to crawling on the side of the plate where they dry out). A worm is defined as dead if it does not react after being poked with the pick.
5. Record the number of alive, dead, and censored worms again at 7 hours and 9 hours.
6. Calculate the percentage of animals alive at each time point (excluding censored worms).

Notes: This assay can also be done at 34°. In that case, heat shock the worms overnight and start counting after about 9 or 10 hours. The time between starting the heat shock and 50% mortality was less variable at 37°. I found the results to be quite variable, so it's crucial to include the control genotype each time.

Filming timing of embryogenesis in two genotypes

Compiled by Erika Anderson, August 2017, with Cel-Tak protocol from Satoru Uzawa

I. Prepare coverslips with Cel-Tak

1. Remove any dust from 18x18 coverslips by blowing air and using a Kimwipe.
2. Dilute Cel-Tak 10-fold in water for a final volume of 3.5ul x the number of coverslips. Add 1.8ul of 1N NaOH per coverslip. Vortex immediately and put 3ul on each coverslip.
3. Allow the coverslips to dry at room temperature.
4. Spot 2ul of poly-L-lysine solution on top of the dried Cel-Tak. Let dry for at least 10 minutes.
5. Rinse the coverslips in ethanol and then water. Remove liquid by blotting with filter paper.

II. Stick Genotype 1 worms to the coverslip and photograph them.

1. Pick 15 Genotype 1 worms into a 10ul drop of M9 on a slide.
2. Use a mouth pipette to remove most of the liquid and then pipette 10ul of clean M9 on top of the worms. Repeat this a couple times to rinse off bacteria.
3. Cut open the worms and transfer 10 2-cell embryos to a fresh drop of M9 using a mouth pipette.
4. Transfer the embryos to a new drop of M9 two successive times to remove any debris.
5. Transfer the embryos to the Cel-Tak on the coverslip. Using an eyebrow/guinea pig hair press the embryos down and line them up in the center of the drop.
6. Let the embryos settle for a few minutes. Then rinse the coverslip with M9 to remove loose embryos. Mark one corner of the coverslip to remember the orientation.
7. Satoru constructed a stand by gluing (with nail polish) two sticks on the bottom of a plastic plate. Place the coverslip face down on this stand and take a picture of the positions of the embryos using the GFP-scope camera. (Hit Live and then Album to take the image.) Place a wet Kimwipe in the plate and put the lid on to make sure the embryos don't dry out.

III. Add Genotype 2 embryos and image development.

1. Prepare an agarose pad (25ul of 2% agarose)
2. Isolate 10 Genotype 2 embryos as before.
3. Transfer the embryos to the agarose pad. Place the coverslip on top and seal with rubber cement.
4. Take another photo of the embryos with the GFP scope.
5. On the SP8, use Mark and Find to image the embryos overnight. Imaging settings: wavelength 670, WLL on 50%, power 11.8; Fluo Turret: Scan-PH; 20x objective; 512x512; speed: 400; Zoom: 5; image size: 116.25*116.25um; pixel size: 227.49x227.49nm; Image every 3 minutes for 13 hours (plenty of time for all the worms to hatch). Z size: 30um, 5 steps

6. Take a screenshot of the panel showing the mark and find positions.
7. Record the temperature in the microscope room. (It was between 22 and 23°.)

IV. Analyze movies

1. Using the photos of the embryos and the screen shot of the mark and find positions, identify the genotype of each embryo.
2. Use Priism command line to covert the tiffs into an mrc. example (run from folder with tifs in it): tiff2mrc -template=Position002_t%3t_z%1z_ch00.tif -z=0:4 -t=0:260 -palette=grey ../Position002.mrc
3. I went through each movie and recorded the frame when the embryo started transitioning towards bean stage, arrived at comma stage, completed two-fold stage, and hatched.